

Computational homogenization for the multi-scale analysis of multi-phase materials

Citation for published version (APA):

Kouznetsova, V. (2002). *Computational homogenization for the multi-scale analysis of multi-phase materials*. [Phd Thesis 1 (Research TU/e / Graduation TU/e), Mechanical Engineering]. Technische Universiteit Eindhoven. <https://doi.org/10.6100/IR560009>

DOI:

[10.6100/IR560009](https://doi.org/10.6100/IR560009)

Document status and date:

Published: 01/01/2002

Document Version:

Publisher's PDF, also known as Version of Record (includes final page, issue and volume numbers)

Please check the document version of this publication:

- A submitted manuscript is the version of the article upon submission and before peer-review. There can be important differences between the submitted version and the official published version of record. People interested in the research are advised to contact the author for the final version of the publication, or visit the DOI to the publisher's website.
- The final author version and the galley proof are versions of the publication after peer review.
- The final published version features the final layout of the paper including the volume, issue and page numbers.

[Link to publication](#)

General rights

Copyright and moral rights for the publications made accessible in the public portal are retained by the authors and/or other copyright owners and it is a condition of accessing publications that users recognise and abide by the legal requirements associated with these rights.

- Users may download and print one copy of any publication from the public portal for the purpose of private study or research.
- You may not further distribute the material or use it for any profit-making activity or commercial gain
- You may freely distribute the URL identifying the publication in the public portal.

If the publication is distributed under the terms of Article 25fa of the Dutch Copyright Act, indicated by the "Taverne" license above, please follow below link for the End User Agreement:

www.tue.nl/taverne

Take down policy

If you believe that this document breaches copyright please contact us at:

openaccess@tue.nl

providing details and we will investigate your claim.

Computational homogenization for the multi-scale analysis of multi-phase materials

This research was carried out under project number ME97020 in the framework of the Strategic Research Programme of the Netherlands Institute for Metals Research (NIMR).



Netherlands Institute
for Metals Research

CIP-DATA LIBRARY TECHNISCHE UNIVERSITEIT EINDHOVEN

Kouznetsova, Varvara G.

Computational homogenization for the multi-scale analysis of multi-phase materials / by Varvara G. Kouznetsova. – Eindhoven : Technische Universiteit Eindhoven, 2002.

Proefschrift. – ISBN 90-386-2734-3

NUR 971

Subject headings: heterogeneous materials / multi-phase materials / composite materials / multi-scale modelling / homogenization methods / constitutive modelling / micromechanics

Printed by Universiteitsdrukkerij TU Eindhoven, Eindhoven, The Netherlands.

Computational homogenization for the multi-scale analysis of multi-phase materials

PROEFSCHRIFT

ter verkrijging van de graad van doctor
aan de Technische Universiteit Eindhoven,
op gezag van de Rector Magnificus, prof.dr. R.A. van Santen,
voor een commissie aangewezen door het College voor Promoties
in het openbaar te verdedigen op
maandag 9 december 2002 om 16.00 uur

door

Varvara Gennadyevna Kouznetsova

geboren te Perm, Rusland

Dit proefschrift is goedgekeurd door de promotoren:

prof.dr.ir. M.G.D. Geers

en

prof.dr.ir. F.P.T. Baaijens

Copromotor:

dr.ir. W.A.M. Brekelmans

Contents

Summary	vii
Notation	ix
1 Introduction	1
1.1 Metals, classical and modern multi-phase materials	1
1.2 Modelling strategies for multi-phase materials	3
1.3 Scope and outline	5
2 First-order computational homogenization	7
2.1 Introduction	7
2.2 Basic hypotheses	8
2.3 Definition of the problem on the microlevel	10
2.4 Coupling of the macroscopic and microscopic levels	13
2.4.1 Deformation	13
2.4.2 Stress	14
2.4.3 Internal work	15
2.4.4 Consistent tangent stiffness	16
2.5 Nested solution scheme	19
2.6 Computational example	19
2.7 Concept of a representative volume element	23
2.7.1 General concept	23
2.7.2 Regular versus random representation	24
2.8 Discussion	29
3 Second-order computational homogenization	31
3.1 Introduction	31
3.2 General framework	34
3.3 Micro-macro kinematics	35
3.4 Stress and higher-order stress	42
3.5 Finite element implementation	44
3.5.1 RVE boundary value problem	44
3.5.2 Calculation of the macroscopic stress and higher-order stress	46

3.5.3	Macroscopic constitutive tangents	47
3.6	Nested solution scheme	49
3.7	RVEs in the second-order computational homogenization	51
4	Second gradient continuum formulation for the macrolevel	53
4.1	Introduction	53
4.2	Second gradient continuum formulation	56
4.3	Finite element implementation	59
4.3.1	Weak formulation	60
4.3.2	Finite element discretization	64
4.3.3	Iterative procedure	65
4.3.4	Finite elements	68
4.4	Validation and choice of elements	69
4.4.1	Mindlin elastic constitutive model	69
4.4.2	Patch test	70
4.4.3	Boundary shear layer problem	72
4.4.4	Choice of elements	75
5	Comparative analyses	77
5.1	Microstructural analyses	77
5.1.1	Macroscopic bending and tension	78
5.1.2	Macroscopic model of a notched specimen under tension	79
5.1.3	Microstructural and size effects	81
5.2	Computational homogenization modelling of macroscopic localization	84
5.3	Computational homogenization modelling of boundary shear layers	93
6	Conclusions and recommendations	99
A	Constitutive models	105
A.1	Compressible Neo-Hookean model	105
A.2	Elasto-plastic model	105
A.3	Bodner-Partom model	106
	Bibliography	109
	Samenvatting	119
	Acknowledgements	121
	Curriculum Vitae	123

Summary

Most of the materials produced and utilized in industry are heterogeneous on one or another spatial scale. Typical examples include metal alloy systems, porous media, polycrystalline materials and composites. The different phases present in such materials constitute a material microstructure. The (possibly evolving) size, shape, physical properties and spatial distribution of the microstructural constituents largely determine the macroscopic, overall behaviour of these multi-phase materials.

To predict the macroscopic behaviour of heterogeneous materials various homogenization techniques are typically used. However, most of the existing homogenization methods are not suitable for large deformations and complex loading paths and cannot account for an evolving microstructure. To overcome these problems a computational homogenization approach has been developed, which is essentially based on the solution of two (nested) boundary value problems, one for the macroscopic and one for the microscopic scale. Techniques of this type (i) do not require any constitutive assumption with respect to the overall material behaviour; (ii) enable the incorporation of large deformations and rotations on both micro and macrolevel; (iii) are suitable for arbitrary material behaviour, including physically non-linear and time dependent behaviour; (iv) provide the possibility to introduce detailed microstructural information, including a physical and/or geometrical evolution of the microstructure, in the macroscopic analysis and (v) allow the use of any modelling technique at the microlevel.

Existing (first-order) computational homogenization schemes fit entirely into a standard local continuum mechanics framework. The macroscopic deformation (gradient) tensor is calculated for every material point of the macrostructure and is next used to formulate kinematic boundary conditions for the associated microstructural representative volume element. After the solution of the microstructural boundary value problem, the macroscopic stress tensor is obtained by averaging the resulting microstructural stress field over the volume of the microstructural cell. As a result, the (numerical) stress-strain relationship at every macroscopic point is readily available. The first-order computational homogenization technique proves to be a valuable tool in retrieving the macroscopic mechanical response of non-linear multi-phase materials.

However, there are a few severe restrictions limiting the applicability of the first-order computational homogenization scheme (as well as conventional homogenization methods). Firstly, although the technique can account for the volume fraction, distribution and morphology of the constituents, the results are insensitive to the absolute size

of the microstructure. As a consequence, effects related to variations of this size cannot be predicted. Secondly, the approach is not applicable in critical regions of intense deformation, where the characteristic wave length of the macroscopic deformation field is of the order of the size of the microstructure. Moreover, if softening occurs at a macroscopic material point, the solution obtained from a first-order computational homogenization leads to a mesh dependent macroscopic response due to ill-posedness of the macroscopic boundary value problem.

In order to deal with these limitations, a novel, second-order computational homogenization procedure is proposed. The second-order scheme is based on a proper incorporation of the gradient of the macroscopic deformation tensor into the kinematical micro-macro framework. The macroscopic stress tensor and a higher-order stress tensor are retrieved in a natural way based on an extended version of the Hill-Mandel energy balance. A full second gradient continuum theory appears at the macroscale, which requires solving a higher-order equilibrium problem by a dedicated finite element implementation.

The most important property of the second-order computational homogenization method is in fact that the relevant length scale of the microstructure is directly incorporated into the description on the macrolevel via the size of the representative cell. This size should reflect the scale at which the relevant microstructural deformation mechanisms occur. Including the size of the microstructure allows to describe certain phenomena that cannot be addressed by the first-order scheme, such as size effects and macroscopic localization. Several microstructural analyses show that the second-order computational homogenization framework captures changes of the macroscopic response due to variations of the microstructural size as well as variations of macroscopic gradients of the deformation. If the microstructural size becomes negligible with respect to the length scale of the macroscopic deformation field, the results obtained by the second-order modelling coincide with those from the first-order approach. This important observation demonstrates that the second-order computational homogenization scheme is a natural extension of the first-order framework. In problems which exhibit macroscopic localization, the microstructural length scale determines the width of the localization band, thus providing mesh independent results. Furthermore, the second-order framework allows the modelling of surface layer effects via the incorporation of higher-order boundary conditions. Higher-order continuum modelling becomes considerably easier with the use of the second-order computational homogenization scheme because the second-order response is directly obtained from a microstructural analysis, rather than by closed-form constitutive relations which are difficult to formulate and which contain a large number of parameters.

Computational homogenization provides a versatile strategy to establish micro-macro structure-property relations for materials for which the collective behaviour of their evolving, multi-phase structure cannot be predicted by any other method.

Notation

Vectors and tensors

Tensors and tensor products are used in a Cartesian coordinate system, with \vec{e}_i , $i = 1, 2, 3$ a set of unit base vectors. Summation convention is applied over repeated indices.

Quantities

a	scalar
$\vec{a} = a_i \vec{e}_i$	vector
$\mathbf{A} = A_{ij} \vec{e}_i \vec{e}_j$	second-order tensor
${}^3\mathbf{A} = A_{ijk} \vec{e}_i \vec{e}_j \vec{e}_k$	third-order tensor
${}^n\mathbf{A} = A_{ijk\dots n} \vec{e}_i \vec{e}_j \vec{e}_k \dots \vec{e}_n$	n^{th} -order tensor

Operators

$\vec{a}\vec{b} = a_i b_j \vec{e}_i \vec{e}_j$	dyadic product
$\mathbf{A} \cdot \mathbf{B} = A_{ij} B_{jk} \vec{e}_i \vec{e}_k$	inner product
$\mathbf{A} : \mathbf{B} = A_{ij} B_{ji}$	double inner product
${}^3\mathbf{A} : {}^3\mathbf{B} = A_{ijk} B_{kji}$	triple inner product
$\nabla \vec{a} = \nabla_i a_j \vec{e}_i \vec{e}_j$	gradient operator
$\nabla \cdot \vec{a} = \nabla_i a_i$	divergence operator
$\mathbf{A}^c, A_{ij}^c = A_{ji}$	conjugate
${}^3\mathbf{A}^{RC}, A_{ijk}^{RC} = A_{ikj}$	right conjugate
${}^3\mathbf{A}^{LC}, A_{ijk}^{LC} = A_{jik}$	left conjugate
\mathbf{A}^{-1}	inverse
$\det(\mathbf{A})$	determinant

Matrices and columns

Quantities

a	scalar
\underline{a}	column
\underline{A}	matrix

Operators

\underline{AB}	matrix product
\underline{A}^T	transpose
\underline{A}^{-1}	inverse

Chapter 1

Introduction

1.1 Metals, classical and modern multi-phase materials

Industrial and engineering materials, as well as natural materials, are heterogeneous at a certain scale. This heterogeneous nature has a significant impact on the observed macroscopic behaviour of multi-phase materials. Various phenomena occurring on the macroscopic level originate from the physics and mechanics of the underlying microstructure. The overall behaviour of micro-heterogeneous materials depends strongly on the size, shape, spatial distribution and properties of the microstructural constituents and their respective interfaces. The microstructural morphology and properties may also evolve under a macroscopic thermomechanical loading. Consequently, these microstructural influences are important for the production routes and the life performance of the material and products made thereof.

From a historical point of view, metals have been exploited to make optimal use of their multi-phase nature, even though much of the findings long remained empirical. Contributing to the fundamental understanding of the collective behaviour of the assembly of phases is one of the main objectives of this work. Among examples of multi-phase materials are metal alloys, with an additional second phase in the form of precipitates or voids. These second phases are essential for the properties of the alloy and may lead to significant enhancement in the material overall performance or serve as an onset of damage. Moreover, almost all industrially used metals have a polycrystalline structure with grains of different orientations and grain boundaries. Another widely used heterogeneous industrial material is a metal matrix composite. For example, in aluminum metal matrix composites, silica fibres, fine stainless steel wires or small ceramic particles may be distributed throughout the aluminum matrix. This can produce vastly improved properties such as an increased strength, enhanced toughness and weight reduction. Also metal foams, acquiring considerable attention in the past decade, belong to the category of multi-phase materials. The enhanced properties (e.g. the low weight, high energy absorption etc.) of these materials are primarily due to their foamed microstructure. In some cases a heterogeneous structure is specifically

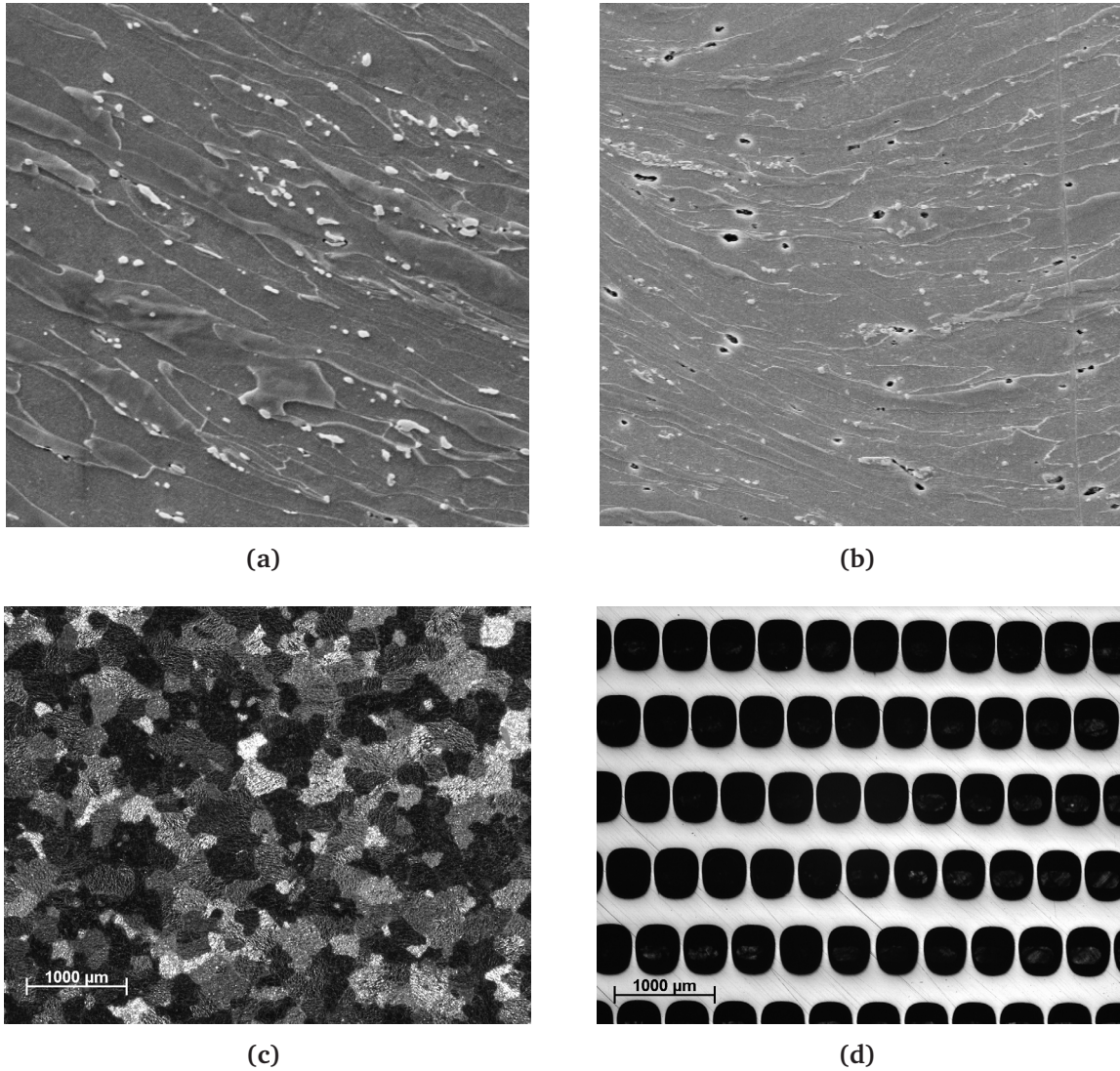


Figure 1.1: Examples of metallic heterogeneous microstructures: (a) SEM image of steel T67CA; the white spots are cementite particles; (b) SEM image of steel T61CA; voids are located around cementite particles; (c) light microscope image of an aluminum polycrystalline microstructure; (d) light microscope image of a shadow mask.

created for a particular product or application. An example of such a small scale heterogeneous structure is a shadow mask (used for colour separation in colour picture tubes), which has variably inclined through-thickness holes. Some examples of heterogeneous metallic microstructures are shown in Figure 1.1.

Determination of the macroscopic overall characteristics of heterogeneous media is an essential problem in many engineering applications. Studying the relation between microstructural phenomena and the macroscopic behaviour not only allows to predict the behaviour of existing multi-phase materials, but also provides a tool to design a material microstructure such that the resulting macroscopic behaviour exhibits the required characteristics. An additional challenge for multi-scale modelling is provided by ongoing technological developments, e.g. miniaturization of products and increasing complexity of forming operations. In micro and submicron applications the microstruc-

ture is no longer negligible with respect to the component size, thus giving rise to a so-called size effect. Furthermore, advanced forming operations force a material to undergo complex loading paths. This results in varying microstructural responses and easily provokes an evolution of the microstructure. From economical (time and costs) points of view, performing straightforward experimental measurements on a number of material samples of different sizes, for various geometrical and physical phase properties, volume fractions and loading paths is a hardly feasible task. Hence, there is a clear need for modelling strategies that provide a better understanding of micro-macro structure-property relations in multi-phase materials.

1.2 Modelling strategies for multi-phase materials

The simplest method leading to homogenized moduli of a heterogeneous material is based on the rule of mixtures. The overall property is then calculated as an average over the respective properties of the constituents, weighted with their volume fractions. This approach takes only one microstructural characteristic, the volume ratio of the heterogeneities, into consideration and, strictly speaking, denies the influence of other aspects.

A more sophisticated method is the effective medium approximation, as established by Eshelby (1957) and further developed by a number of authors, see, e.g. Hashin (1962); Budiansky (1965); Mori and Tanaka (1973). Equivalent material properties are derived as a result of the analytical (or semi-analytical) solution of a boundary value problem for a spherical or ellipsoidal inclusion of one material in an infinite matrix of another material. An extension of this method is the self-consistent approach, in which a particle of one phase is embedded into the effective material (the properties of which are not known a priori), Hill (1965); Christensen and Lo (1979). These strategies give a reasonable approximation for structures that possess some kind of geometrical regularity, but fail to describe the behaviour of clustered structures. Moreover, high contrasts between the properties of the phases cannot be represented accurately.

Although some work has been done on the extension of the self-consistent approach to non-linear cases (originating from the work by Hill (1965) who has proposed an “incremental” version of the self-consistent method), significantly more progress in estimating advanced properties of composites has been achieved by variational bounding methods, Hashin and Shtrikman (1963); Hashin (1983); Willis (1981); Ponte Castañeda and Suquet (1998). The variational bounding methods are based on suitable variational (minimum energy) principles and provide upper and lower bounds for the overall composite properties.

Another homogenization approach is based on the mathematical asymptotic homogenization theory, documented in Bensoussan et al. (1978); Sanchez-Palencia (1980). This method applies an asymptotic expansion of displacement and stress fields on the “natural length parameter”, which is the ratio of a characteristic size of the heterogeneities and a measure of the macrostructure, see, e.g. Tolenado and Murakami (1987); Devries et al. (1989); Guedes and Kikuchi (1990); Hollister and Kikuchi (1992); Fish et al. (1999). The asymptotic homogenization approach provides effective overall properties as well as local stress and strain values. However, usually the considerations are restricted to very simple microscopic geometries and simple material models, mostly at small strains. A comprehensive overview of different homogenization methods may

be found in Nemat-Nasser and Hori (1993).

The increasing complexity of microstructural mechanical and physical behaviour, along with the development of computational methods, made the class of so-called unit cell methods more attractive. These approaches have been used in a great number of different applications (e.g. Christman et al. (1989); Tvergaard (1990); Bao et al. (1991); Brockenbrough et al. (1991); Nakamura and Suresh (1993); McHugh et al. (1993a); van der Sluis et al. (1999a); van der Sluis (2001)). A selection of examples in the field of metal matrix composites has been collected, for example, in Suresh et al. (1993). The unit cell methods serve a twofold purpose: they provide valuable information on the local microstructural fields as well as the effective material properties. These properties are generally determined by fitting the averaged microscopical stress-strain fields, resulting from the analysis of a microstructural representative cell subjected to a certain loading path, on macroscopic closed-form phenomenological constitutive equations in a format established a priori. Once the constitutive behaviour becomes non-linear (geometrically, physically or both), it is extremely difficult to make a well-motivated assumption on a suitable macroscopic constitutive format. For example, McHugh et al. (1993b) have demonstrated that, when a composite is characterized by power-law slip system hardening, the power-law hardening behaviour is not preserved at the macroscale. Hence, most of the known homogenization techniques are not suitable for large deformations nor complex loading paths, neither do they account for the geometrical and physical changes of the microstructure (which is relevant, for example, when dealing with phase transformations in metals).

In recent years, a promising alternative approach for the homogenization of engineering materials has been developed, i.e. multi-scale computational homogenization, also called global-local analysis. The basic ideas of this approach have been presented in papers by Suquet (1985); Guedes and Kikuchi (1990); Terada and Kikuchi (1995); Ghosh et al. (1995, 1996) and further developed and improved in more recent works by Smit et al. (1998); Miehe et al. (1999b,a); Michel et al. (1999); Feyel and Chaboche (2000); Terada and Kikuchi (2001); Ghosh et al. (2001); Kouznetsova et al. (2001a); Miehe and Koch (2002). These micro-macro modelling procedures do not lead to closed-form overall constitutive equations, but compute the stress-strain relationship at every point of interest of the macrocomponent by detailed modelling of the microstructure attributed to that point. Techniques of this type (i) do not require any constitutive assumption on the macrolevel, (ii) enable the incorporation of large deformations and rotations on both micro and macrolevels, (iii) are suitable for arbitrary material behaviour, including physically non-linear and time dependent, (iv) provide the possibility to introduce detailed microstructural information, including the physical and geometrical evolution of the microstructure, into the macroscopic analysis and (v) allow the use of any modelling technique on the microlevel, e.g. the finite element method (Smit et al. (1998); Feyel and Chaboche (2000); Terada and Kikuchi (2001); Kouznetsova et al. (2001a)), the Voronoi cell method (Ghosh et al. (1995, 1996)), a crystal plasticity framework (Miehe et al. (1999b,a)) or numerical methods based on Fast Fourier Transforms (Michel et al. (1999); Moulinec and Suquet (1998)).

Although the fully coupled micro-macro technique is still computationally rather expensive, this concern can be overcome by parallel computation (Feyel and Chaboche (2000)). Another option is selective usage, where non-critical regions are modelled by continuum closed-form homogenized constitutive relations or by the constitutive

tangents obtained from the microstructural analysis but kept constant in the elastic domain, while in the critical regions the multi-scale analysis of the microstructure is fully performed (Ghosh et al. (2001)). Despite the required computational efforts, the numerical homogenization approach seems to be a versatile tool to establish micro-macro structure-property relations in materials, where the collective behaviour of an evolving multi-phase heterogeneous material is not yet possible to predict by any other method. Moreover, this micro-macro modelling technique is useful for constructing, evaluating and verifying other homogenization methods or micromechanically based macroscopic constitutive models.

The computational homogenization techniques developed until now are built entirely within a standard local continuum mechanics concept, where the response at a (macroscopic) material point depends only on the first gradient of the displacement field. Thus, throughout the present work, the classical computational homogenization methods will be referred to as “first-order”.

Two major disadvantages of the existing first-order micro-macro computational approaches (as well as conventional homogenization methods), which significantly limit their applicability, are to be mentioned. First, even though these techniques can account for the volume fraction, distribution and morphology of the constituents, they cannot take into account the absolute size of the microstructure and consequently fail to account for geometrical size effects. Another difficulty arises from the intrinsic assumption of uniformity of the macroscopic (stress-strain) fields attributed to each microstructural representative cell. This uniformity assumption relies on the concept of separation of scales and is not appropriate in critical regions of high gradients, where the macroscopic fields can vary rapidly.

To address these problems, a second-order computational homogenization procedure, that extends the classical computational homogenization technique to a full gradient geometrically non-linear approach, is proposed in this thesis (Kouznetsova et al. (2002)). In this framework, leading to a second gradient macroscopic continuum, the macroscopic deformation tensor and its gradient (i.e. the first and the second gradient of the displacement field, thus the name “second-order”) are used to prescribe the essential boundary conditions on a microstructural representative volume element (RVE). For the RVE boundary conditions, the well-known periodic boundary conditions are generalized. At the small RVE scale all microstructural constituents are still treated as an ordinary continuum, described by standard first-order equilibrium and constitutive equations. Therefore the microstructural boundary value problem remains actually classical, so that the solution is readily obtained without any complications. From the solution of the RVE boundary value problem, the macroscopic stress tensor and a higher-order stress tensor are extracted by exploiting an enhanced Hill-Mandel condition. This automatically delivers the microstructurally based constitutive response of the higher-order macrocontinuum, which deals with the macroscopic size effects and macroscopic localization phenomena (high deformation gradients) in a natural way.

1.3 Scope and outline

The aim of this thesis is to develop a computational homogenization technique for the multi-scale modelling of non-linear deformation processes of evolving multi-phase materials.

In chapter 2 the classical first-order computational homogenization approach is introduced. Details on the formulation of the microscopic boundary value problem and the micro-macro coupling in a geometrically and physically non-linear framework are given. The implementation of the first-order computational homogenization scheme in a finite element framework is briefly discussed. An example of the first-order computational homogenization modelling is presented, followed by a discussion of the classical concept of a representative volume element. Finally, some intrinsic limitations of the first-order framework are pointed out.

In order to eliminate these limitations, in chapter 3 the novel second-order computational homogenization scheme is presented. The microstructural boundary conditions and the relations for the determination of the averaged stress measures are elaborated. The extraction of the macroscopic constitutive tangents from the microstructural stiffness is treated in detail. The solution scheme of the coupled second-order multi-scale computational analysis is outlined. Chapter 3 ends with some remarks on the notion of a representative volume element in the second-order computational homogenization approach.

In the framework of the second-order computational homogenization a proper description of the macroscopic homogenized continuum requires a full second gradient equilibrium formulation. In chapter 4 the continuum description for the second gradient medium is presented and the finite element computational strategy is developed and validated.

Chapter 5 presents some illustrative examples of the second-order computational homogenization analysis. The main focus is on the comparison of the performance of the first- and second-order techniques, which allows a definition of their range of applicability and indicates when the second-order scheme is necessary to obtain physically meaningful results.

Finally, chapter 6 gives a brief summary of the conclusions and recommendations on the practical use of the computational homogenization techniques given attention in this thesis. Perspectives of future developments in computational homogenization strategies are shortly discussed.

Chapter 2

First-order computational homogenization

In this chapter the first-order computational homogenization strategy is presented. The key components of the computational homogenization scheme, i.e. the formulation of the microstructural boundary value problem and the coupling between the micro and macrolevel based on the averaging theorems, are treated in detail. Some aspects of the numerical implementation of the framework, particularly the computation of the macroscopic consistent tangent operator based on the total microstructural stiffness, are discussed. The performance of the method is illustrated by the simulation of pure bending of porous aluminum. The classical notion of a representative volume element is introduced and the influence of the spatial distribution of heterogeneities on the overall macroscopic behaviour is investigated by comparing the results of multi-scale modelling for regular and random structures.

2.1 Introduction

Computational homogenization is a multi-scale technique, which is essentially based on the derivation of the local macroscopic constitutive response (input leading to output, e.g. stress driven by deformation) from the underlying microstructure through the adequate construction and solution of a microstructural boundary value problem.

The basic principles of the classical first-order computational homogenization have gradually evolved from the concepts employed in other homogenization methods and may be fit into the four-step homogenization scheme established by Suquet (1985): (i) definition of a microstructural representative volume element (RVE), of which the constitutive behaviour of individual constituents is assumed to be known; (ii) formulation of the microscopic boundary conditions from the macroscopic input variables and their application on the RVE (macro-to-micro transition); (iii) calculation of the macroscopic output variables from the analysis of the deformed microstructural RVE (micro-to-macro transition); (iv) obtaining the (numerical) relation between the macroscopic

input and output variables. The main ideas of the first-order computational homogenization have been established in papers by Suquet (1985); Guedes and Kikuchi (1990); Terada and Kikuchi (1995); Ghosh et al. (1995, 1996) and further developed and improved in more recent works by Smit et al. (1998); Smit (1998); Miehe et al. (1999b); Miehe and Koch (2002); Michel et al. (1999); Feyel and Chaboche (2000); Terada and Kikuchi (2001); Ghosh et al. (2001); Kouznetsova et al. (2001a).

Among several advantageous characteristics of the computational homogenization technique the following are worth to be mentioned: (i) no explicit assumptions on the format of the macroscopic local constitutive response are required at the macroscale, since the macroscopic constitutive behaviour is obtained from the solution of the associated microscale boundary value problem; (ii) the macroscopic constitutive tangent operator is derived from the total microscopic stiffness matrix through static condensation; (iii) consistency is preserved through this scale transition; (iv) the method deals with large strains and large rotations in a trivial way, if the microstructural constituents are properly modelled within a geometrically non-linear framework. Different phases present in the microstructure can be characterized by arbitrary physically non-linear constitutive models. The RVE problem is a classical boundary value problem, for which any appropriate solution strategy can be used.

Despite rather high computational efforts involved in the fully coupled multi-scale analysis (i.e. the solution of a nested boundary value problem), the computational homogenization technique has proven to be a valuable tool to establish non-linear micro-macro structure-property relations, especially in the cases where the complexity of the mechanical and geometrical microstructural properties and the evolving character prohibit the use of other homogenization methods.

This chapter presents the essential ingredients of the first-order computational homogenization technique. The basic underlying hypotheses and general concepts are summarized in section 2.2. The microstructural boundary value problem is defined in section 2.3. Section 2.4 deals with the coupling between micro and macrovariables. In the large deformation framework the importance of a careful choice of the deformation and stress measures, at the macroscopic level obtained as the volume average of the microstructural counterparts, is emphasized. Numerical extraction of the macroscopic consistent constitutive tangent from the microscopic overall stiffness is treated in section 2.4.4. Some implementation details and the solution scheme are briefly summarized in section 2.5. A numerical example, the first-order computational homogenization analysis of bending of voided aluminum is presented in section 2.6. Section 2.7 discusses the classical notion of a representative volume element and investigates the influence of the spatial arrangement of the microstructural heterogeneities on the overall response for different material models and loading histories. The chapter concludes with a discussion, addressing some intrinsic limitations of the first-order framework.

2.2 Basic hypotheses

The material configuration to be considered is assumed to be macroscopically sufficiently homogeneous, but microscopically heterogeneous (the morphology consists of distinguishable components as e.g. inclusions, grains, interfaces, cavities). This is schematically illustrated in Figure 2.1. The microscopic length scale is much larger than the molecular dimensions, so that a continuum approach is justified for every

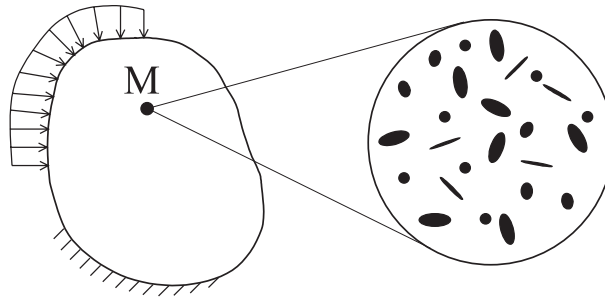


Figure 2.1: Continuum macrostructure and heterogeneous microstructure associated with the macroscopic point M .

constituent. At the same time, in the context of the principle of separation of scales, the microscopic length scale should be much smaller than the characteristic size of the macroscopic sample or the wave length of the macroscopic loading.

Most of the homogenization approaches make an assumption on global periodicity of the microstructure, suggesting that the whole macroscopic specimen consists of spatially repeated unit cells. In the computational homogenization approach a more realistic assumption on local periodicity is proposed, i.e. the microstructure can have different morphologies corresponding to different macroscopic points, while it repeats itself in a small vicinity of each individual macroscopic point. The concept of local and global periodicity is schematically illustrated in Figure 2.2. The assumption of local periodicity adopted in the computational homogenization allows the modelling of the effects of a non-uniform distribution of the microstructure on the macroscopic response (e.g. in functionally graded materials).

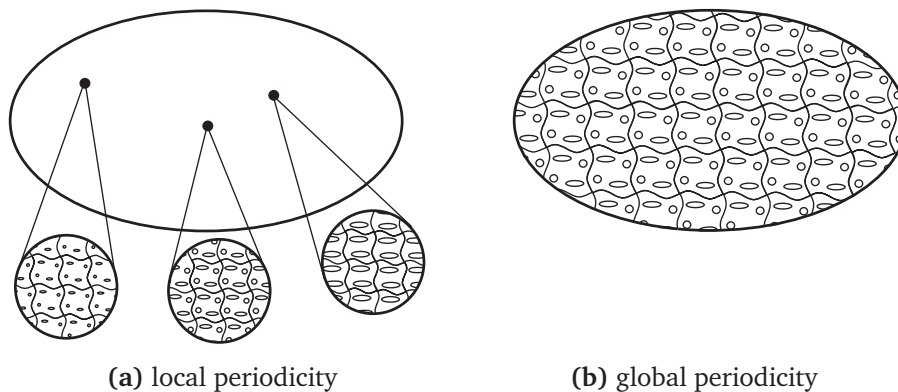


Figure 2.2: Schematic representation of a macrostructure with (a) a locally and (b) a globally periodic microstructure.

In the first-order computational homogenization procedure, a macroscopic deformation (gradient) tensor \mathbf{F}_M is calculated for every material point of the macrostructure (e.g. the integration points of the macroscopic mesh within a finite element environment). Here and in the following the subscript “M” refers to a macroscopic quantity, while the subscript “m” will denote a microscopic quantity. The deformation tensor \mathbf{F}_M for a macroscopic point is next used to formulate the boundary conditions to be imposed on the RVE that is assigned to this point. Upon the solution of the boundary value problem for the RVE, the macroscopic stress tensor \mathbf{P}_M is obtained by averaging the resulting RVE stress field over the volume of the RVE. As a result, the (numerical) stress-

deformation relationship at the macroscopic point is readily available. Additionally, the local macroscopic consistent tangent is derived from the microstructural stiffness. This framework is schematically illustrated in Figure 2.3.

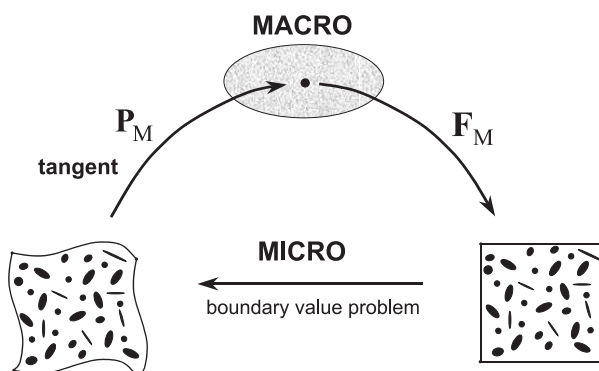


Figure 2.3: First-order computational homogenization scheme.

The micro-macro procedure outlined here is “deformation driven”, i.e. on the local macroscopic level the problem is formulated as follows: given a macroscopic deformation gradient tensor F_M , determine the stress P_M and the constitutive tangent, based on the response of the underlying microstructure. A “stress driven” procedure (given a local macroscopic stress, obtain the deformation) is also possible. However, such a procedure does not directly fit into the standard displacement-based finite element framework, which is usually employed for the solution of macroscopic boundary value problems. Moreover, in case of large deformations the macroscopic rotational effects have to be added to the stress tensor in order to uniquely determine the deformation gradient tensor, thus complicating the implementation. Therefore, the “stress driven” approach, which is often used in the analysis of single unit cells, is generally not adopted in coupled micro-macro computational homogenization strategies.

In the subsequent sections the essential steps of the first-order computational homogenization process are discussed in more detail. First the problem on the microlevel is defined, then the aspects of the coupling between micro and macrolevel are considered and finally the realization of the whole procedure within a finite element context is explained.

2.3 Definition of the problem on the microlevel

The physical and geometrical properties of the microstructure are identified by a representative volume element (RVE). An example of a typical two-dimensional RVE is depicted in Figure 2.4. The actual choice of the RVE is a rather delicate task. The RVE should be large enough to represent the microstructure, without introducing non-existing properties (e.g. undesired anisotropy) and at the same time it should be small enough to allow efficient computational modelling. Some issues related to the concept of a representative cell are discussed in section 2.7. Here it is supposed that an appropriate RVE has been already selected. Then the problem on RVE level can be formulated as a standard problem in quasi-static continuum solid mechanics.

The RVE deformation field in a point with the initial position vector \vec{X} (in the reference domain V_0) and the actual position vector \vec{x} (in the current domain V) is described

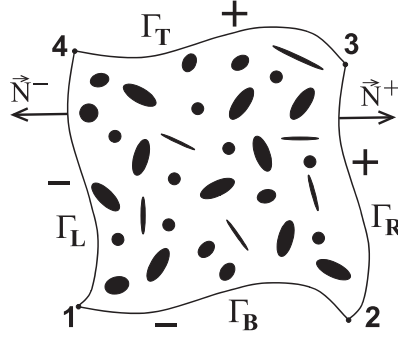


Figure 2.4: Schematic picture of a typical two-dimensional representative volume element (RVE).

by the microstructural deformation gradient tensor $\mathbf{F}_m = (\nabla_{0m}\vec{x})^c$, where the gradient operator ∇_{0m} is taken with respect to the reference microstructural configuration.

The RVE is in a state of equilibrium. This is mathematically reflected by the equilibrium equation in terms of the Cauchy stress tensor $\boldsymbol{\sigma}_m$ or, alternatively, in terms of the first Piola-Kirchhoff stress tensor $\mathbf{P}_m = \det(\mathbf{F}_m)\boldsymbol{\sigma}_m \cdot (\mathbf{F}_m^c)^{-1}$ according to (in the absence of body forces)

$$\nabla_m \cdot \boldsymbol{\sigma}_m = \vec{0} \quad \text{in } V, \quad \text{or} \quad \nabla_{0m} \cdot \mathbf{P}_m^c = \vec{0} \quad \text{in } V_0, \quad (2.1)$$

where ∇_m is the the gradient operator with respect to the current configuration of the microstructural cell.

The mechanical characterizations of the microstructural components are described by certain constitutive laws, specifying a time and history dependent stress-deformation relationship for every microstructural constituent

$$\boldsymbol{\sigma}_m^{(\alpha)}(t) = \mathcal{F}_\sigma^{(\alpha)} \{ \mathbf{F}_m^{(\alpha)}(\tau), \tau \in [0, t] \}, \quad \text{or} \quad \mathbf{P}_m^{(\alpha)}(t) = \mathcal{F}_P^{(\alpha)} \{ \mathbf{F}_m^{(\alpha)}(\tau), \tau \in [0, t] \}, \quad (2.2)$$

where t denotes the current time; $\alpha = \overline{1, N}$, with N the number of microstructural constituents (e.g. matrix, inclusion, etc.) to be distinguished.

The actual macro-to-micro transition is performed by imposing the macroscopic deformation gradient tensor \mathbf{F}_M on the microstructural RVE through a specific approach. Probably the simplest way is to assume that all the microstructural constituents undergo a constant deformation identical to the macroscopic one. In the literature this is called the Taylor (or Voigt) assumption. Another simple strategy is to assume an identical constant stress (and additionally identical rotation) in all the components. This is called the Sachs (or Reuss) assumption. Also some intermediate procedures are possible, where the Taylor and Sachs assumptions are applied only to certain components of the deformation and stress tensors. All these simplified procedures do not really require a detailed microstructural modelling. Accordingly, they generally provide very rough estimates of the overall material properties and are hardly suitable in the non-linear deformation regimes. The Taylor assumption usually overestimates the overall stiffness, while the Sachs assumption leads to an underestimation of the stiffness. Nevertheless, the Taylor and Sachs averaging procedures are sometimes used to quickly obtain a first estimate of the composite's overall stiffness. The Taylor assumption and some intermediate procedures are often employed in multi-crystal plasticity modelling.

More accurate averaging strategies that do require the solution of the detailed microstructural boundary value problem transfer the given macroscopic variables to the microstructural RVE via the boundary conditions. Classically three types of RVE boundary conditions are used, i.e. prescribed displacements, prescribed tractions and prescribed periodicity.

In the case of prescribed displacement boundary conditions, the position vector of a point on the RVE boundary in the deformed state is given by

$$\vec{x} = \mathbf{F}_M \cdot \vec{X} \quad \text{with} \quad \vec{X} \quad \text{on} \quad \Gamma_0, \quad (2.3)$$

where Γ_0 denotes the undeformed boundary of the RVE. This condition prescribes a linear mapping of the RVE boundary.

For the traction boundary conditions it is prescribed

$$\vec{t} = \vec{n} \cdot \boldsymbol{\sigma}_M \quad \text{on} \quad \Gamma, \quad \text{or} \quad \vec{p} = \vec{N} \cdot \mathbf{P}_M^c \quad \text{on} \quad \Gamma_0, \quad (2.4)$$

with \vec{n} and \vec{N} the normals to the current (Γ) and initial (Γ_0) RVE boundaries, respectively. However, the traction boundary conditions (2.4) do not completely define the microstructural boundary value problem, as discussed at the end of section 2.2. Moreover, they are not appropriate in the deformation driven procedure to be pursued in the present computational homogenization scheme. Therefore, the RVE traction boundary conditions are not used in the actual implementation of the coupled computational homogenization scheme; they were presented here for the sake of generality only.

Based on the assumption of microstructural periodicity presented in section 2.2, periodic boundary conditions are introduced. The periodicity conditions for the microstructural RVE are written in a general format as

$$\vec{x}^+ - \vec{x}^- = \mathbf{F}_M \cdot (\vec{X}^+ - \vec{X}^-), \quad (2.5)$$

$$\vec{p}^+ = -\vec{p}^-, \quad (2.6)$$

representing periodic deformations (2.5) and antiperiodic tractions (2.6) on the boundary of the RVE. Here the (opposite) parts of the RVE boundary Γ_0^- and Γ_0^+ are defined such that $\vec{N}^- = -\vec{N}^+$ at corresponding points on Γ_0^- and Γ_0^+ , see Figure 2.4. The periodicity condition (2.5), being prescribed on an initially periodic RVE, preserves the periodicity of the RVE in the deformed state. Also it should be mentioned that, as has been observed by several authors (e.g. van der Sluis et al. (2000); Terada et al. (2000)), the periodic boundary conditions provide a better estimation of the overall properties, than the prescribed displacement or prescribed traction boundary conditions (see also the discussion in section 2.7.1).

For the two-dimensional RVE depicted in Figure 2.4 the periodicity condition (2.5) may be recast into the following constraint relations (more suitable for the actual implementation)

$$\vec{x}_R = \vec{x}_L + \vec{x}_2 - \vec{x}_1, \quad (2.7)$$

$$\vec{x}_T = \vec{x}_B + \vec{x}_4 - \vec{x}_1, \quad (2.8)$$

where \vec{x}_L , \vec{x}_R , \vec{x}_B and \vec{x}_T denote a position vector on the left, right, bottom and top boundary of the RVE, respectively; \vec{x}_i , $i = 1, 2, 4$ are the position vectors of the corner

points 1, 2 and 4 in the deformed state. These position vectors are prescribed according to

$$\vec{x}_i = \mathbf{F}_M \cdot \vec{X}_i, \quad i = 1, 2, 4. \quad (2.9)$$

Other types of RVE boundary conditions are possible. The only general requirement is that they should be consistent with the so-called averaging theorems. The averaging theorems, dealing with the coupling between the micro and macrolevels in an energetically consistent way, will be presented in the next section. The consistency of the three types of boundary conditions presented above with these averaging theorems will be verified.

2.4 Coupling of the macroscopic and microscopic levels

The actual coupling between the macroscopic and microscopic levels is based on averaging theorems. The integral averaging expressions have been initially proposed by Hill (1963) for small deformations and later extended to a large deformation framework by Hill (1984) and Nemat-Nasser (1999).

2.4.1 Deformation

The first of the averaging relations concerns the micro-macro coupling of kinematic quantities. It is postulated that the macroscopic deformation gradient tensor \mathbf{F}_M is the volume average of the microstructural deformation gradient tensor \mathbf{F}_m

$$\mathbf{F}_M = \frac{1}{V_0} \int_{V_0} \mathbf{F}_m \, dV_0 = \frac{1}{V_0} \int_{\Gamma_0} \vec{x} \vec{N} \, d\Gamma_0, \quad (2.10)$$

where the divergence theorem has been used to transform the integral over the undeformed volume V_0 of the RVE to a surface integral.

Verification that the use of the prescribed displacement boundary conditions (2.3) indeed leads to satisfaction of (2.10) is rather trivial. Substitution of (2.3) into (2.10) and use of the divergence theorem with account for $\nabla_{0m} \vec{X} = \mathbf{I}$ gives

$$\mathbf{F}_M = \frac{1}{V_0} \int_{\Gamma_0} (\mathbf{F}_M \cdot \vec{X}) \vec{N} \, d\Gamma_0 = \frac{1}{V_0} \mathbf{F}_M \cdot \int_{\Gamma_0} \vec{X} \vec{N} \, d\Gamma_0 = \frac{1}{V_0} \mathbf{F}_M \cdot \int_{V_0} (\nabla_{0m} \vec{X})^c \, dV_0 = \mathbf{F}_M. \quad (2.11)$$

The validation for the periodic boundary conditions (2.5) follows the same lines except that the RVE boundary is split into the parts Γ_0^+ and Γ_0^-

$$\begin{aligned} \mathbf{F}_M &= \frac{1}{V_0} \left\{ \int_{\Gamma_0^+} \vec{x}^+ \vec{N}^+ \, d\Gamma_0 + \int_{\Gamma_0^-} \vec{x}^- \vec{N}^- \, d\Gamma_0 \right\} = \frac{1}{V_0} \int_{\Gamma_0^+} (\vec{x}^+ - \vec{x}^-) \vec{N}^+ \, d\Gamma_0 \\ &= \frac{1}{V_0} \mathbf{F}_M \cdot \int_{\Gamma_0^+} (\vec{X}^+ - \vec{X}^-) \vec{N}^+ \, d\Gamma_0 = \frac{1}{V_0} \mathbf{F}_M \cdot \int_{\Gamma_0} \vec{X} \vec{N} \, d\Gamma_0 = \mathbf{F}_M. \end{aligned} \quad (2.12)$$

In the general case of large strains and large rotations, attention should be given to the fact that due to the non-linear character of the relations between different kinematic measures not all macroscopic kinematic quantities may be obtained as the volume

average of their microstructural counterparts. For example, the volume average of the Green-Lagrange strain tensor

$$\mathbf{E}_M^* = \frac{1}{2V_0} \int_{V_0} (\mathbf{F}_m^c \cdot \mathbf{F}_m - \mathbf{I}) dV_0 \quad (2.13)$$

is in general not equal to the macroscopic Green-Lagrange strain obtained according to

$$\mathbf{E}_M = \frac{1}{2}(\mathbf{F}_M^c \cdot \mathbf{F}_M - \mathbf{I}). \quad (2.14)$$

2.4.2 Stress

Similarly, the averaging relation for the first Piola-Kirchhoff stress tensor is established as

$$\mathbf{P}_M = \frac{1}{V_0} \int_{V_0} \mathbf{P}_m dV_0. \quad (2.15)$$

In order to express the macroscopic first Piola-Kirchhoff stress tensor \mathbf{P}_M in the microstructural quantities defined on the RVE surface, the following relation is used (with account for microscopic equilibrium $\nabla_{0m} \cdot \mathbf{P}_m^c = \vec{0}$ and the equality $\nabla_{0m} \vec{X} = \mathbf{I}$)

$$\mathbf{P}_m = (\nabla_{0m} \cdot \mathbf{P}_m^c) \vec{X} + \mathbf{P}_m \cdot (\nabla_{0m} \vec{X}) = \nabla_{0m} \cdot (\mathbf{P}_m^c \vec{X}). \quad (2.16)$$

Substitution of (2.16) into (2.15), application of the divergence theorem and the definition of the first Piola-Kirchhoff stress vector $\vec{p} = \vec{N} \cdot \mathbf{P}_m^c$ gives

$$\mathbf{P}_M = \frac{1}{V_0} \int_{V_0} \nabla_{0m} \cdot (\mathbf{P}_m^c \vec{X}) dV_0 = \frac{1}{V_0} \int_{\Gamma_0} \vec{N} \cdot \mathbf{P}_m^c \vec{X} d\Gamma_0 = \frac{1}{V_0} \int_{\Gamma_0} \vec{p} \vec{X} d\Gamma_0. \quad (2.17)$$

Now it is a trivial task to validate that substitution of the traction boundary conditions (2.4₂) into this equation leads to an identity.

After the solution of the microstructural RVE boundary value problem with an appropriate solution technique (i.e. finite elements) the macroscopic stress \mathbf{P}_M is obtained by numerical evaluation of the boundary integral (2.17). For the case of prescribed displacement boundary conditions this simply leads to

$$\mathbf{P}_M = \frac{1}{V_0} \sum_{i=1}^{N_p} \vec{f}_i \vec{X}_i, \quad (2.18)$$

where \vec{f}_i are the resulting external forces at the boundary nodes and \vec{X}_i the position vectors of these nodes in the undeformed state; N_p is the number of the nodes on the boundary. Using the periodicity conditions (2.7)-(2.9) for the two-dimensional configuration depicted in Figure 2.4, it can be verified that the only contribution to the boundary integral (2.17) is offered by the external forces at the three prescribed corner nodes

$$\mathbf{P}_M = \frac{1}{V_0} \sum_{i=1,2,4} \vec{f}_i \vec{X}_i. \quad (2.19)$$

The volume average of the microscopic Cauchy stress tensor $\boldsymbol{\sigma}_m$ over the current RVE volume V can be elaborated similarly to (2.17)

$$\boldsymbol{\sigma}_M^* = \frac{1}{V} \int_V \boldsymbol{\sigma}_m \, dV = \frac{1}{V} \int_{\Gamma} \vec{t} \vec{x} \, d\Gamma. \quad (2.20)$$

Just as it is the case for kinematic quantities, the usual continuum mechanics relation between stress measures (e.g. the Cauchy and the first Piola-Kirchhoff stress tensors) is, in general, not valid for the volume averages of the microstructural counterparts $\boldsymbol{\sigma}_M^* \neq \mathbf{P}_M \cdot \mathbf{F}_M^c / \det(\mathbf{F}_M)$. However, the Cauchy stress tensor on the macrolevel should be defined as

$$\boldsymbol{\sigma}_M = \frac{1}{\det(\mathbf{F}_M)} \mathbf{P}_M \cdot \mathbf{F}_M^c. \quad (2.21)$$

Clearly, there is some arbitrariness in the choice of associated deformation and stress quantities, whose macroscopic measures are obtained as a volume average of their microscopic counterparts. The remaining macroscopic measures are then expressed in terms of these averaged quantities using the standard continuum mechanics relations. The specific selection should be made with care and based on experimental results and convenience of the implementation. The actual choice of the “primary” averaging measures: the deformation gradient tensor \mathbf{F} and the first Piola-Kirchhoff stress tensor \mathbf{P} (and their rates) has been advocated by Hill (1984), Nemat-Nasser (1999) and Miehe et al. (1999b) (in the first two references the nominal stress $\mathbf{S}_N = \det(\mathbf{F})\mathbf{F}^{-1} \cdot \boldsymbol{\sigma} = \mathbf{P}^c$ has been used). This particular choice is motivated by the fact that these two measures are work conjugated, combined with the observation that their volume averages can exclusively be defined in terms of the microstructural quantities on the RVE boundary only. This feature will be used in the next section, where the averaging theorem for the micro-macro energy transition is discussed.

2.4.3 Internal work

The energy averaging theorem, known in the literature as the Hill-Mandel condition or macrohomogeneity condition (Hill (1963); Suquet (1985)), requires that the macroscopic volume average of the variation of work performed on the RVE is equal to the local variation of the work on the macroscale. Formulated in terms of a work conjugated set, i.e. the deformation gradient tensor and the first Piola-Kirchhoff stress tensor, the Hill-Mandel condition reads

$$\frac{1}{V_0} \int_{V_0} \mathbf{P}_m : \delta \mathbf{F}_m^c \, dV_0 = \mathbf{P}_M : \delta \mathbf{F}_M^c, \quad \forall \delta \vec{x}. \quad (2.22)$$

The averaged microstructural work in the left-hand side of (2.22) may be expressed in terms of RVE surface quantities

$$\delta W_{0M} = \frac{1}{V_0} \int_{V_0} \mathbf{P}_m : \delta \mathbf{F}_m^c \, dV_0 = \frac{1}{V_0} \int_{\Gamma_0} \vec{p} \cdot \delta \vec{x} \, d\Gamma_0, \quad (2.23)$$

where the relation (with account for microstructural equilibrium)

$$\mathbf{P}_m : \nabla_{0m} \delta \vec{x} = \nabla_{0m} \cdot (\mathbf{P}_m^c \cdot \delta \vec{x}) - (\nabla_{0m} \cdot \mathbf{P}_m^c) \cdot \delta \vec{x} = \nabla_{0m} \cdot (\mathbf{P}_m^c \cdot \delta \vec{x}),$$

and the divergence theorem have been used.

Now it is easy to verify that the three types of boundary conditions: prescribed displacements (2.3), prescribed tractions (2.4) or the periodicity conditions (2.5) and (2.6) all satisfy the Hill-Mandel condition a priori, if the averaging relations for the deformation gradient tensor (2.10) and for the first Piola-Kirchhoff stress tensor (2.15) are adopted. In case of the prescribed displacements (2.3), substitution of the variation of the boundary position vectors $\delta\vec{x} = \delta\mathbf{F}_M \cdot \vec{X}$ into the expression for the averaged microwork (2.23) with incorporation of (2.17) gives

$$\delta W_{0M} = \frac{1}{V_0} \int_{\Gamma_0} \vec{p} \cdot (\delta\mathbf{F}_M \cdot \vec{X}) \, d\Gamma_0 = \frac{1}{V_0} \int_{\Gamma_0} \vec{p} \vec{X} \, d\Gamma_0 : \delta\mathbf{F}_M^c = \mathbf{P}_M : \delta\mathbf{F}_M^c. \quad (2.24)$$

Similarly, substitution of the traction boundary condition (2.4) into (2.23), with account for the variation of the macroscopic deformation gradient tensor obtained by varying relation (2.10), leads to

$$\delta W_{0M} = \frac{1}{V_0} \int_{\Gamma_0} (\vec{N} \cdot \mathbf{P}_M^c) \cdot \delta\vec{x} \, d\Gamma_0 = \mathbf{P}_M : \frac{1}{V_0} \int_{\Gamma_0} \vec{N} \delta\vec{x} \, d\Gamma_0 = \mathbf{P}_M : \delta\mathbf{F}_M^c. \quad (2.25)$$

Finally, for the periodic boundary conditions (2.5) and (2.6)

$$\begin{aligned} \delta W_{0M} &= \frac{1}{V_0} \left\{ \int_{\Gamma_0^+} \vec{p}^+ \cdot \delta\vec{x}^+ \, d\Gamma_0 + \int_{\Gamma_0^-} \vec{p}^- \cdot \delta\vec{x}^- \, d\Gamma_0 \right\} = \frac{1}{V_0} \int_{\Gamma_0^+} \vec{p}^+ \cdot (\delta\vec{x}^+ - \delta\vec{x}^-) \, d\Gamma_0 \\ &= \frac{1}{V_0} \int_{\Gamma_0} \vec{p}^+ (\vec{X}^+ - \vec{X}^-) \, d\Gamma_0 : \delta\mathbf{F}_M^c = \frac{1}{V_0} \int_{\Gamma_0} \vec{p} \vec{X} \, d\Gamma_0 : \delta\mathbf{F}_M^c = \mathbf{P}_M : \delta\mathbf{F}_M^c. \end{aligned} \quad (2.26)$$

2.4.4 Consistent tangent stiffness

When the micro-macro approach is implemented within the framework of a non-linear finite element code, the stiffness matrix at every macroscopic integration point is required. Because in the computational homogenization approach there is no explicit form of the constitutive behaviour on the macrolevel assumed a priori, the stiffness matrix has to be determined numerically from the relation between variations of the macroscopic stress and variations of the macroscopic deformation at such a point. This may be realized by numerical differentiation of the numerical macroscopic stress-strain relation, for example using a forward difference approximation as has been suggested by Miehe (1996). Another approach is to condense the microstructural stiffness to the local macroscopic stiffness. This is achieved by reducing the total RVE system of equations to the relation between the forces acting on the RVE boundary and the associated boundary displacements. Such a procedure in combination with the Lagrange multiplier method to impose boundary constraints has been recently elaborated by Miehe and Koch (2002). In the present work an alternative scheme, which employs the direct condensation of the constrained degrees of freedom, as has been presented in Kouznetsova et al. (2001a), is used.

First, consider the case of fully prescribed boundary displacements (2.3). The total microstructural system of equations is rearranged to the form

$$\begin{bmatrix} \underline{K}_{pp} & \underline{K}_{pf} \\ \underline{K}_{fp} & \underline{K}_{ff} \end{bmatrix} \begin{bmatrix} \delta\tilde{u}_p \\ \delta\tilde{u}_f \end{bmatrix} = \begin{bmatrix} \delta f_p \\ \underline{0} \end{bmatrix}, \quad (2.27)$$

where $\delta \underline{u}_p$ and $\delta \underline{f}_p$ are the columns with iterative displacements and external forces of the boundary nodes and $\delta \underline{u}_f$ the column with the iterative displacements of the remaining (interior) nodes; \underline{K}_{pp} , \underline{K}_{pf} , \underline{K}_{fp} and \underline{K}_{ff} are the corresponding partitions of the total RVE stiffness matrix. The stiffness matrix in the formulation (2.27) is taken at the end of a microstructural increment, where a converged state is reached. Equation (2.27) may be rewritten to obtain the reduced stiffness matrix \underline{K}_M relating boundary displacement variations to boundary force variations

$$\underline{K}_M \delta \underline{u}_p = \delta \underline{f}_p, \quad \text{with} \quad \underline{K}_M = \underline{K}_{pp} - \underline{K}_{pf} (\underline{K}_{ff})^{-1} \underline{K}_{fp}. \quad (2.28)$$

Next, the case of the periodic boundary conditions is elaborated. Here the two-dimensional RVE, as depicted in Figure 2.4 is considered, so the periodic boundary conditions in the form (2.7)-(2.9) are used. In the following it is (implicitly) supposed that the finite element discretization is performed such that the distribution of nodes on opposite RVE edges is equal. In the discretized format, (2.7) and (2.8) may then easily be written as $\delta \underline{u}_d = \underline{C}_{di} \delta \underline{u}_i$, with \underline{u}_i the independent degrees of freedom (to be retained in the system) and \underline{u}_d dependent degrees of freedom (to be eliminated from the system); \underline{C}_{di} is the dependency matrix. Elimination of the dependent degrees of freedom from the total system of equations is a standard procedure in structural mechanics, see for example Cook et al. (1989). Following this procedure the total linearized RVE system of equations, which is partitioned according to

$$\begin{bmatrix} \underline{K}_{ii} & \underline{K}_{id} \\ \underline{K}_{di} & \underline{K}_{dd} \end{bmatrix} \begin{bmatrix} \delta \underline{u}_i \\ \delta \underline{u}_d \end{bmatrix} = \begin{bmatrix} \delta \underline{r}_i \\ \delta \underline{r}_d \end{bmatrix}, \quad (2.29)$$

is condensed to a system where only the independent degrees of freedom are retained

$$\underline{K}^* \delta \underline{u}_i = \delta \underline{r}^*, \quad (2.30)$$

$$\text{with} \quad \underline{K}^* = \underline{K}_{ii} + \underline{K}_{id} \underline{C}_{di} + \underline{C}_{di}^T \underline{K}_{di} + \underline{C}_{di}^T \underline{K}_{dd} \underline{C}_{di}, \quad (2.31)$$

$$\delta \underline{r}^* = \delta \underline{r}_i + \underline{C}_{di}^T \delta \underline{r}_d. \quad (2.32)$$

Next, system (2.30) is further split, similarly to (2.27), into the parts corresponding to the variations of the prescribed degrees of freedom $\delta \underline{u}_p$, which in this case are the varied positions of the three corner nodes prescribed according to (2.9), variations of the external forces at these prescribed nodes denoted by $\delta \underline{f}_p^*$, and the remaining (free) displacement variations $\delta \underline{u}_f$:

$$\begin{bmatrix} \underline{K}_{pp}^* & \underline{K}_{pf}^* \\ \underline{K}_{fp}^* & \underline{K}_{ff}^* \end{bmatrix} \begin{bmatrix} \delta \underline{u}_p \\ \delta \underline{u}_f \end{bmatrix} = \begin{bmatrix} \delta \underline{f}_p^* \\ \underline{0} \end{bmatrix}. \quad (2.33)$$

Then the reduced stiffness matrix \underline{K}_M^* in case of periodic boundary conditions is obtained as

$$\underline{K}_M^* \delta \underline{u}_p = \delta \underline{f}_p^*, \quad \text{with} \quad \underline{K}_M^* = \underline{K}_{pp}^* - \underline{K}_{pf}^* (\underline{K}_{ff}^*)^{-1} \underline{K}_{fp}^*. \quad (2.34)$$

Note that \underline{K}_M^* is $[6 \times 6]$ matrix only (in the two-dimensional case).

Condensation of the RVE stiffness matrix in case of the prescribed boundary tractions (2.4) is left out of consideration here.

Finally, the resulting relation between displacement and force variations (relation (2.28) if prescribed displacement boundary conditions are used, or relation (2.34) if

periodicity conditions are employed) needs to be transformed to arrive at an expression relating variations of the macroscopic stress and deformation tensors

$$\delta \mathbf{P}_M = {}^4\mathbf{C}_M^P : \delta \mathbf{F}_M^c, \quad (2.35)$$

where the fourth order tensor ${}^4\mathbf{C}_M^P$ represents the required consistent tangent stiffness at the macroscopic integration point level.

In order to obtain this constitutive tangent from the reduced stiffness matrix \underline{K}_M (or \underline{K}_M^*), first relations (2.28) and (2.34) are rewritten in a specific vector/tensor format

$$\sum_j \mathbf{K}_M^{(ij)} \cdot \delta \vec{u}_{(j)} = \delta \vec{f}_{(i)}, \quad (2.36)$$

where indices i and j take the values $i, j = \overline{1, N_p}$ for prescribed displacement boundary conditions (N_p is the number of boundary nodes) and $i, j = 1, 2, 4$ for periodic boundary conditions on the two-dimensional configuration depicted in Figure 2.4. In (2.36) the components of the tensors $\mathbf{K}_M^{(ij)}$ are simply found in the tangent matrix \underline{K}_M (for displacement boundary conditions) or in the matrix \underline{K}_M^* (for periodic boundary conditions) at the rows and columns of the degrees of freedom in the nodes i and j . Next, the expression for the variation of the nodal forces (2.36) is substituted into the relation for the variation of the macroscopic stress following from (2.18) or (2.19)

$$\delta \mathbf{P}_M = \frac{1}{V_0} \sum_i \sum_j (\mathbf{K}_M^{(ij)} \cdot \delta \vec{u}_{(j)}) \vec{X}_{(i)}. \quad (2.37)$$

Substitution of the equation $\delta \vec{u}_{(j)} = \vec{X}_{(j)} \cdot \delta \mathbf{F}_M^c$ into (2.37) gives

$$\delta \mathbf{P}_M = \frac{1}{V_0} \sum_i \sum_j (\vec{X}_{(i)} \mathbf{K}_M^{(ij)} \vec{X}_{(j)})^{LC} : \delta \mathbf{F}_M^c, \quad (2.38)$$

where the superscript LC denotes left conjugation, which for a fourth-order tensor ${}^4\mathbf{T}$ is defined as $T_{ijkl}^{LC} = T_{jikl}$. Finally, by comparing (2.38) with (2.35) the consistent constitutive tangent is identified as

$${}^4\mathbf{C}_M^P = \frac{1}{V_0} \sum_i \sum_j (\vec{X}_{(i)} \mathbf{K}_M^{(ij)} \vec{X}_{(j)})^{LC}. \quad (2.39)$$

If the macroscopic finite element scheme requires the constitutive tangent relating the variation of the macroscopic Cauchy stress to the variation of the macroscopic deformation gradient tensor according to

$$\delta \boldsymbol{\sigma}_M = {}^4\mathbf{C}_M^\sigma : \delta \mathbf{F}_M^c, \quad (2.40)$$

this tangent may be obtained by varying the definition equation of the macroscopic Cauchy stress tensor (2.21), followed by substitution of (2.18) (or (2.19)) and (2.38). This gives

$$\delta \boldsymbol{\sigma}_M = \left[\frac{1}{V} \sum_i \sum_j (\vec{x}_{(i)} \mathbf{K}_M^{(ij)} \vec{x}_{(j)})^{LC} + \frac{1}{V} \sum_i \vec{f}_{(i)} \mathbf{I} \vec{X}_{(i)} - \boldsymbol{\sigma}_M \mathbf{F}_M^{-c} \right] : \delta \mathbf{F}_M^c, \quad (2.41)$$

where the expression in square brackets is identified as the required tangent stiffness tensor ${}^4\mathbf{C}_M^\sigma$. In the derivation of (2.41) it has been used that in case of prescribed displacements of the RVE boundary (2.3) or of periodic boundary conditions (2.5), the initial and current volumes of an RVE are related according to $J_M = \det(\mathbf{F}_M) = V/V_0$.

2.5 Nested solution scheme

Based on the above developments the actual implementation of the first-order computational homogenization strategy may be described by the following subsequent steps.

The macroscopic structure to be analyzed is discretized by finite elements. The external load is applied by an incremental procedure. Increments can be associated with discrete time steps. The solution of the macroscopic non-linear system of equations is performed in a standard iterative manner. To each macroscopic integration point a discretized periodic RVE is assigned. The geometry of the RVE is based on the microstructural morphology of the material under consideration.

For each macroscopic integration point the local macroscopic deformation gradient tensor \mathbf{F}_M is computed from the iterative macroscopic nodal displacements (during the initialization step, zero deformation is assumed throughout the macroscopic structure, i.e. $\mathbf{F}_M = \mathbf{I}$, which allows to obtain the initial macroscopic constitutive tangent). The macroscopic deformation gradient tensor is used to formulate the boundary conditions to be applied on the corresponding representative cell. In the present implementation the periodic boundary conditions according to (2.7)-(2.9) are used.

The solution of the RVE boundary value problem (outlined in section 2.3) employing a fine scale finite element procedure, provides the resulting stress and strain distributions in the microstructural cell. Using the resulting forces at the prescribed nodes, the RVE averaged first Piola-Kirchhoff stress tensor \mathbf{P}_M is computed according to (2.19) and returned to the macroscopic integration point as a local macroscopic stress. From the global RVE stiffness matrix the local macroscopic consistent tangent ${}^4\mathbf{C}_M^P$ is obtained according to (2.39).

When the analysis of all microstructural RVEs is finished, the stress tensor is available at every macroscopic integration point. Thus, the internal macroscopic forces can be calculated. If these forces are in balance with the external load, incremental convergence has been achieved and the next time increment can be evaluated. If there is no convergence, the procedure is continued to achieve an updated estimation of the macroscopic nodal displacements. The macroscopic stiffness matrix is assembled using the constitutive tangents available at every macroscopic integration point from the RVE analysis. The solution of the macroscopic system of equations leads to an updated estimation of the macroscopic displacement field. The solution scheme is summarized in Table 2.1. It is remarked that the two-level scheme outlined above can be used selectively depending on the macroscopic deformation, e.g. in the elastic domain the macroscopic constitutive tangents do not have to be updated at every macroscopic loading step.

2.6 Computational example

In order to evaluate the presented computational homogenization approach, pure bending of a rectangular strip under plane strain conditions has been examined. Both the length and the height of the sample equal 0.2 m, the thickness is taken 1 m. The macromesh is composed of 5 quadrilateral 8 node plane strain reduced integration elements. The undeformed and deformed geometries of the macromesh are schematically depicted in Figure 2.5. At the left side the strip is fixed in axial (horizontal) direction, the displacement in transverse (vertical) direction is left free. At the right side the rota-

Table 2.1: Incremental-iterative nested multi-scale solution scheme for the first-order computational homogenization.

MACRO		MICRO
1. Initialization ▷ initialize the macroscopic model ▷ assign an RVE to every integration point ▷ loop over all integration points set $\mathbf{F}_M = \mathbf{I}$ store the tangent ▷ end integration point loop	$\xrightarrow{\mathbf{F}_M}$ $\xleftarrow{\text{tangent}}$	Initialization RVE analysis ▷ prescribe boundary conditions ▷ assemble the RVE stiffness ▷ calculate the tangent ${}^4\mathbf{C}_M^P$
2. Next increment ▷ apply increment of the macro load		
3. Next iteration ▷ assemble the macroscopic tangent stiffness ▷ solve the macroscopic system ▷ loop over all integration points calculate \mathbf{F}_M store \mathbf{P}_M store the tangent ▷ end integration point loop ▷ assemble the macroscopic internal forces	$\xrightarrow{\mathbf{F}_M}$ $\xleftarrow{\mathbf{P}_M}$ $\xleftarrow{\text{tangent}}$	RVE analysis ▷ prescribe boundary conditions ▷ assemble the RVE stiffness ▷ solve the RVE problem ▷ calculate \mathbf{P}_M ▷ calculate the tangent ${}^4\mathbf{C}_M^P$
4. Check for convergence ▷ if not converged \Rightarrow step 3 ▷ else \Rightarrow step 2		

tion of the cross section is prescribed. As pure bending is considered the behaviour of the strip is uniform in axial direction and, therefore, a single layer of elements on the macrolevel suffices to simulate the situation.

In this example two heterogeneous microstructures consisting of a homogeneous matrix material with initially 12% and 30% volume fractions of voids are studied. To generate a random distribution of cavities in the matrix with a prescribed volume fraction, maximum diameter of holes and minimum distance between two neighbouring holes, for a two-dimensional RVE, the procedure from Hall (1991) and Smit (1998) has been adopted. The microstructural cells used in the calculations are presented in Figure 2.6. It is worth mentioning that the absolute size of the microstructure is irrelevant for the first-order computational homogenization analysis (see also discussion in section 2.8).

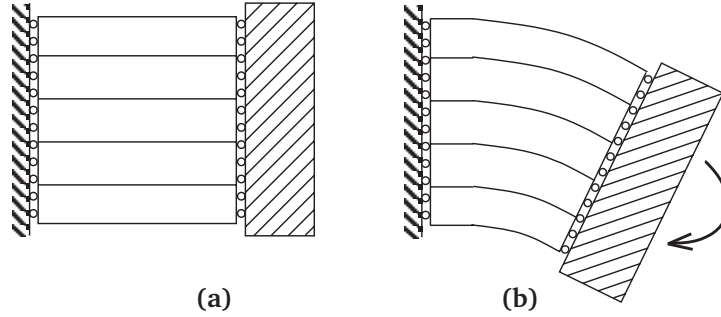


Figure 2.5: Schematic representation of the undeformed (a) and deformed (b) configurations of the macroscopically bended specimen.

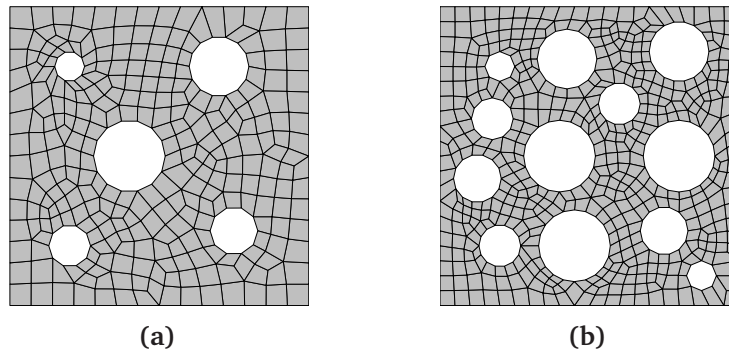


Figure 2.6: Microstructural cells used in the calculations with 12% voids (a) and 30% voids (b).

The matrix material behaviour has been described by a modified elasto-visco-plastic Bodner-Partom model. This choice is motivated by the intention to demonstrate that the method is well-suited for complex microstructural material behaviour, e.g. non-linear history and strain rate dependent at large strains. A brief summary of this model may be found in appendix A.3. In the present calculations the material parameters for annealed aluminum AA 1050 determined by van der Aa et al. (2000) have been used; elastic parameters: shear modulus $G = 2.6 \times 10^4$ MPa, bulk modulus $K = 7.8 \times 10^4$ MPa and viscosity parameters: $\Gamma_0 = 10^8 \text{ s}^{-2}$, $m = 13.8$, $n = 3.4$, $Z_0 = 81.4$ MPa, $Z_1 = 170$ MPa.

Micro-macro calculations for the heterogeneous structure, represented by the RVEs shown in Figure 2.6 have been carried out, simulating pure bending at a prescribed moment rate equal to $5 \times 10^5 \text{ N m s}^{-1}$. Figure 2.7 shows the distribution plots of the effective plastic strain for the case of the RVE with 12% volume fraction voids at an applied moment equal to $6.8 \times 10^5 \text{ N m}$ in the deformed macrostructure and in three deformed, initially identical RVEs at different locations in the macrostructure. Each hole acts as a plastic strain concentrator and causes higher strains in the RVE than those occurring in the homogenized macrostructure. In the present calculations the maximum effective plastic strain in the macrostructure is about 25%, whereas at RVE level this strain reaches 50%. It is obvious from the deformed geometry of the holes in Figure 2.7 that the RVE in the upper part of the bended strip is subjected to tension and the RVE in the lower part to compression, while the RVE in the vicinity of the neutral axis is loaded considerably milder than the other RVEs. This confirms the conclusion that the method realistically describes the deformation modes of the microstructure.

In Figure 2.8 the moment-curvature (curvature defined for the bottom edge of the

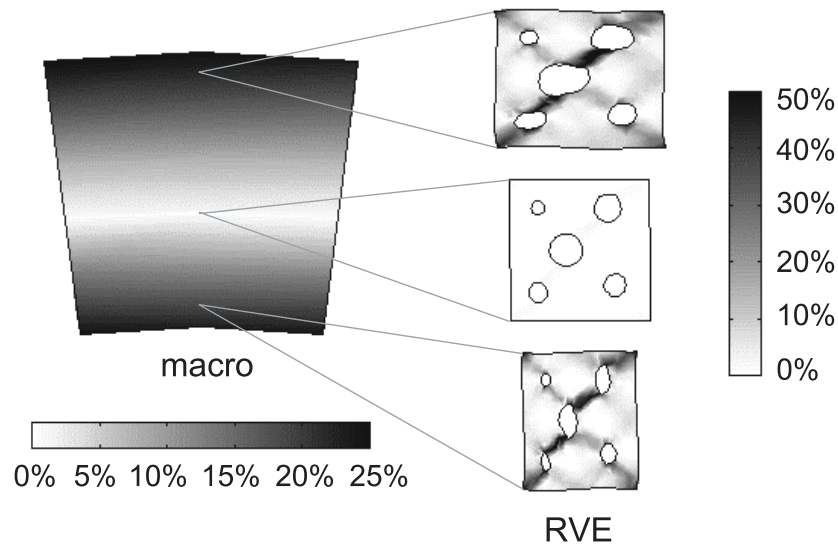


Figure 2.7: Distribution of the effective plastic strain in the deformed macrostructure and in three deformed RVEs, corresponding to different points of the macrostructure.

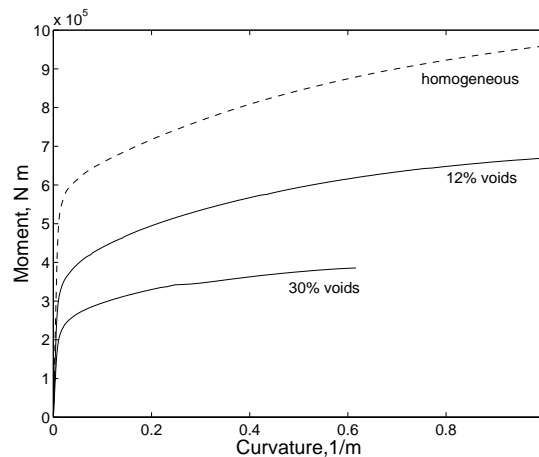


Figure 2.8: Moment-curvature diagram resulting from the first-order computational homogenization analysis.

specimen) diagram resulting from the computational homogenization approach is presented. To give an impression of the influence of the holes also the response of a homogeneous configuration (without cavities) is shown. It can be concluded that even the presence of 12% voids induces a reduction of the bending moment (at a certain curvature) of more than 25% in the plastic regime. This significant reduction in the bending moment may be attributed to the formation of microstructural shear bands, which are clearly observed in Figure 2.7. This indicates that in order to capture such an effect a detailed microstructural analysis is required. A straightforward application of, for example, the rule of mixtures would lead to erroneous results.

2.7 Concept of a representative volume element

2.7.1 General concept

The computational homogenization approach, as well as most of other homogenization techniques, are based on the concept of a representative volume element (RVE). An RVE is a model of a material microstructure to be used to obtain the response of the corresponding homogenized macroscopic continuum in a macroscopic material point. Thus, the proper choice of the RVE largely determines the accuracy of the modelling of a heterogeneous material.

There appear to be two significantly different ways to define a representative volume element (Drugan and Willis (1996)). The first definition requires an RVE to be a statistically representative sample of the microstructure, i.e. to include virtually a sampling of all possible microstructural configurations that occur in the composite. Clearly, in the case of a non-regular and non-uniform microstructure such a definition leads to a considerably large RVE. Therefore, RVEs that rigorously satisfy this definition are rarely used in actual homogenization analyses. This concept is usually employed when a computer model of the microstructure is being constructed based on experimentally obtained statistical information (e.g. Shan and Gokhale (2002)).

Another definition characterizes an RVE as the smallest microstructural volume that sufficiently accurately represents the overall macroscopic properties of interest. This usually leads to much smaller RVE sizes than the statistical definition described above. However, in this case the minimum required RVE size also depends on the type of material behaviour (e.g. for elastic behaviour usually much smaller RVEs suffice than for plastic behaviour), macroscopic loading path and difference of properties between heterogeneities. Moreover, the minimum RVE size, that results in a good approximation of the overall material properties, does not always lead to adequate distributions of the microfields within the RVE. This may be important if, for example, microstructural damage initiation or evolving microstructures are of interest.

The latter definition of an RVE is closely related to the one established by Hill (1963), who argued that an RVE is well-defined if it reflects the material microstructure and if the responses under uniform displacement and traction boundary conditions coincide. If a microstructural cell does not contain sufficient microstructural information, its overall responses under uniform displacement and traction boundary conditions will differ. The homogenized properties determined in this way are called “apparent”, a notion introduced by Huet (1990). The apparent properties obtained by application of uniform displacement boundary conditions on a microstructural cell usually overestimate the real effective properties, while the uniform traction boundary conditions lead to underestimation. As has been verified by a number of authors (van der Sluis et al. (2000); Terada et al. (2000)), for a given microstructural cell size, the periodic boundary conditions provide a better estimation of the overall properties, than the uniform displacement and uniform traction boundary conditions. This conclusion also holds if the microstructure does not really possess geometrical periodicity (Terada et al. (2000)). Increasing the size of the microstructural cell leads to a better estimation of the overall properties, and, finally, to a “convergence” of the results obtained with the different boundary conditions to the real effective properties of the composite material, as illustrated in Figure 2.9. The convergence of the apparent properties towards the effective ones at increasing size of the microstructural cell has been investigated by Huet (1990, 1999);

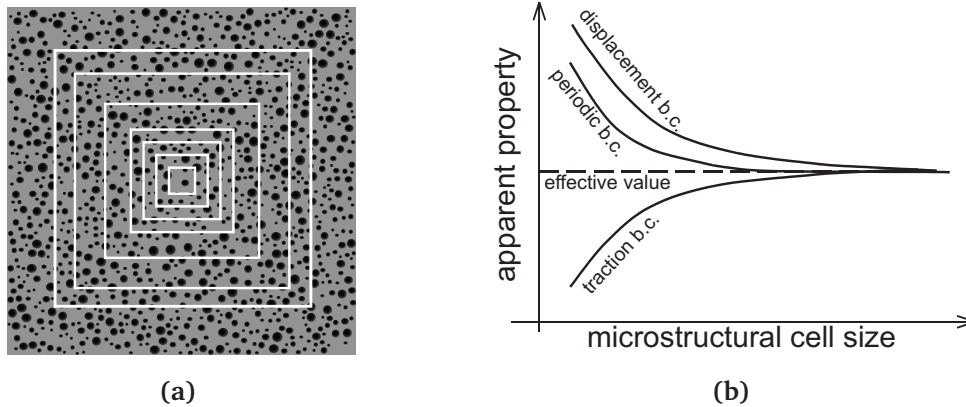


Figure 2.9: (a) Several microstructural cells of different sizes. (b) Convergence of the apparent properties to the effective values with increasing microstructural cell size for different types of boundary conditions.

Ostoja-Starzewski (1998, 1999); Pecullan et al. (1999); Terada et al. (2000).

2.7.2 Regular versus random representation

In practice, instead of a representative volume element, a unit cell is often used as a microstructural model, since it requires substantially less computational effort. This section examines the possible error, which is made in the obtained overall response of a multi-phase material, if the analysis is performed on a unit cell instead of an RVE.

As the simplest unit cell, a piece (for example a square or cube) of the matrix material containing a single heterogeneity (e.g. inclusion or void) could be suggested. The use of such a unit cell implicitly assumes a regular arrangement of the heterogeneities in the matrix, which contradicts the observations that almost all materials have a non-periodic or even spatially random microstructural composition. Examples are precipitates in metal alloys arranged randomly by their nature and artificial fiber reinforced composites, possessing a non-regular distribution of the fibers due to the production process. At the same time, several experimental evidences exist showing that the spatial variability in the microstructure significantly influences the overall behaviour and particularly the fracture characteristics of composites, as reported by Mackay (1990); Barsoum et al. (1992).

Different authors, e.g. Brockenbrough et al. (1991); Nakamura and Suresh (1993); Ghosh et al. (1996); Moulinec and Suquet (1998), have performed a comparison of the overall composite responses resulting from the modelling of regular and random structures. They have found a significant response difference in the plastic regime, while there is almost no deviation in elastic regime. Also it has been shown by Smit et al. (1999), that softening behaviour of a regularly composed structure may change to hardening in the case of a random composition. Most of these considerations, except for the latter, have been performed for small deformations, very simple elasto-plastic behaviour and relatively stiff inclusions (fibers). In this section the overall behaviour of regular and random structures is compared at large deformations, non-linear history dependent material behaviour, for voided material (an appropriate approximation for material with soft inclusions). Apart from the calculations on the microstructural cell (tensile configuration), also a full multi-scale analysis (pure bending) of both regular

and random structures is presented.

A material with a 12% volume fraction of voids is considered. The regularly stacked structure is modelled by a square unit cell containing a single hole (Figure 2.10a). For the modelling of a random structure 10 different unit cells with non-regular arrangements of voids with a distribution of void sizes have been generated (Figure 2.10b). The averaged behaviour of these 10 unit cells is expected to be representative for the real random structure with a given volume fraction of heterogeneities. Using several small non-regular unit cells instead of one larger RVE also allows to estimate the amount of deviation of the apparent properties obtained by the unit cell modelling, from the effective values for different types of material models and loading histories.

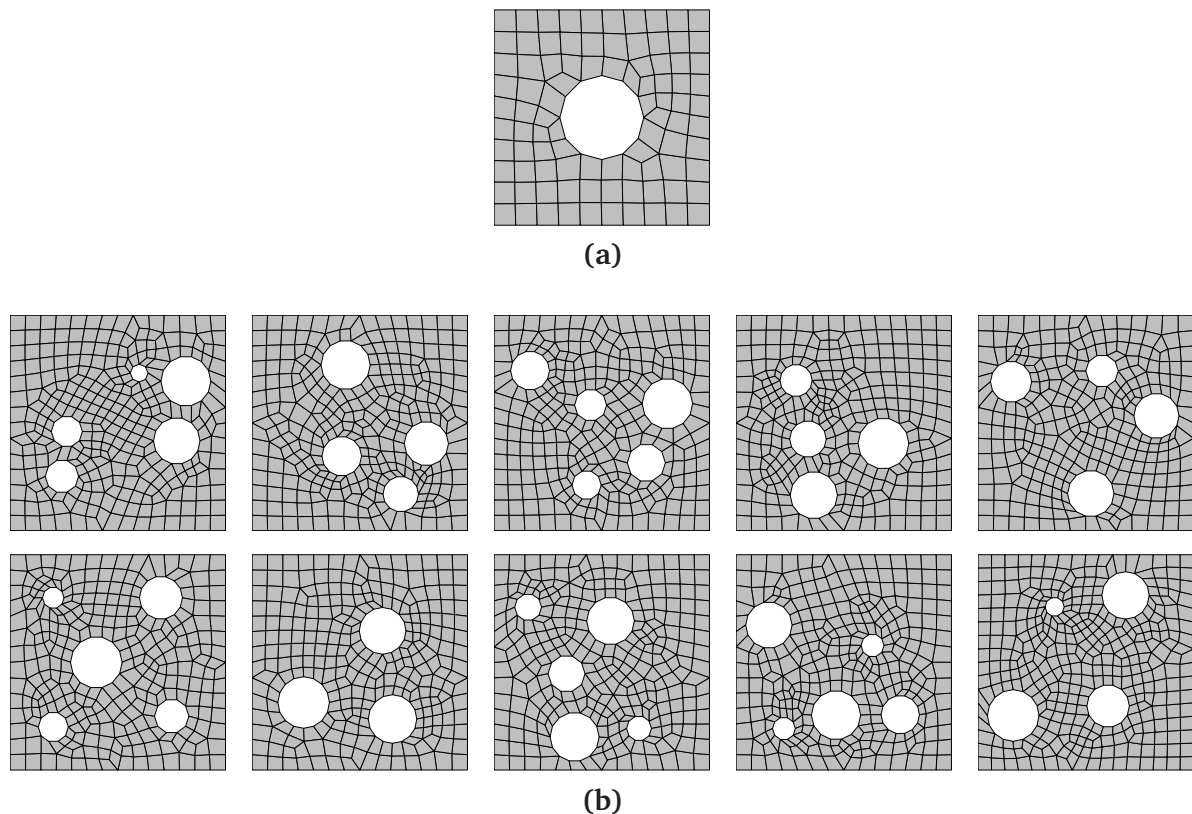


Figure 2.10: Unit cell with one hole (a), representing a regular structure, and 10 randomly composed unit cells (b).

In the subsequent sections a comparison is performed for three different constitutive models of the matrix material: hyper-elastic, elasto-visco-plastic with hardening and elasto-visco-plastic with intrinsic softening. First uniaxial extension (under plane strain conditions) of a macroscopic sample is considered. Because in this case the macroscopic deformation field is homogeneous a full micro-macro modelling is not necessary and an analysis of an isolated unit cell with adequate boundary conditions (periodic) suffices. In the last section the results of a micro-macro simulation of bending using random and regular microstructures are compared.

Elastic behaviour, tension

First a comparison of the overall behaviour of regular and random structures is carried out for the case of hyper-elastic behaviour of the matrix material, modelled as a compressible Neo-Hookean material as defined in appendix A.1. The material parameters used in the calculations are $K = 2667$ MPa, $G = 889$ MPa.

Figure 2.11 shows the stress-strain curves for the unit cells with regular and random void stacking. For small deformations there is almost no difference in the responses originating from the regular and random void distributions. This result is in agreement with the experiences reported in the literature for small deformations, see, e.g. Brockenbrough et al. (1991); Nakamura and Suresh (1993); Moulinec and Suquet (1998). For large deformations the stiffer behaviour of the regular structure becomes a little bit more pronounced, however, the deviations remain small. The difference between the response of the regular structure and the response averaged over the random unit cells does not exceed 2%. This small deviation is explained by Figure 2.12, presenting the distribution of the equivalent von Mises stress in the regular unit cell and in a random unit cell for 20% macroscopic strain. The stress field around any hole of the random structure is almost the same as around the hole of the regular structure, which indicates little interaction between voids. If only the averaged elastic constants are of interest, it is concluded that calculations performed on the simplest regular unit cell usually provide an answer within an acceptable tolerance.

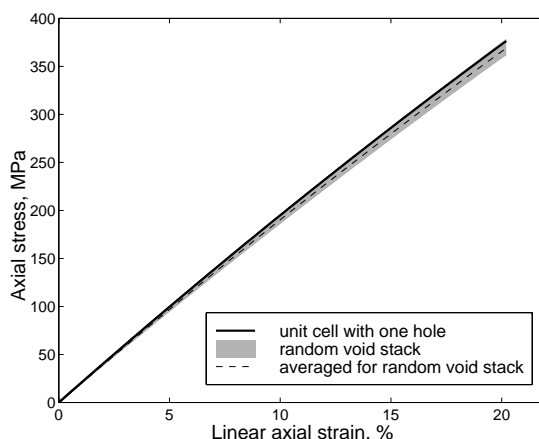


Figure 2.11: Tensile stress-strain responses (unit cell averages) of the regular and random structures in a voided hyper-elastic matrix material.

Elasto-visco-plastic behaviour with hardening, tension

The influence of the randomness of the microstructure on the macroscopic response becomes more significant when plastic yielding of one or more constituents occurs. This section investigates the responses of the regular and random unit cells under tensile loading when the matrix material exhibits elasto-visco-plastic behaviour with hardening. The constitutive description is given by the Bodner-Partom model specified in appendix A.3. The material parameters are the same as those used in section 2.6. The unit cells are subjected to uniaxial tension at a constant strain rate of 0.5 s^{-1} .

In Figure 2.13 the stress-strain curves are presented. In this case the difference between the overall response of the regular structure and the averaged response of the

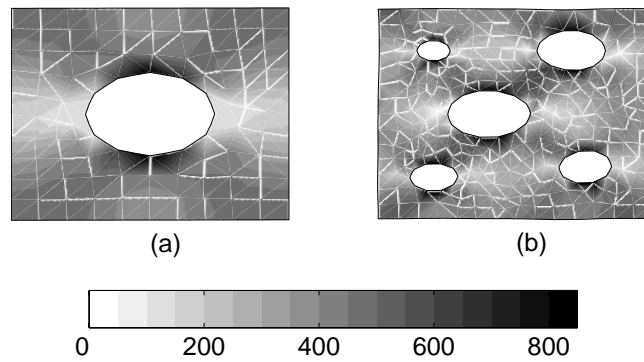


Figure 2.12: Distribution of the equivalent von Mises stress (MPa) in the deformed regular (a) and random (b) structures in a voided hyper-elastic matrix material.

random structures reaches 10%. The rather large scattering in the responses of different random cells is due to the small number of voids included. As has been demonstrated by Smit (1998), the scattering is significantly reduced if microstructural cells contain more heterogeneities. The averaged response is, however, hardly affected, provided that a sufficient number of random realizations has been considered.

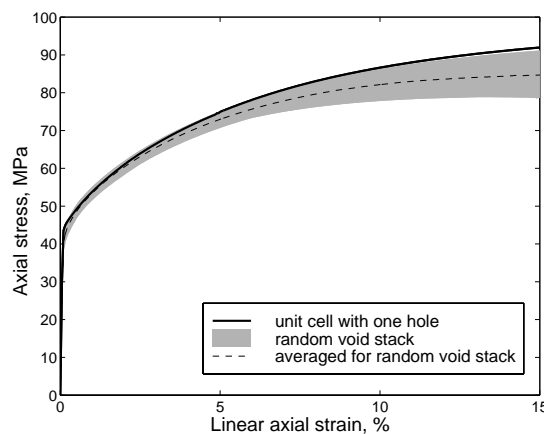


Figure 2.13: Tensile stress-strain responses (unit cell averages) of the regular and random structures for an elasto-visco-plastic matrix material with hardening.

The fundamental mechanism that governs the difference between the response of the regular structure and the averaged response of the random structures is illustrated in Figure 2.14, where the distribution of the effective plastic strain in the deformed regular and random unit cells at 15% applied macroscopic strain is presented. In the regular unit cell the ligaments yield simultaneously rather than sequentially with increasing macroscopic strain, which is the case for the random unit cell. As a result, at the same value of the macroscopic strain the regular unit cell is deformed relatively smoothly, while some ligaments in the random unit cell have already accumulated a significant amount of plastic strain. Consequently, the regular unit cell (in fact a structure with a periodic stacking of heterogeneities) has a larger overall stiffness than a random configuration.

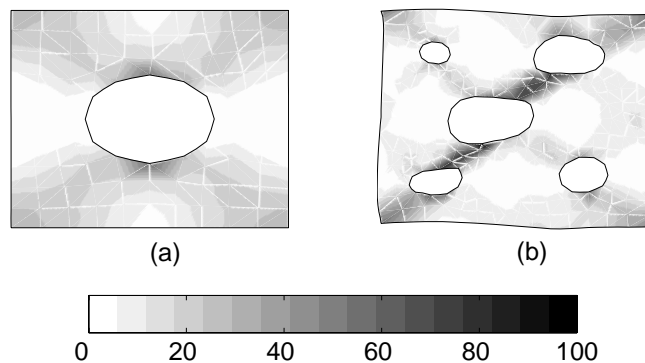


Figure 2.14: Distribution of the effective plastic strain in the deformed regular (a) and random (b) structures for an elasto-visco-plastic matrix material with hardening.

Elasto-visco-plastic behaviour with softening, tension

The difference in yielding mechanisms for regular and random microstructures outlined in the previous section causes not only a quantitative deviation in the responses of these structures (as illustrated by Figure 2.13), but in some cases also the qualitative character changes, as has been shown by Smit et al. (1999). For example, such a phenomenon can be observed when the matrix material is described by a generalized compressible Leonov model with intrinsic softening and subsequent hardening. The model is designed for the plastic deformation of polymers and incorporates a stress dependent Eyring viscosity extended by pressure dependence and intrinsic softening effects. Details of this model can be found in Baaijens (1991); Tervoort (1996); Govaert et al. (2000).

The resulting stress-strain curves for uniaxial tension of polycarbonate at a constant strain rate of 0.01 s^{-1} are given in Figure 2.15. The overall behaviour of the regular structure in the plastic regime exhibits some initial softening followed by hardening. The response of the regular structure is, in fact, similar to the response of one single ligament, that softens according to the intrinsic material behaviour. A completely different response can be observed for the random configurations. Although some of the random unit cells also demonstrate some softening behaviour, originating from the relatively simple composition of the unit cells used in the calculations, the average response of the random unit cells does not show any softening but exhibits continuous hardening. This is caused by the sequential appearance of elastic, softening and hardening zones within the random microstructure.

This example illustrates that the overall response of heterogeneous materials, when determined from a modelling by a regular structure, should be interpreted with great care, particularly in the case of complex material behaviour (e.g. in case of softening followed by hardening or vice versa).

Elasto-visco-plastic behaviour with hardening, bending

The comparison of the overall behaviour of the regular and random microstructures performed above has been based on the averaged behaviour of a single unit cell subjected to a particular loading history (uniaxial tension). The question remains how the randomness of the microstructure does influence the overall behaviour when a macro-

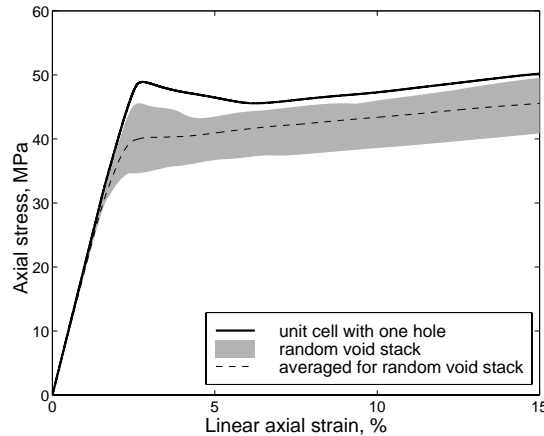


Figure 2.15: Tensile stress-strain responses (RVE averages) of the regular and random structures for an elasto-visco-plastic matrix material with intrinsic softening and subsequent hardening.

scopic sample is deformed heterogeneously, so that potentially every material point of the sample is subjected to a different loading history. In order to investigate this item the computational homogenization approach is a helpful tool.

As an example the influence of the spatial composition of the microstructure on the overall moment-curvature response of the voided material under pure bending is studied. The behaviour of the matrix material is described by the Bodner-Partom elasto-visco-plastic model with hardening. The macrogeometry and the material parameters are the same as these used in section 2.6.

Figure 2.16 shows the moment-curvature diagram resulting from the full micro-macro analysis of pure bending of the material using the regular and the random microstructures. Again, the regular structure exhibits a stiffer response than the averaged random result, while the maximum deviation is only about 5%, which is considerably less than for the tensile test with the same material behaviour (Figure 2.13). This smaller deviation originates from the fact that in case of bending all the unit cells assigned to the various macroscopic points over the height of the bended strip are loaded differently, see Figure 2.7. The unit cell at the top of the bended strip experiences tension, so that the observations dealt with in the previous examples apply. At the same time, there are also unit cells that are stretched less or still are in elastic regime, like for example the one in the vicinity of the neutral line, so that in average for the whole bending process the influence of randomness can be expected to be smaller than for uniaxial extension.

2.8 Discussion

In this chapter the first-order computational homogenization strategy, which provides an approach to determine the macroscopic response of heterogeneous materials with accurate account for microstructural characteristics and evolution of the morphology, has been presented. When using this micro-macro strategy there is no necessity to specify the homogenized macroscopic constitutive behaviour, which in case of large deformations and complex microstructures, would be generally a hardly feasible task. Instead, the constitutive behaviour at macroscopic integration points is determined by

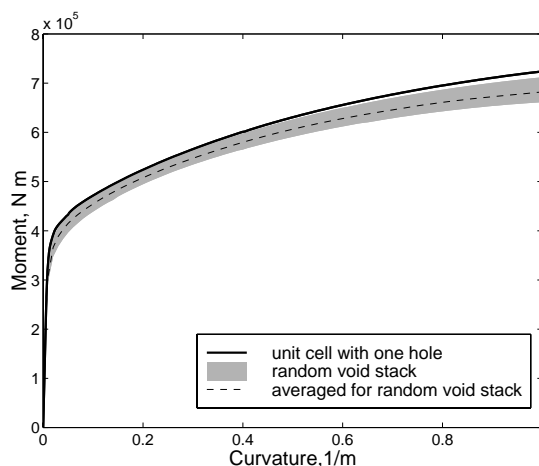


Figure 2.16: Moment-curvature responses of the regular and random structures for an elasto-visco-plastic matrix material with hardening.

averaging the results of a detailed modelling of the microstructure. This enables the straightforward application of the method to geometrically and physically non-linear problems, thus being a particularly valuable tool for the modelling of evolving highly non-linear heterogeneous microstructures under complex macroscopic loading paths.

Despite a number of attractive characteristics, there are a few strong limitations of the first-order computational homogenization framework. The shortcomings of the first-order scheme originate from the fundamental implicit assumption (also accepted in most other classical homogenization approaches) that the microstructural length scale is negligible in comparison with the macrostructural characteristic length (determined by the size of the macroscopic specimen or the wave length of the macroscopic load). Based on the concept of separation of scales it is justified to assume macroscopic uniformity of the deformation field over the microstructural cell. As a result, only simple first-order deformation modes (tension, compression, shear or combinations thereof) of the microstructure are found. As can be noticed for example in Figure 2.7, the typical bending mode, which from a physical point of view should appear for small, but finite, microstructural cells in the macroscopically bended specimen, is not found. Moreover, the dimensions of the microstructural heterogeneities do not influence the averaging procedure. Increasing the scale of the entire microstructure then leads to identical results. All of this is not surprising, since the first-order approach is fully in line with the standard continuum mechanics theory, where one of the fundamental points of departure is the principle of local action. In fact this principle states that material points are local, i.e. are identified with an infinitesimal volume only. This infinitesimal character is exactly represented in the behaviour of the microstructural RVEs, which are considered as macroscopic material points. This implies that the size of the microstructure is considered as irrelevant and hence microstructural and geometrical size effects are not taken into account. Furthermore, the assumption on uniformity of the macroscopic deformation over a representative microstructural cell is not valid in zones of large gradients of the deformation field, thus it is questionable whether macrostructural localization phenomena can be modelled within the first-order framework. The limitations of the first-order homogenization framework motivate the development of the second-order homogenization approach, which is presented in the next chapter.

Chapter 3

Second-order computational homogenization

This chapter presents the second-order computational homogenization framework, as an extension of the classical first-order computational homogenization framework, which aims at a modelling of macroscopic localization and microstructural size effects. In the second-order homogenization approach the macroscopic deformation gradient tensor and its gradient are imposed on a microstructural representative volume element. Every microstructural constituent is modelled as a classical continuum. On the macrolevel, however, a full second gradient equilibrium problem appears. From the solution of the underlying microstructural boundary value problem, the macroscopic stress tensor and the higher-order stress tensor are derived based on an extension of the Hill-Mandel condition. This automatically delivers the microstructurally based constitutive response of the second gradient macrocontinuum. In this chapter the theoretical development of the second-order computational homogenization scheme is presented and some issues of its implementation are discussed.

3.1 Introduction

In the previous chapter the first-order computational homogenization technique has been presented. The first-order micro-macro modelling framework, based on classical homogenization approaches, has been proven to be a versatile tool to establish micro-macro structure-property relations in materials, especially in those cases that the collective behaviour of a multi-phase heterogeneous material cannot be predicted by any other method, e.g. for a geometrically and physically non-linear material behaviour, complex loading paths or evolving microstructures. However, as has been pointed out at the end of the previous chapter, two major disadvantages of the existing (first-order) micro-macro computational approaches (as well as the conventional homogenization methods), which significantly limit their applicability, can be mentioned. In spite of the fact that these techniques do account for the volume fraction, distribution and morphol-

ogy of the constituents, they do not incorporate the absolute size of the microstructure, thus making it impossible to address geometrical size effects. (Microstructural size effects, which are triggered through small-scale deformation mechanisms, and which can be captured in a local stress-strain response, do not fall into this category.) Another difficulty arises from the intrinsic assumption of uniformity of the macroscopic (stress or strain) fields attributed to each microstructural representative cell. This uniformity assumption relies on the concept of separation of scales and is not appropriate in critical regions of high deformation gradients, where the macroscopic fields can vary considerably.

To solve the problems mentioned, different authors proposed to use generalized continua (e.g. Cosserat, couple-stress, strain-gradient, non-local) to describe the behaviour of either the microstructural constituents or the homogenized macrostructure, or to employ generalized continuum models at both levels simultaneously. This has the effect of introducing a material length scale into the constitutive description, providing a natural way to obtain a dependence of the overall response of composites on the absolute size of the constituents and to achieve a realistic description of a microstructurally initiated macroscopic localization.

Bounds and estimates of the effective properties of two-phase composites with a linear couple-stress constitutive law for each phase have been obtained by Smyshlyaev and Fleck (1994). Later these results were applied to bound the overall non-linear behaviour of the composites with a plastic strain-gradient constitutive model for the phases (Smyshlyaev and Fleck (1995)) and of a polycrystalline aggregate of single crystals with a strain-gradient constitutive law for each slip system (Smyshlyaev and Fleck (1996)). Drugan and Willis (1996) developed a non-local effective constitutive equation for a class of linearly elastic composites by formally solving the equilibrium equation in terms of stress polarization and subsequent ensemble averaging. For periodic, linearly elastic media an asymptotic solution technique has been used to obtain the homogenized higher-order gradient material behaviour, for which effective moduli up to an arbitrary order may be determined based on the properties and morphology of the phases (Boutin (1996); Triantafyllidis and Bardenhagen (1996)). Smyshlyaev and Cherednichenko (2000) have combined the asymptotic method with a variational technique, which allowed them to minimize the difference between the real and homogenized behaviour and to ensure that the higher-order homogenized equations remain elliptic. This approach has been extended to the full three-dimensional case and was used to numerically obtain (by solving a set of microstructural boundary value problems) the effective higher-order moduli of a fiber-reinforced composite by Peerlings and Fleck (2001).

Recently, some work has been done to extend the unit cell based homogenization approaches to higher-order continuum models. Zhu et al. (1997) used strain-gradients in the expression for the flow stress of the matrix material to obtain particle size dependent overall flow properties of metal matrix composites. Forest and Sab (1998) proposed a methodology to derive an effective Cosserat continuum for a heterogeneous material, every constituent of which was described by a classical continuum model. They presented a scheme that consists of a representation of the macroscopic displacement field by a polynomial basis field with a periodic perturbation. Within a similar framework, van der Sluis et al. (1999b) presented the homogenization of an elasto-visco-plastic heterogeneous material on the microlevel towards a Cosserat elastic con-

tinuum on the macrolevel. Ostoja-Starzewski et al. (1999) and Bouyge et al. (2001) used the unit cell modelling with different types of boundary conditions to calculate the overall moduli and the characteristic length of a homogenized couple-stress medium, composed of classical linearly elastic constituents. De Felice and Rizzi (1997) and Yuan and Tomita (2001) extended the classical homogenization scheme of Suquet (1985) based on the Hill-Mandel macrohomogeneity condition to the Cosserat continuum. Forest et al. (1999) obtained the effective properties of a heterogeneous linearly elastic Cosserat material, by also considering the microstructural constituents as linearly elastic Cosserat media. In Forest et al. (2001), the asymptotic homogenization method, classically used for periodic heterogeneous materials, has been applied to linearly elastic Cosserat microstructural constituents. It was shown that depending on the ratio of the microstructural intrinsic Cosserat length and the macrostructural size, the homogenized material should be treated either as a classical (Cauchy) continuum with volume couples or as a Cosserat medium. These developments have been used by Forest et al. (2000) to model the behaviour of a polycrystalline material consisting of elasto-viscoplastic Cosserat single crystals.

The above works were limited to geometrically linear kinematics in the framework of the Cosserat and the couple-stress theories and were mostly concerned with obtaining the homogenized material parameters for certain cases rather than providing a general computational homogenization procedure. To the knowledge of the author, the second-order computational homogenization framework, dealt with in the present chapter, is the first attempt to develop a systematic procedure to obtain the constitutive response of a second gradient continuum, based on the behaviour of the underlying microstructure.

In this chapter a second-order computational procedure, that extends the classical computational homogenization technique to a full-gradient geometrically non-linear approach, is developed (Kouznetsova et al. (2002)). The procedure, leading to a higher-order macroscopic continuum model, uses the macroscopic deformation tensor and its gradient to prescribe the essential boundary conditions on a microstructural representative volume element (RVE). For the RVE boundary conditions, the well-known periodic boundary conditions are generalized. In this framework all microstructural constituents are treated as a classical continuum, described by standard first-order equilibrium and constitutive equations. The reason for this is that for geometrically and physically non-linear material behaviour, the formulation of constitutive equations and experimental procedures for material parameter identification are sufficiently developed and verified for single phases considered as a classical continuum; for the higher-order models, these are still to be developed. Therefore, in this theory, the microstructural boundary value problem remains classical, so that its solution is readily obtained without any complications. From the solution of the RVE boundary value problem, the macroscopic stress tensor and a higher-order stress tensor are extracted employing an enhanced Hill-Mandel condition. This automatically delivers the microstructurally based constitutive response of the higher-order macrocontinuum, which deals with the microstructural size in a natural way. The higher-order macroscopic constitutive response, which poses a difficult problem in closed-form homogenization techniques, is thus found in a straightforward manner without any additional assumptions.

This chapter is organized as follows. First in section 3.2 the general framework of the second-order computational homogenization is presented. Then section 3.3 discusses the micro-macro kinematics, which leads to the formulation of the boundary conditions

to be imposed on a microstructural representative cell. The relations for the determination of the macroscopic stress tensor and the higher-order stress tensor are elaborated in section 3.4. Some aspects of the implementation of the second-order computational homogenization scheme in a finite element framework are discussed in section 3.5. Special attention is given to the extraction of the macroscopic constitutive tangents from the microstructural stiffness. Finally, the solution scheme for the coupled second-order micro-macro computational analysis is outlined in section 3.6.

3.2 General framework

Let the non-linear deformation map, describing the transformation from the undeformed macroscopic state (position vector \vec{X}) to the deformed state (\vec{x}) at time t , be defined as $\vec{x} = \vec{\phi}(\vec{X}, t)$. For an infinitesimal material line element, classical continuum mechanics leads to the linear mapping

$$d\vec{x} = \left(\frac{\partial \vec{\phi}}{\partial \vec{X}} \right)^c \cdot d\vec{X} = \mathbf{F}_M \cdot d\vec{X}, \quad (3.1)$$

where the deformation gradient tensor \mathbf{F}_M is given by

$$\mathbf{F}_M = \left(\frac{\partial \vec{\phi}}{\partial \vec{X}} \right)^c = (\nabla_{0M} \vec{x})^c. \quad (3.2)$$

As in chapter 2, the subscript ‘‘M’’ refers to a macroscopic quantity, while the subscript ‘‘m’’ will denote a microscopic quantity.

The linear relation (3.1) is used as the point of departure in the first-order computational homogenization, described in chapter 2. When dealing with line elements in volumes of a finite size, relation (3.1) does not apply any more, and an expression for a finite material vector $\Delta \vec{x}$ in the current macroscopic configuration may be obtained using a Taylor series expansion

$$\Delta \vec{x} = \mathbf{F}_M \cdot \Delta \vec{X} + \frac{1}{2} \Delta \vec{X} \cdot {}^3\mathbf{G}_M \cdot \Delta \vec{X} + \mathcal{O}(\Delta \vec{X}^3), \quad (3.3)$$

where the third-order tensor ${}^3\mathbf{G}_M$ is introduced as

$${}^3\mathbf{G}_M = \frac{\partial}{\partial \vec{X}} \left(\frac{\partial \vec{\phi}}{\partial \vec{X}} \right)^c = \nabla_{0M} \mathbf{F}_M. \quad (3.4)$$

Although $\Delta \vec{X}$ (and $\Delta \vec{x}$) is a finite vector, this vector is assumed to be sufficiently small, so that the terms, which contain deformation gradients higher than the second-order, may still be neglected, and the Taylor series expansion (3.3) can be truncated after the second term. The higher-order (in this case the second-order) computational homogenization approach uses both the macroscopic deformation tensor \mathbf{F}_M and its gradient ${}^3\mathbf{G}_M = \nabla_{0M} \mathbf{F}_M$ to prescribe kinematic boundary conditions on an RVE. A scheme of the gradient-enhanced computational homogenization is presented in Figure 3.1 (cf. Figure 2.3). In the general case that an RVE is subjected to a non-zero gradient of the deformation, the classical periodic boundary conditions cannot be applied and therefore a new type of ‘‘generalized’’ periodic boundary conditions will be introduced (see section 3.3). These boundary conditions complete the boundary value problem on the

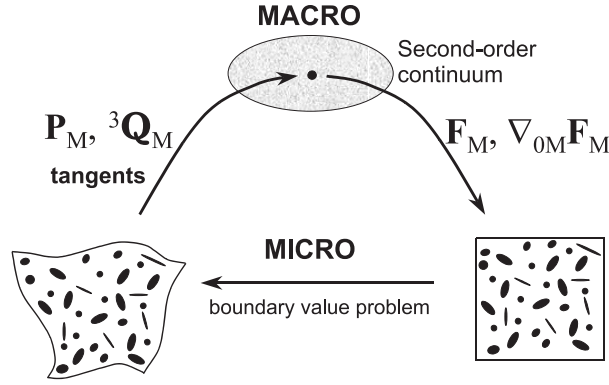


Figure 3.1: Second-order computational homogenization scheme.

RVE level, which is formulated as a standard problem of quasi-static equilibrium in a classical continuum. The equilibrium equation for the microstructural RVE (in the absence of body forces) takes the form

$$\nabla_{0m} \cdot \mathbf{P}_m^c = \vec{0}, \quad (3.5)$$

where \mathbf{P}_m is the first Piola-Kirchhoff stress tensor, related to the Cauchy stress tensor by $\mathbf{P}_m = \det(\mathbf{F}_m) \boldsymbol{\sigma}_m \cdot (\mathbf{F}_m^c)^{-1}$. The material behaviour of each microstructural constituent α (e.g. matrix, inclusion etc.) is described by its constitutive law, specifying a time and history dependent stress-strain relationship

$$\mathbf{P}_m^{(\alpha)}(t) = \mathcal{F}^{(\alpha)} \{ \mathbf{F}_m(\tau), \tau \in [0, t] \}. \quad (3.6)$$

It is emphasized that the present framework is not specifically designed for any particular constitutive law; the microstructural material behaviour may be very complex and include a physical and/or geometrical evolution of the microstructure, when modelled on the microstructural level. After the solution of the RVE boundary value problem, a macroscopic stress tensor (in the actual case the first Piola-Kirchhoff stress tensor \mathbf{P}_M) and a higher-order stress tensor ${}^3\mathbf{Q}_M$ (a third order tensor), defined as the work conjugate of the gradient ${}^3\mathbf{G}_M$ of the deformation gradient tensor, are derived exploiting the Hill-Mandel energy condition. Further details are discussed in section 3.4.

Contrary to the microstructural problem, which remains a classical one, macroscopically, a full gradient second-order equilibrium problem appears. The formulation and the associated finite element implementation are outlined in chapter 4. In contrast to most higher-order theories, the framework presented here does not bring in complicating factors in terms of an a priori quantification of the higher-order constitutive response. Macroscopic quantities are obtained from the microstructural analysis according to a straightforward multi-scale mathematical derivation.

3.3 Micro-macro kinematics

In order to construct a boundary value problem for a microstructural RVE the point of departure is the Taylor series expansion (3.3), truncated after the second-order term

$$\Delta \vec{x} = \mathbf{F}_M \cdot \Delta \vec{X} + \frac{1}{2} \Delta \vec{X} \cdot {}^3\mathbf{G}_M \cdot \Delta \vec{X} + \Delta \vec{w}. \quad (3.7)$$

The extra term $\Delta\vec{w}$ represents a microstructural fluctuation field, added here to account for the effect of a local microdisplacement field that is superimposed on the local macroscopic displacement field. From (3.7) the microscopic deformation tensor \mathbf{F}_m is determined as

$$\mathbf{F}_m = (\nabla_{0m}\Delta\vec{x})^c = \mathbf{F}_M + \Delta\vec{X} \cdot {}^3\mathbf{G}_M + (\nabla_{0m}\Delta\vec{w})^c, \quad (3.8)$$

where the minor symmetry $G_{Mijk} = G_{Mkji}$ of the tensor ${}^3\mathbf{G}_M$, following from its definition (3.4), has been used. Integrating (3.8) over the undeformed volume V_0 of the RVE and scaling by this volume leads to

$$\frac{1}{V_0} \int_{V_0} \mathbf{F}_m dV_0 = \mathbf{F}_M + \left(\frac{1}{V_0} \int_{V_0} \Delta\vec{X} dV_0 \right) \cdot {}^3\mathbf{G}_M + \frac{1}{V_0} \int_{V_0} (\nabla_{0m}\Delta\vec{w})^c dV_0. \quad (3.9)$$

Preserving one of the averaging theorems of the classical homogenization theory (see for example Suquet (1985) and section 2.4.1), the macroscopic deformation tensor \mathbf{F}_M is required to be equal to the volume average of the microstructural deformation tensor \mathbf{F}_m

$$\mathbf{F}_M = \frac{1}{V_0} \int_{V_0} \mathbf{F}_m dV_0. \quad (3.10)$$

Applying (3.10) to the kinematical relation given in equation (3.9) and choosing

$$\frac{1}{V_0} \int_{V_0} \Delta\vec{X} dV_0 = \vec{0}, \quad (3.11)$$

leads to the additional requirement

$$\frac{1}{V_0} \int_{V_0} (\nabla_{0m}\Delta\vec{w})^c dV_0 = \frac{1}{V_0} \int_{\Gamma_0} \Delta\vec{w} \vec{N} d\Gamma_0 = \mathbf{0}, \quad (3.12)$$

where the divergence theorem has been used to transform the volume integral to an integral over the undeformed boundary Γ_0 of the RVE, with outward normal \vec{N} .

Relation (3.11) is easily satisfied by placing the geometric center of the undeformed RVE at the origin of a Cartesian vector basis, i.e. $\vec{X}_c = \vec{0}$ (this always can be done without loss of generality) and writing equation (3.7) with respect to the center of the RVE. Hence $\Delta\vec{x} = \vec{x} - \vec{x}_c$ and $\Delta\vec{X} = \vec{X} - \vec{X}_c = \vec{X}$. From a physical point of view the center of the RVE is identified as the macroscopic point, at which the macroscopic deformation gradient tensor \mathbf{F}_M and its gradient ${}^3\mathbf{G}_M$ are calculated. The RVE volume represents the underlying microstructure in a finite vicinity of this point.

Constraint (3.12) necessitates complementary considerations. This equation may be satisfied in many alternative ways. In similarity with chapter 2, the following three approaches can be used

1. $\Delta\vec{w} = \vec{0}$, $\forall \vec{X} \in V_0$. This does not allow for any microstructural fluctuations and enforces the entire volume to deform precisely according to the prescribed \mathbf{F}_M and ${}^3\mathbf{G}_M$. For the first-order theory this is usually referred to as the Taylor (or Voigt) assumption.

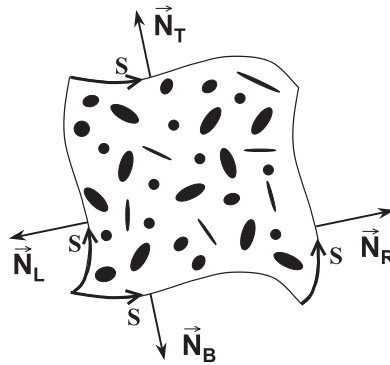


Figure 3.2: An initially periodic two-dimensional rectangular-shaped RVE.

2. $\Delta \vec{w} = \vec{0}, \forall \vec{X} \in \Gamma_0$. With this condition the displacement of the boundary of the RVE is fully prescribed, while leaving the microstructural fluctuations inside the volume yet undetermined. For the first-order case this is equivalent to uniform displacement boundary conditions.
3. Consider an initially periodic (two-dimensional) rectangular-shaped RVE, see Figure 3.2, so that for every two corresponding points on opposite boundaries $\vec{N}_L(s) = -\vec{N}_R(s)$ or $\vec{N}_B(s) = -\vec{N}_T(s)$, where the subscripts L, R, B and T denote quantities corresponding to the left, right, bottom and top boundary of the RVE, respectively, and s is a local coordinate along the edges. For this case (3.12) is satisfied if

$$\Delta \vec{w}_L(s) = \Delta \vec{w}_R(s) \quad \text{and} \quad \Delta \vec{w}_B(s) = \Delta \vec{w}_T(s), \quad (3.13)$$

which, in the first-order case, is equivalent to the frequently used periodic boundary conditions.

The same types of boundary conditions have been presented previously in the context of the first-order computational homogenization (see section 2.3) based on different arguments. The concept of a microstructural fluctuation field, however, seems to be rather general and allows the selection of other types of boundary conditions.

As has been mentioned in the previous chapter (section 2.7.1), use of periodic boundary conditions provides a better estimate of the overall properties than the uniformly prescribed displacement boundary conditions and the uniformly prescribed traction boundary conditions (van der Sluis et al. (2000); Terada et al. (2000)). Thus, the concept of a periodic fluctuation field according to (3.13) is also applied in the present approach. However, it is important to notice that in the second-order framework the macroscopic part of the deformation is definitely not periodic. In the general case of a non-zero gradient of the deformation gradient tensor, ${}^3\mathbf{G}_M \neq {}^3\mathbf{0}$, a non-periodic RVE shape will be found. Therefore, the notion of periodicity is employed here in a “generalized” sense, a concept that will be clarified in the following.

A two-dimensional initially rectangular RVE, schematically depicted in Figure 3.3, is considered, a choice which can easily be made without severe restrictions. However, without entering in details, the approach can also be extended to an initially periodic (but not necessarily rectangular) shape of the RVE and to three-dimensional configurations. In the undeformed reference state the RVE has boundary normals $\vec{N}_L = -\vec{N}_R$ and $\vec{N}_B = -\vec{N}_T$, width W and height H .

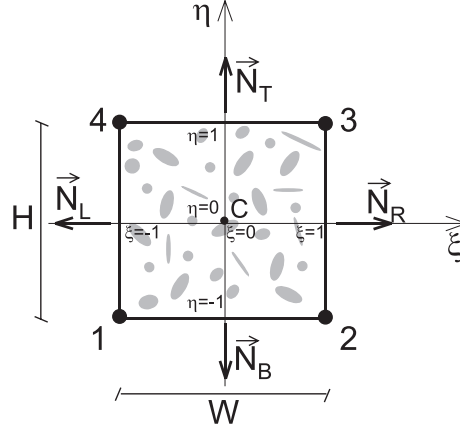


Figure 3.3: Schematic picture of an undeformed RVE for the second-order computational homogenization.

Applying (3.7) to the left and right boundary of the RVE and subtracting the results, with account for the periodicity conditions (3.13), eliminates the unknowns \vec{x}_c and $\Delta\vec{v}$. A kinematic constraint between the left and right boundary is recovered according to

$$\vec{x}_R = \vec{x}_L + \mathbf{A} \cdot \vec{X}_L + \vec{a}, \quad (3.14)$$

where the tensor \mathbf{A} and the vector \vec{a} are related to the macroscopic deformation quantities by

$$\mathbf{A} = W \vec{N}_R \cdot {}^3\mathbf{G}_M, \quad (3.15)$$

$$\vec{a} = W \mathbf{F}_M \cdot \vec{N}_R + \frac{W^2}{2} \vec{N}_R \cdot {}^3\mathbf{G}_M \cdot \vec{N}_R. \quad (3.16)$$

Similarly, for the bottom and top edge

$$\vec{x}_T = \vec{x}_B + \mathbf{B} \cdot \vec{X}_B + \vec{b}, \quad (3.17)$$

with

$$\mathbf{B} = H \vec{N}_T \cdot {}^3\mathbf{G}_M, \quad (3.18)$$

$$\vec{b} = H \mathbf{F}_M \cdot \vec{N}_T + \frac{H^2}{2} \vec{N}_T \cdot {}^3\mathbf{G}_M \cdot \vec{N}_T. \quad (3.19)$$

The equations (3.14) and (3.17) in fact reflect a linear relation between the deformed shapes of the opposite edges of the RVE, hereby deviating from the conventional periodic boundary conditions, where the shapes of opposite edges remain identical. Consequently, in contrast to the first-order case, the deformed RVE is no longer geometrically periodic. Furthermore, it is remarked that with ${}^3\mathbf{G} = {}^3\mathbf{0}$, the relations (3.14)–(3.19) lead to $\vec{x}_R = \vec{x}_L + \vec{x}_2 - \vec{x}_1$ and $\vec{x}_T = \vec{x}_B + \vec{x}_4 - \vec{x}_1$ (with \vec{x}_i denoting the current position vector of node i , Figure 3.3) in the deformed state, which are precisely the standard periodic boundary conditions on a two-dimensional periodic RVE (cf. equations (2.7) and (2.8)).

Note that the microstructural fluctuation vectors of the corner nodes $\Delta\vec{v}_i$, $i = \overline{1, 4}$ are constrained to be all identical in order to satisfy the periodicity conditions (3.13).

Considering that the fluctuation field on the RVE is in fact determined up to a constant value, expressing a rigid body displacement, which is generally suppressed, the fluctuation vectors of the corner nodes are set to zero, so that the displacements of the four corner nodes are fully prescribed

$$\Delta \vec{x}_i = \mathbf{F}_M \cdot \Delta \vec{X}_i + \frac{1}{2} \Delta \vec{X}_i \cdot {}^3\mathbf{G}_M \cdot \Delta \vec{X}_i, \quad i = \overline{1,4}. \quad (3.20)$$

By making use of the local coordinate system (ξ, η) defined in Figure 3.3, the constraints (3.14) and (3.17) can be elaborated yielding

$$\vec{x}_R = \vec{x}_L + W \mathbf{F}_M \cdot \vec{N}_R + \frac{WH}{2} \eta \vec{N}_R \cdot {}^3\mathbf{G}_M \cdot \vec{N}_T, \quad (3.21)$$

$$\vec{x}_T = \vec{x}_B + H \mathbf{F}_M \cdot \vec{N}_T + \frac{WH}{2} \xi \vec{N}_T \cdot {}^3\mathbf{G}_M \cdot \vec{N}_R. \quad (3.22)$$

Because of the minor symmetry of ${}^3\mathbf{G}_M$, $\vec{N}_T \cdot {}^3\mathbf{G}_M \cdot \vec{N}_R$ equals $\vec{N}_R \cdot {}^3\mathbf{G}_M \cdot \vec{N}_T$. This means that the kinematic equations (3.14)–(3.19) derived above in fact involve only two of the six (independent) components of ${}^3\mathbf{G}_M$ additional to the four components of \mathbf{F}_M (in 2D). Thus a modified set of boundary conditions is needed in order to subject the RVE to the full gradient ${}^3\mathbf{G}_M$. Moreover, it is remarked that the above relations are derived only by identifying the macroscopic deformation tensor \mathbf{F}_M with the volume average of its microstructural counterpart \mathbf{F}_m . Therefore the next step in constructing the kinematic framework for the higher-order RVE attempts to relate the macroscopic gradient of the deformation ${}^3\mathbf{G}_M$ to microstructural quantities.

To relate the macroscopic gradient of the deformation ${}^3\mathbf{G}_M = \nabla_{0M} \mathbf{F}_M$ to microstructural variables, first the microstructural gradient of the deformation gradient ${}^3\mathbf{G}_m = \nabla_{0m} \mathbf{F}_m$ is obtained from (3.8) and integrated over the initial RVE volume. This gives

$$\frac{1}{V_0} \int_{V_0} \nabla_{0m} \mathbf{F}_m \, dV_0 = {}^3\mathbf{G}_M + \frac{1}{V_0} \int_{V_0} \nabla_{0m} (\nabla_{0m} \Delta \vec{w})^c \, dV_0. \quad (3.23)$$

If equality of the macroscopic gradient of the deformation gradient ${}^3\mathbf{G}_M$ and the volume average of its microstructural counterpart ${}^3\mathbf{G}_m = \nabla_{0m} \mathbf{F}_m$ is enforced, the last term in (3.23) should be set to zero

$$\frac{1}{V_0} \int_{V_0} \nabla_{0m} (\nabla_{0m} \Delta \vec{w})^c \, dV_0 = \frac{1}{V_0} \int_{\Gamma_0} \vec{N} (\nabla_{0m} \Delta \vec{w})^c \, d\Gamma_0 = {}^3\mathbf{0}, \quad (3.24)$$

where the divergence theorem has been applied. The above relation provides an additional constraint on the fluctuation field along the RVE boundary.

Splitting the gradient $\nabla_{0m} \Delta \vec{w}$ into a normal gradient $\vec{N} D_{0m} \Delta \vec{w} \equiv \vec{N} \vec{N} \cdot \nabla_{0m} \Delta \vec{w}$ and a surface gradient $\nabla_{0m}^s \Delta \vec{w} \equiv (\mathbf{I} - \vec{N} \vec{N}) \cdot \nabla_{0m} \Delta \vec{w}$, leads to

$$\frac{1}{V_0} \int_{\Gamma_0} \vec{N} (\vec{N} D_{0m} \Delta \vec{w})^c \, d\Gamma_0 + \frac{1}{V_0} \int_{\Gamma_0} \vec{N} (\nabla_{0m}^s \Delta \vec{w})^c \, d\Gamma_0 = {}^3\mathbf{0}. \quad (3.25)$$

Using the requirement of periodicity of the microfluctuation field (3.13), for an initially rectangular RVE, the second integral in (3.25) is identically zero. An additional

constraint should prescribe the normal gradient of the fluctuation field in such a way that the first term in (3.25) is also zero. Therefore, higher-order boundary conditions would have to be prescribed on the RVE and consequently the microstructural formulation would also become of the higher-order type. This, however, is not consistent with the intention to preserve the microstructural RVE problem as a classical boundary value problem.

Hence, an alternative relation between the macroscopic gradient of the deformation gradient ${}^3\mathbf{G}_M$ and the microscopic variables, which does not lead to higher-order boundary conditions, is established in the present framework. For this purpose the following integral over the initial volume V_0 of the RVE is considered:

$$\int_{V_0} (\mathbf{F}_m^c \vec{X} + \vec{X} \mathbf{F}_m) dV_0. \quad (3.26)$$

The choice of this expression as a point of departure is motivated by its similarity to the relation between the macroscopic higher-order stress tensor ${}^3\mathbf{Q}_M$ and microscopic stress quantities, which will be presented in the next section (eq. (3.47)).

Elaboration of (3.26) by substitution of relation (3.8) for \mathbf{F}_m , with account for (3.11) (which is a particular choice locating the origin at the geometric center of the RVE, made in the present framework) leads to

$$\int_{V_0} (\mathbf{F}_m^c \vec{X} + \vec{X} \mathbf{F}_m) dV_0 = ({}^3\mathbf{G}_M \cdot \mathbf{J} + \mathbf{J} \cdot {}^3\mathbf{G}_M) + \int_{V_0} [(\nabla_{0m} \Delta \vec{w}) \vec{X} + \vec{X} (\nabla_{0m} \Delta \vec{w})^c] dV_0, \quad (3.27)$$

where the tensor \mathbf{J} , which may be interpreted as the geometrical inertia tensor with respect to the center of the RVE, is defined as

$$\mathbf{J} = \int_{V_0} \vec{X} \vec{X} dV_0. \quad (3.28)$$

In fact, equation (3.27) may be considered as a system of linear algebraic equations relating the components of tensor ${}^3\mathbf{G}_M$ to the microstructural quantities \mathbf{F}_m and $\Delta \vec{w}$. For the particular case of a square RVE, so that $H = W$, the geometric inertia tensor has the form $\mathbf{J} = (V_0 W^2 / 12) \mathbf{I}$ (with \mathbf{I} the second-order unit tensor) and tensor ${}^3\mathbf{G}_M$ may be explicitly formulated in terms of the volume averages of the microstructural quantities

$${}^3\mathbf{G}_M = \frac{6}{V_0 W^2} \left\{ \int_{V_0} (\mathbf{F}_m^c \vec{X} + \vec{X} \mathbf{F}_m) dV_0 - \int_{V_0} [(\nabla_{0m} \Delta \vec{w}) \vec{X} + \vec{X} (\nabla_{0m} \Delta \vec{w})^c] dV_0 \right\}. \quad (3.29)$$

Since the determination of the RVE behaviour should preferably be performed from a boundary value problem, it is desired to relate the macroscopic kinematic quantities to microscopic displacements defined only on the RVE boundary. Using the rule $(\nabla_{0m} \vec{a}) \vec{X} = \nabla_{0m} (\vec{a} \vec{X}) - (\mathbf{I} \vec{a})^{RC}$ for arbitrary \vec{a} , where instead of vector \vec{a} , either $\Delta \vec{x}$ or $\Delta \vec{w}$ is substituted (in this relation the superscript RC indicates right conjugation, which for a third-order tensor ${}^3\mathbf{T}$ is defined as $T_{ijk}^{RC} = T_{ikj}$), and applying the divergence

theorem allows the transformation of the volume integrals in (3.27)

$$\begin{aligned} {}^3\mathbf{G}_M \cdot \mathbf{J} + \mathbf{J} \cdot {}^3\mathbf{G}_M &= \int_{\Gamma_0} (\vec{N} \Delta \vec{x} \vec{X} + \vec{X} \Delta \vec{x} \vec{N}) d\Gamma_0 - 2 \left(\mathbf{I} \int_{V_0} \Delta \vec{x} dV_0 \right)^{RC} \\ &\quad - \int_{\Gamma_0} (\vec{N} \Delta \vec{w} \vec{X} + \vec{X} \Delta \vec{w} \vec{N}) d\Gamma_0 + 2 \left(\mathbf{I} \int_{V_0} \Delta \vec{w} dV_0 \right)^{RC}. \end{aligned} \quad (3.30)$$

Finally, by using (3.7) and (3.11) the components of the gradient of the deformation gradient tensor ${}^3\mathbf{G}_M$ are related to quantities defined on the RVE boundary only

$$\begin{aligned} {}^3\mathbf{G}_M \cdot \mathbf{J} + \mathbf{J} \cdot {}^3\mathbf{G}_M + (\mathbf{I} \mathbf{J} : {}^3\mathbf{G}_M^{RC})^{RC} &= \int_{\Gamma_0} (\vec{N} \Delta \vec{x} \vec{X} + \vec{X} \Delta \vec{x} \vec{N}) d\Gamma_0 \\ &\quad - \int_{\Gamma_0} (\vec{N} \Delta \vec{w} \vec{X} + \vec{X} \Delta \vec{w} \vec{N}) d\Gamma_0. \end{aligned} \quad (3.31)$$

For the case of a square RVE the above relation reduces to

$$\begin{aligned} {}^3\mathbf{G}_M + \frac{1}{2} (\mathbf{I} \mathbf{I} : {}^3\mathbf{G}_M^{RC})^{RC} &= \frac{6}{V_0 W^2} \left\{ \int_{\Gamma_0} (\vec{N} \Delta \vec{x} \vec{X} + \vec{X} \Delta \vec{x} \vec{N}) d\Gamma_0 \right. \\ &\quad \left. - \int_{\Gamma_0} (\vec{N} \Delta \vec{w} \vec{X} + \vec{X} \Delta \vec{w} \vec{N}) d\Gamma_0 \right\}. \end{aligned} \quad (3.32)$$

Since the above relations ((3.31) or (3.32)) are required to be independent of any particular realization of the fluctuation field, the new additional constraint takes the form

$$\int_{\Gamma_0} (\vec{N} \Delta \vec{w} \vec{X} + \vec{X} \Delta \vec{w} \vec{N}) d\Gamma_0 = {}^3\mathbf{0}. \quad (3.33)$$

Exploiting this constraint enables the RVE problem to be considered as an ordinary boundary value problem. For the initially rectangular RVE in Figure 3.3 with account for the periodicity conditions (3.13), the constraint (3.33) reduces to two constraints along two contiguous boundaries

$$\int_{\Gamma_{0L}} \Delta \vec{w}_L d\Gamma_0 = \vec{0} \quad \text{and} \quad \int_{\Gamma_{0B}} \Delta \vec{w}_B d\Gamma_0 = \vec{0}. \quad (3.34)$$

Comparable constraints are then automatically satisfied on the remaining opposite boundaries through the periodicity constraint (3.13). From (3.34) it is obvious that these new constraints enforce the shape of the boundary to approximate the kinematically fully prescribed boundary in an average sense. In terms of the position vectors of the boundary points in the deformed state the constraints (3.34) have the form

$$\int_{\Gamma_{0L}} \Delta \vec{x}_L d\Gamma_0 = \mathbf{F}_M \cdot \int_{\Gamma_{0L}} \vec{X}_L d\Gamma_0 + \frac{1}{2} {}^3\mathbf{G}_M^{RC} : \int_{\Gamma_{0L}} \vec{X}_L \vec{X}_L d\Gamma_0, \quad (3.35)$$

$$\int_{\Gamma_{0B}} \Delta \vec{x}_B d\Gamma_0 = \mathbf{F}_M \cdot \int_{\Gamma_{0B}} \vec{X}_B d\Gamma_0 + \frac{1}{2} {}^3\mathbf{G}_M^{RC} : \int_{\Gamma_{0B}} \vec{X}_B \vec{X}_B d\Gamma_0. \quad (3.36)$$

To summarize, the RVE boundary value problem to be solved consists of the equilibrium equation (3.5), the constitutive laws (3.6) and boundary conditions which fully prescribe the displacements of the four RVE corner nodes and require the periodicity of the microfluctuation field on opposite boundaries (3.13) and zero averaged fluctuations along two adjoint boundaries (3.34).

3.4 Stress and higher-order stress

In order to determine RVE averaged stress measures, an extension of the Hill-Mandel energy condition (also referred to as the macrohomogeneity condition, Hill (1963); Suquet (1985), see also section 2.4.3) is used. This condition requires the microscopic volume average of the variation of work performed on an RVE to equal the local variation of the work on the macroscale. Taking into account that on the macrolevel the modelling deals with a full gradient higher-order continuum (definition of the local work for this case is given in the next chapter, eq. (4.3), see also Fleck and Hutchinson (1997)), the extended Hill-Mandel condition takes the form (compare to (2.22))

$$\frac{1}{V_0} \int_{V_0} \mathbf{P}_m : \delta \mathbf{F}_m^c dV_0 = \mathbf{P}_M : \delta \mathbf{F}_M^c + {}^3\mathbf{Q}_M : \delta {}^3\mathbf{G}_M, \quad \forall \delta \Delta \vec{x}. \quad (3.37)$$

It is remarked that (3.37) is in fact the definition of the macroscopic stress tensor \mathbf{P}_M and the macroscopic higher-order stress tensor ${}^3\mathbf{Q}_M$.

Using the divergence theorem, with incorporation of equilibrium in the microstructure (3.5), the microstructural work (per unit of volume in the reference state) can be written as

$$\delta W_{0M} = \frac{1}{V_0} \int_{V_0} \mathbf{P}_m : \delta \mathbf{F}_m^c dV_0 = \frac{1}{V_0} \int_{\Gamma_0} \vec{p} \cdot \delta \Delta \vec{x} d\Gamma_0, \quad (3.38)$$

where $\vec{p} = \vec{N} \cdot \mathbf{P}_m^c$ represents the first Piola-Kirchhoff stress vector.

Substituting the variation of the position vector $\delta \Delta \vec{x}$ according to (3.7)

$$\delta \Delta \vec{x} = \delta \mathbf{F}_M \cdot \vec{X} + \frac{1}{2} \vec{X} \cdot \delta {}^3\mathbf{G}_M \cdot \vec{X} + \delta \Delta \vec{w}, \quad (3.39)$$

into equation (3.38) leads to

$$\delta W_{0M} = \frac{1}{V_0} \int_{\Gamma_0} \vec{p} \vec{X} d\Gamma_0 : \delta \mathbf{F}_M^c + \frac{1}{2V_0} \int_{\Gamma_0} \vec{X} \vec{p} \vec{X} d\Gamma_0 : \delta {}^3\mathbf{G}_M + \frac{1}{V_0} \int_{\Gamma_0} \vec{p} \cdot \delta \Delta \vec{w} d\Gamma_0. \quad (3.40)$$

Since the homogeneous constraints (3.13) do not contribute to the total work and accounting for (3.34) and for the zero microstructural fluctuation field value in the corner nodes $\Delta \vec{w}_i = \vec{0}$, $i = \overline{1,4}$, the last term in (3.40) can be proven to disappear

$$\int_{\Gamma_0} \vec{p} \cdot \delta \Delta \vec{w} d\Gamma_0 = 0, \quad (3.41)$$

manifesting the fact that the microstructural fluctuation field does not affect the average variation of the microscopic work.

Comparing (3.40) (with account for (3.41)) and the right-hand side of (3.37) the relations for the macroscopic first Piola-Kirchhoff stress tensor \mathbf{P}_M and the macroscopic higher-order stress tensor ${}^3\mathbf{Q}_M$ are obtained as

$$\mathbf{P}_M = \frac{1}{V_0} \int_{\Gamma_0} \vec{p} \vec{X} \, d\Gamma_0, \quad (3.42)$$

$${}^3\mathbf{Q}_M = \frac{1}{2V_0} \int_{\Gamma_0} \vec{X} \vec{p} \vec{X} \, d\Gamma_0. \quad (3.43)$$

The above formulas relate the macroscopic stress tensor and the macroscopic higher-order stress tensor to microstructural variables defined on the RVE boundary. The relations (3.42) and (3.43) can also be transformed into volume integrals, allowing the macroscopic stress measures to be expressed in terms of volume averages of microstructural quantities. The macroscopic stress tensor \mathbf{P}_M again equals the volume average of the microscopic stress tensor \mathbf{P}_m

$$\mathbf{P}_M = \frac{1}{V_0} \int_{V_0} \mathbf{P}_m \, dV_0. \quad (3.44)$$

The proof of this equation is identical to that for the first-order framework (for the derivation see (2.15)-(2.17)).

The derivation for the higher-order stress tensor ${}^3\mathbf{Q}_M$ follows the same procedure. Applying the divergence theorem to transform the boundary integral in (3.43) to a volume integral gives

$$\begin{aligned} {}^3\mathbf{Q}_M &= \frac{1}{2V_0} \int_{\Gamma_0} \vec{X} \vec{p} \vec{X} \, d\Gamma_0 = \frac{1}{2V_0} \int_{\Gamma_0} ((\vec{N} \cdot \mathbf{P}_m^c) \vec{X} \vec{X})^{LC} \, d\Gamma_0 \\ &= \frac{1}{2V_0} \int_{V_0} (\nabla_{0m} \cdot (\mathbf{P}_m^c \vec{X} \vec{X}))^{LC} \, dV_0, \end{aligned} \quad (3.45)$$

where the superscript LC denotes left conjugation, $T_{ijk}^{LC} = T_{jik}$. Finally using the equality

$$\begin{aligned} \nabla_{0m} \cdot (\mathbf{P}_m^c \vec{X} \vec{X}) &= (\nabla_{0m} \cdot \mathbf{P}_m^c) \vec{X} \vec{X} + \mathbf{P}_m \cdot (\nabla_{0m} \vec{X}) \vec{X} + (\vec{X} \mathbf{P}_m \cdot (\nabla_{0m} \vec{X}))^{LC} \\ &= \mathbf{P}_m \vec{X} + (\vec{X} \mathbf{P}_m)^{LC}, \end{aligned} \quad (3.46)$$

where equilibrium has been exploited, the relation between the macroscopic higher-order stress tensor and microstructural quantities is obtained

$${}^3\mathbf{Q}_M = \frac{1}{2V_0} \int_{V_0} (\mathbf{P}_m^c \vec{X} + \vec{X} \mathbf{P}_m) \, dV_0. \quad (3.47)$$

It is clear from (3.47) that ${}^3\mathbf{Q}_M$ can be interpreted as the first moment (with respect to the RVE center) of the microscopic first Piola-Kirchhoff stress tensor \mathbf{P}_m over the initial RVE volume V_0 .

3.5 Finite element implementation

3.5.1 RVE boundary value problem

In the framework of the second-order computational homogenization the RVE boundary value problem to be solved consists of the equilibrium equation (3.5), the constitutive laws for the microstructural constituents (3.6) and boundary conditions that include prescribed positions of the four corner nodes (3.20), kinematic constraints between opposite boundaries reflecting periodic microstructural fluctuations (3.14) and (3.17) and kinematic constraints prescribing zero-averaged fluctuations along two adjoint boundaries (3.35) and (3.36). Such a problem is a standard non-linear quasi-static boundary value problem for a classical continuum. For the solution of this problem any available suitable solution strategy and associated numerical technique may be used. As it was the case in the previous section, the attention will be focused on a two-dimensional rectangular RVE, schematically depicted in Figure 3.3.

Following the standard finite element procedure for the microlevel RVE, the weak form of equilibrium (after discretization) leads to a system of non-linear algebraic equations in the nodal displacements \underline{u}

$$\underline{f}_{int}(\underline{u}) = \underline{f}_{ext}, \quad (3.48)$$

expressing the balance of internal and external nodal forces. This system has to be completed by boundary conditions. Hence, the earlier introduced boundary conditions (3.20), (3.14), (3.17) and (3.35), (3.36) have to be elaborated in more detail.

First, the unknown position of the center of the RVE in the deformed state \vec{x}_c ($\Delta\vec{x}_i = \vec{x}_i - \vec{x}_c$, $i = \overline{1,4}$) has to be eliminated from (3.20). This is easily achieved by spatial fixation of displacement of one of the corner nodes, say $i = 1$, (thereby suppressing rigid body translation of the RVE). Taking into account that $\vec{X}_c = \vec{0}$, \vec{x}_c is obtained as

$$\vec{x}_c = \vec{X}_1 - \mathbf{F}_M \cdot \vec{X}_1 - \frac{1}{2} \vec{X}_1 \cdot {}^3\mathbf{G}_M \cdot \vec{X}_1. \quad (3.49)$$

Then the displacements of the corner nodes can be written as

$$\begin{aligned} \vec{u}_j &= (\mathbf{F}_M - \mathbf{I}) \cdot (\vec{X}_j - \vec{X}_1) + \frac{1}{2} {}^3\mathbf{G}_M^{RC} : (\vec{X}_j \vec{X}_j - \vec{X}_1 \vec{X}_1), \quad j = 2, 3, 4 \\ \vec{u}_1 &= \vec{0}. \end{aligned} \quad (3.50)$$

For a given macroscopic deformation gradient tensor \mathbf{F}_M and its gradient ${}^3\mathbf{G}_M$ and a specified geometry of the RVE, the displacements of the corner nodes are readily calculated and added to the system (3.48).

For the initially rectangular RVE depicted in Figure 3.3, the constraints (3.14) and (3.17), reflecting a linear relation between opposite edges, can be recast in terms of displacements as

$$\vec{u}_R = \vec{u}_L + \frac{1}{2}(1 - \eta)(\vec{u}_2 - \vec{u}_1) + \frac{1}{2}(1 + \eta)(\vec{u}_3 - \vec{u}_4), \quad (3.51)$$

$$\vec{u}_T = \vec{u}_B + \frac{1}{2}(1 - \xi)(\vec{u}_4 - \vec{u}_1) + \frac{1}{2}(1 + \xi)(\vec{u}_3 - \vec{u}_2), \quad (3.52)$$

with η and ξ the local coordinates of the corresponding points on the right-left and top-bottom boundaries, respectively, see Figure 3.3. The vectors \vec{u}_i , $i = \overline{1,4}$ are, as before, displacements of the four corner nodes expressed in \mathbf{F}_M and ${}^3\mathbf{G}_M$ by (3.50). For the following it is supposed, as in section 2.4.4, that the finite element discretization is

performed such that the distribution of nodes on opposite RVE edges is equal. In a discretized format the relations (3.51) and (3.52) then easily lead to a set of homogeneous constraints of the type

$$\underline{C}_a \underline{u}_a = \underline{0}, \quad (3.53)$$

with \underline{C}_a a matrix containing coefficients in the constraint relations and \underline{u}_a a column with the degrees of freedom involved in the constraints.

Boundary constraints prescribing the zero-averaged microstructural fluctuations (3.35) and (3.36) may be rewritten in terms of displacement vectors of the nodes on the boundary

$$\sum_{i=1}^{N_L} \alpha^i \vec{u}_L^i = \vec{u}_{L^*}(\mathbf{F}_M, {}^3\mathbf{G}_M), \quad \sum_{i=1}^{N_B} \beta^i \vec{u}_B^i = \vec{u}_{B^*}(\mathbf{F}_M, {}^3\mathbf{G}_M), \quad (3.54)$$

where N_L and N_B are the numbers of nodes on the left and bottom boundary, respectively; α^i and β^i are coefficients following from the discretized form of the integrals in the left-hand sides of (3.35) and (3.36); \vec{u}_{L^*} and \vec{u}_{B^*} are vectors from the right-hand sides of (3.35) and (3.36) with account for (3.49)

$$\vec{u}_{L^*} = (\mathbf{F}_M - \mathbf{I}) \cdot \int_{\Gamma_{0L}} (\vec{X}_L - \vec{X}_1) d\Gamma_0 + \frac{1}{2} {}^3\mathbf{G}_M^{RC} : \int_{\Gamma_{0L}} (\vec{X}_L \vec{X}_L - \vec{X}_1 \vec{X}_1) d\Gamma_0, \quad (3.55)$$

$$\vec{u}_{B^*} = (\mathbf{F}_M - \mathbf{I}) \cdot \int_{\Gamma_{0B}} (\vec{X}_B - \vec{X}_1) d\Gamma_0 + \frac{1}{2} {}^3\mathbf{G}_M^{RC} : \int_{\Gamma_{0B}} (\vec{X}_B \vec{X}_B - \vec{X}_1 \vec{X}_1) d\Gamma_0. \quad (3.56)$$

Consequently, the vectors \vec{u}_{L^*} and \vec{u}_{B^*} are known for any given \mathbf{F}_M and ${}^3\mathbf{G}_M$ and the RVE geometry. Contrary to the constraints (3.51) and (3.52), which gave rise to the homogeneous tying relations (3.53), the constraints (3.54) result in a set of non-homogeneous constraints of the type

$$\underline{C}_b \underline{u}_b = \underline{q}_b. \quad (3.57)$$

Procedures for imposing the constraints (3.53) and (3.57) include the direct elimination of the dependent degrees of freedom from the system of equations, or the use of Lagrange multipliers or penalty functions. In the following, the constraints (3.53) and (3.57) are enforced by elimination of the dependent degrees of freedom. Although such a procedure may be found in many textbooks on finite elements (e.g. Cook et al. (1989)), here it is summarized for the sake of completeness but also in the context of the derivation of the macroscopic tangent stiffness, which will be presented in the next section.

First, the constraints (3.53) and (3.57) are combined into

$$\underline{C} \underline{u} = \underline{q}, \quad (3.58)$$

where the column \underline{q} has non-zero values only at the positions corresponding to the non-homogeneous constraints (3.57). In the following derivations no distinction is made between constraints with zero and with non-zero values in \underline{q} and the right-hand side

column \underline{q} is treated as a column containing given values. Next, (3.58) is partitioned according to

$$[\underline{C}_i \quad \underline{C}_d] \begin{bmatrix} \underline{u}_i \\ \underline{u}_d \end{bmatrix} = \underline{q}, \quad (3.59)$$

where \underline{u}_i are the independent degrees of freedom (to be retained in the system) and \underline{u}_d are the dependent degrees of freedom (to be eliminated from the system). Because there are as many degrees of freedom \underline{u}_d as there are independent constraint equations in (3.59), matrix \underline{C}_d is square and non-singular. Solution for \underline{u}_d yields

$$\underline{u}_d = [\underline{C}_{di} \quad \underline{C}_d^{-1}] \begin{bmatrix} \underline{u}_i \\ \underline{q} \end{bmatrix}, \quad \text{with} \quad \underline{C}_{di} = -\underline{C}_d^{-1} \underline{C}_i. \quad (3.60)$$

This relation may be further rewritten as

$$\begin{bmatrix} \underline{u}_i \\ \underline{u}_d \end{bmatrix} = \underline{T} \begin{bmatrix} \underline{u}_i \\ \underline{q} \end{bmatrix}, \quad \text{with} \quad \underline{T} = \begin{bmatrix} \underline{I} & \underline{O} \\ \underline{C}_{di} & \underline{C}_d^{-1} \end{bmatrix}, \quad (3.61)$$

where \underline{I} is a unit matrix of size $[N_i \times N_i]$ and \underline{O} is a zero matrix of size $[N_i \times N_d]$, with N_i and N_d the number of the independent and dependent degrees of freedom, respectively.

With the transformation matrix \underline{T} defined such that $\underline{d} = \underline{T} \underline{d}'$, the common transformations $\underline{r}' = \underline{T}^T \underline{r}$ and $\underline{K}' = \underline{T}^T \underline{K} \underline{T}$ can be applied to a linear system of equations of the form $\underline{K} \underline{d} = \underline{r}$, leading to a new system $\underline{K}' \underline{d}' = \underline{r}'$.

The standard linearization of the non-linear system of equations (3.48) leads to a linear system in the iterative corrections $\delta \underline{u}$ to the current estimate \underline{u} . This system may be partitioned as

$$\begin{bmatrix} \underline{K}_{ii} & \underline{K}_{id} \\ \underline{K}_{di} & \underline{K}_{dd} \end{bmatrix} \begin{bmatrix} \delta \underline{u}_i \\ \delta \underline{u}_d \end{bmatrix} = \begin{bmatrix} \delta \underline{r}_i \\ \delta \underline{r}_d \end{bmatrix}, \quad (3.62)$$

with the residual nodal forces at the right-hand side. Noting that all the constraint equations considered above are linear, and thus their linearization is straightforward, application of the transformation (3.61) to the system (3.62) gives

$$\begin{bmatrix} \underline{K}_{ii} + \underline{K}_{id} \underline{C}_{di} + \underline{C}_{di}^T \underline{K}_{di} + \underline{C}_{di}^T \underline{K}_{dd} \underline{C}_{di} & (\underline{K}_{id} + \underline{C}_{di}^T \underline{K}_{dd}) \underline{C}_d^{-1} \\ (\underline{C}_d^{-1})^T (\underline{K}_{di} + \underline{K}_{dd} \underline{C}_{di}) & \underline{C}_d^{-1} \underline{K}_{dd} \underline{C}_d^{-1} \end{bmatrix} \begin{bmatrix} \delta \underline{u}_i \\ \delta \underline{q} \end{bmatrix} = \begin{bmatrix} \delta \underline{r}_i + \underline{C}_{di}^T \delta \underline{r}_d \\ (\underline{C}_d^{-1})^T \delta \underline{r}_d \end{bmatrix}. \quad (3.63)$$

3.5.2 Calculation of the macroscopic stress and higher-order stress

After the analysis of a microstructural RVE is completed, the RVE averaged stress tensors have to be extracted. Of course, the macroscopic stress and higher-order stress tensors can be calculated by numerically evaluating the volume integrals (3.44) and (3.47) or the surface integrals (3.42) and (3.43). However, for the particular implementation proposed here, computationally more efficient formulas may be obtained.

As it was the case for the first-order computational homogenization scheme, it may be verified that all the forces involved in the homogeneous kinematic constraints (3.51) and (3.52) cancel out from the surface integrals (3.42) and (3.43). The major difference

with respect to the first-order case is the presence of the additional non-homogeneous constraint relations (3.54). The forces involved in this constraint have to be properly accounted for. After somewhat lengthy but straightforward mathematical manipulations the surface integrals (3.42) and (3.43) can be transformed to

$$\mathbf{P}_M = \frac{1}{V_0} \left\{ \sum_{i=1}^4 \vec{f}_i \vec{X}_i + \vec{f}_{L^*} \int_{\Gamma_{0L}} \vec{X}_L d\Gamma_0 + \vec{f}_{B^*} \int_{\Gamma_{0B}} \vec{X}_B d\Gamma_0 \right\}, \quad (3.64)$$

$${}^3\mathbf{Q}_M = \frac{1}{2V_0} \left\{ \sum_{i=1}^4 \vec{X}_i \vec{f}_i \vec{X}_i + \left(\vec{f}_{L^*} \int_{\Gamma_{0L}} \vec{X}_L \vec{X}_L d\Gamma_0 \right)^{LC} + \left(\vec{f}_{B^*} \int_{\Gamma_{0B}} \vec{X}_B \vec{X}_B d\Gamma_0 \right)^{LC} \right\}, \quad (3.65)$$

where \vec{f}_i , $i = \overline{1,4}$ are the external forces in the four prescribed corner nodes; \vec{f}_{L^*} and \vec{f}_{B^*} are the resultant forces necessary to enforce the non-homogeneous constraints (3.54). If a Lagrange multiplier technique would have been used to impose the constraints (3.54), the forces \vec{f}_{L^*} and \vec{f}_{B^*} might be identified as the Lagrange multipliers. If elimination of the dependent degrees of freedom, as has been outlined in the previous section, is used, these forces are extracted from the column in the right-hand side of (3.63). In a finite element program the forces \vec{f}_i , $i = \overline{1,4}$ and \vec{f}_{L^*} and \vec{f}_{B^*} are readily available for the converged solution, from which the macroscopic stress tensor \mathbf{P}_M and the higher-order stress tensor ${}^3\mathbf{Q}_M$ can be easily calculated using the formulas (3.64) and (3.65).

3.5.3 Macroscopic constitutive tangents

For the finite element solution of the macroscopic problem a stiffness matrix at every macroscopic integration point is required. Similar as in the first-order computational homogenization scheme, in the second-order homogenization two alternative approaches can be used to obtain the macroscopic stiffness, i.e. numerical differentiation based on a perturbation technique and condensation of the total RVE stiffness matrix. For reasons of efficiency, in the present work the latter method is used.

The derivation of the macroscopic consistent tangent operator for the second-order computational homogenization largely follows the same steps as for the first-order case (see section 2.4.4). In the first-order case information on the macroscopic deformation (components of the macroscopic deformation gradient tensor \mathbf{F}_M) are transmitted to the RVE level through the displacements of three prescribed nodes. In the second-order approach in addition to the macroscopic deformation tensor \mathbf{F}_M , also its gradient ${}^3\mathbf{G}_M$ is imposed on the RVE. This is done by prescribing the displacement of the four corner nodes of the RVE (\vec{u}_i , $i = \overline{1,4}$) and the vectors \vec{u}_{L^*} and \vec{u}_{B^*} in the right-hand side of the non-homogeneous constraints (3.54). Components of the vectors \vec{u}_{L^*} and \vec{u}_{B^*} enter the system of equations (3.63) through the column denoted by \underline{q} (see section 3.5.1).

In order to obtain the macroscopic stiffness matrix, the system of equations (3.63) is written as $\underline{K}^* \delta \underline{u} = \delta \underline{f}^*$ and rearranged to the form

$$\begin{bmatrix} \underline{K}_{pp}^* & \underline{K}_{pf}^* \\ \underline{K}_{fp}^* & \underline{K}_{ff}^* \end{bmatrix} \begin{bmatrix} \delta \underline{u}_p \\ \delta \underline{u}_f \end{bmatrix} = \begin{bmatrix} \delta \underline{f}_p^* \\ \delta \underline{f}_f^* \end{bmatrix} \approx \begin{bmatrix} \delta \underline{f}_p^* \\ \underline{0} \end{bmatrix}, \quad (3.66)$$

where the subscript p refers to “prescribed” degrees of freedom (degrees of freedom through which the macroscopic \mathbf{F}_M and ${}^3\mathbf{G}_M$ are imposed on the RVE). The subscript f refers to all remaining “free” nodes. System (3.66) is taken at the converged end of the

microstructural increment, thus the residual force in the free nodes can be neglected $\delta f_f^* \approx \underline{0}$. Condensing \underline{u}_f out of the system (3.66) then leads to the definition of the reduced stiffness matrix \underline{K}_M^* that relates the variation of the prescribed degrees of freedom to the variation of the associated forces

$$\underline{K}_M^* \delta \underline{u}_p = \delta \underline{f}_p^*, \quad \text{with} \quad \underline{K}_M^* = \underline{K}_{pp}^* - \underline{K}_{pf}^* (\underline{K}_{ff}^*)^{-1} \underline{K}_{fp}^*. \quad (3.67)$$

Next, relation (3.67) needs to be transformed to arrive at an expression relating variations of the macroscopic stress to variations of the deformation. Since in the second-order computational homogenization framework the macrostructure is modelled as a full second gradient continuum, the linearized constitutive relations are written in the form

$$\delta \mathbf{P}_M = {}^4\mathbf{C}_M^{(1)} : \delta \mathbf{F}_M^c + {}^5\mathbf{C}_M^{(2)} : \delta^3 \mathbf{G}_M^{RC}, \quad (3.68)$$

$$\delta^3 \mathbf{Q}_M = {}^5\mathbf{C}_M^{(3)} : \delta \mathbf{F}_M^c + {}^6\mathbf{C}_M^{(4)} : \delta^3 \mathbf{G}_M^{RC}, \quad (3.69)$$

where the fourth-order tensor ${}^4\mathbf{C}_M^{(1)}$, the fifth-order tensors ${}^5\mathbf{C}_M^{(2)}$ and ${}^5\mathbf{C}_M^{(3)}$ and the sixth-order tensor ${}^6\mathbf{C}_M^{(4)}$ are the macroscopic consistent constitutive tangents. In order to obtain these constitutive tangents from the reduced matrix \underline{K}_M^* , first relation (3.67) is rewritten in a vector/tensor format

$$\sum_j \mathbf{K}_M^{(ij)} \cdot \delta \vec{u}_{(j)} = \delta \vec{f}_{(i)}, \quad i, j = 1, 2, 3, 4, L^*, B^*, \quad (3.70)$$

where the components of tensors $\mathbf{K}_M^{(ij)}$ are simply found in the tangent matrix \underline{K}_M at the rows and columns of the degrees of freedom corresponding to i and j . Next, the expression for the variation of the forces (3.70) is substituted into the relations for the variations of the macroscopic stress and higher-order stress obtained by varying (3.64) and (3.65), which leads to

$$\delta \mathbf{P}_M = \frac{1}{V_0} \sum_i \sum_j (\mathbf{K}_M^{(ij)} \cdot \delta \vec{u}_{(j)}) \vec{X}_{(i)}, \quad (3.71)$$

$$\delta^3 \mathbf{Q}_M^{LC} = \frac{1}{2V_0} \sum_i \sum_j (\mathbf{K}_M^{(ij)} \cdot \delta \vec{u}_{(j)}) \mathbf{Y}_{(i)}, \quad (3.72)$$

where the following notation has been introduced

$$\vec{X}_{L^*} = \int_{\Gamma_{0L}} \vec{X}_L \, d\Gamma_0, \quad \vec{X}_{B^*} = \int_{\Gamma_{0B}} \vec{X}_B \, d\Gamma_0, \quad (3.73)$$

$$\mathbf{Y}_{(i)} = \begin{cases} \vec{X}_{(i)} \vec{X}_{(i)}, & \text{for } i = 1, 2, 3, 4, \\ \int_{\Gamma_{0L}} \vec{X}_L \vec{X}_L \, d\Gamma_0, & \text{for } i = L^*, \\ \int_{\Gamma_{0B}} \vec{X}_B \vec{X}_B \, d\Gamma_0, & \text{for } i = B^*. \end{cases} \quad (3.74)$$

The vectors $\delta \vec{u}_{(j)}$ are now obtained as

$$\delta \vec{u}_{(j)} = \vec{X}_{(j)} \cdot \delta \mathbf{F}_M^c + \frac{1}{2} \mathbf{Y}_{(j)} : \delta^3 \mathbf{G}_M^{RC}. \quad (3.75)$$

Substitution of (3.75) into (3.71) and (3.72) gives

$$\delta \mathbf{P}_M = \frac{1}{V_0} \sum_i \sum_j (\vec{X}_{(i)} \mathbf{K}_M^{(ij)} \vec{X}_{(j)})^{LC} : \delta \mathbf{F}_M^c + \frac{1}{2V_0} \sum_i \sum_j (\vec{X}_{(i)} \mathbf{K}_M^{(ij)} \mathbf{Y}_{(j)})^{LC} : \delta^3 \mathbf{G}_M^{RC}, \quad (3.76)$$

$$\delta^3 \mathbf{Q}_M = \frac{1}{2V_0} \sum_i \sum_j (\mathbf{Y}_{(i)} \mathbf{K}_M^{(ij)} \vec{X}_{(j)})^{LC} : \delta \mathbf{F}_M^c + \frac{1}{4V_0} \sum_i \sum_j (\mathbf{Y}_{(i)} \mathbf{K}_M^{(ij)} \mathbf{Y}_{(j)})^{LC} : \delta^3 \mathbf{G}_M^{RC}. \quad (3.77)$$

Comparing (3.76) and (3.77) with (3.68) and (3.69), the consistent tangents are finally identified as

$$\begin{aligned} {}^4\mathbf{C}_M^{(1)} &= \frac{1}{V_0} \sum_i \sum_j (\vec{X}_{(i)} \mathbf{K}_M^{(ij)} \vec{X}_{(j)})^{LC}, & {}^5\mathbf{C}_M^{(2)} &= \frac{1}{2V_0} \sum_i \sum_j (\vec{X}_{(i)} \mathbf{K}_M^{(ij)} \mathbf{Y}_{(j)})^{LC}, \\ {}^5\mathbf{C}_M^{(3)} &= \frac{1}{2V_0} \sum_i \sum_j (\mathbf{Y}_{(i)} \mathbf{K}_M^{(ij)} \vec{X}_{(j)})^{LC}, & {}^6\mathbf{C}_M^{(4)} &= \frac{1}{4V_0} \sum_i \sum_j (\mathbf{Y}_{(i)} \mathbf{K}_M^{(ij)} \mathbf{Y}_{(j)})^{LC}. \end{aligned} \quad (3.78)$$

3.6 Nested solution scheme

Summarizing the second-order computational homogenization framework, this section discusses the nested solution scheme for the coupled multi-scale numerical analysis.

The structure of the coupled micro-macro program can be outlined as follows. The macroscopic structure to be analyzed is discretized by finite elements. To each macroscopic integration point a unique microstructural RVE is assigned. The geometry and material properties of an RVE are based on the microstructure of the underlying material. The RVE selected should be “representative”, i.e. it should contain sufficient information on the microstructural features and basic mechanisms of their interaction. A discussion on the choice of a microstructural cell in the framework of the second-order computational homogenization may be found in the next section. In order to initiate the macroscopic finite element analysis, constitutive tangents at every integration point are required. To obtain these tangents from the microstructural properties a preparing microstructural analysis is performed. During this initialization the stiffness matrix of an undeformed RVE is assembled and used to derive the initial macroscopic constitutive tangents at a macroscopic integration point.

During the actual analysis the external macroscopic load is applied in increments. For every step of the macroscopic incremental-iterative procedure, and in each macroscopic integration point, the macroscopic deformation gradient tensor \mathbf{F}_M and its gradient ${}^3\mathbf{G}_M$ are calculated based on the current (iterative) macroscopic displacement field. These deformation tensors and gradients of deformation tensors are sent to the microlevel, where they are used to define the boundary value problem for the RVE, corresponding to the respective macroscopic integration point (see section 3.5.1). Upon the solution of every RVE problem, the averaged stress tensor \mathbf{P}_M and the higher-order stress tensor ${}^3\mathbf{Q}_M$ are obtained using (3.64) and (3.65). Additionally, the constitutive tangents are extracted according to (3.78) and returned to the macroscopic program. When the analysis of all RVEs is finished, the stress tensor, the higher-order stress tensor and the consistent constitutive tangents are available at every macroscopic integration

Table 3.1: Incremental-iterative nested multi-scale solution scheme for the second-order computational homogenization.

MACRO		MICRO
1. Initialization <ul style="list-style-type: none"> ▷ initialize the macroscopic model ▷ assign an RVE to every integration point ▷ loop over all integration points <ul style="list-style-type: none"> set $\mathbf{F}_M = \mathbf{I}$ and ${}^3\mathbf{G}_M = {}^3\mathbf{0}$ 	$\xrightarrow{\mathbf{F}_M, {}^3\mathbf{G}_M}$	Initialization RVE analysis <ul style="list-style-type: none"> ▷ prescribe boundary conditions ▷ assemble the RVE stiffness
$\xleftarrow{\text{tangents}}$		<ul style="list-style-type: none"> ▷ calculate the tangents ${}^4\mathbf{C}_M^{(1)}, {}^5\mathbf{C}_M^{(2)}, {}^5\mathbf{C}_M^{(3)}, {}^6\mathbf{C}_M^{(4)}$
<ul style="list-style-type: none"> store the tangents ▷ end integration point loop 		
2. Next increment <ul style="list-style-type: none"> ▷ apply increment of the macro load 		
3. Next iteration <ul style="list-style-type: none"> ▷ assemble the macroscopic tangent stiffness ▷ solve the macroscopic system ▷ loop over all integration points <ul style="list-style-type: none"> calculate \mathbf{F}_M and ${}^3\mathbf{G}_M$ 	$\xrightarrow{\mathbf{F}_M, {}^3\mathbf{G}_M}$	RVE analysis <ul style="list-style-type: none"> ▷ prescribe boundary conditions ▷ assemble the RVE stiffness ▷ solve the RVE problem
$\xleftarrow{\mathbf{P}_M, {}^3\mathbf{Q}_M}$		<ul style="list-style-type: none"> ▷ calculate \mathbf{P}_M and ${}^3\mathbf{Q}_M$
<ul style="list-style-type: none"> store \mathbf{P}_M and ${}^3\mathbf{Q}_M$ store the tangents ▷ end integration point loop ▷ assemble the macroscopic internal forces 		<ul style="list-style-type: none"> ▷ calculate the tangents ${}^4\mathbf{C}_M^{(1)}, {}^5\mathbf{C}_M^{(2)}, {}^5\mathbf{C}_M^{(3)}, {}^6\mathbf{C}_M^{(4)}$
<ul style="list-style-type: none"> ▷ end integration point loop ▷ assemble the macroscopic internal forces 		
4. Check for convergence <ul style="list-style-type: none"> ▷ if not converged \Rightarrow step 3 ▷ else \Rightarrow step 2 		

point. Hence, macroscopic internal nodal forces can be calculated, higher-order equilibrium can be evaluated and, if required, the next macroscopic iteration can be performed. If equilibrium is achieved the calculations can be continued for the next increment. This solution scheme is summarized in Table 3.1.

Obviously, the multi-scale algorithm described above is parallel by its nature. All RVE calculations for one macroscopic iteration can be performed at the same time without any exchange of data between them. So the use of parallel processors for the RVE analyses would significantly reduce the total micro-macro calculation time. In view of this, the current implementation is constructed on the basis of parallel computation. The implementation uses the PVM (Parallel Virtual Machine) software system (Geist et al. (1994)), which essentially provides the library of routines for functions such as

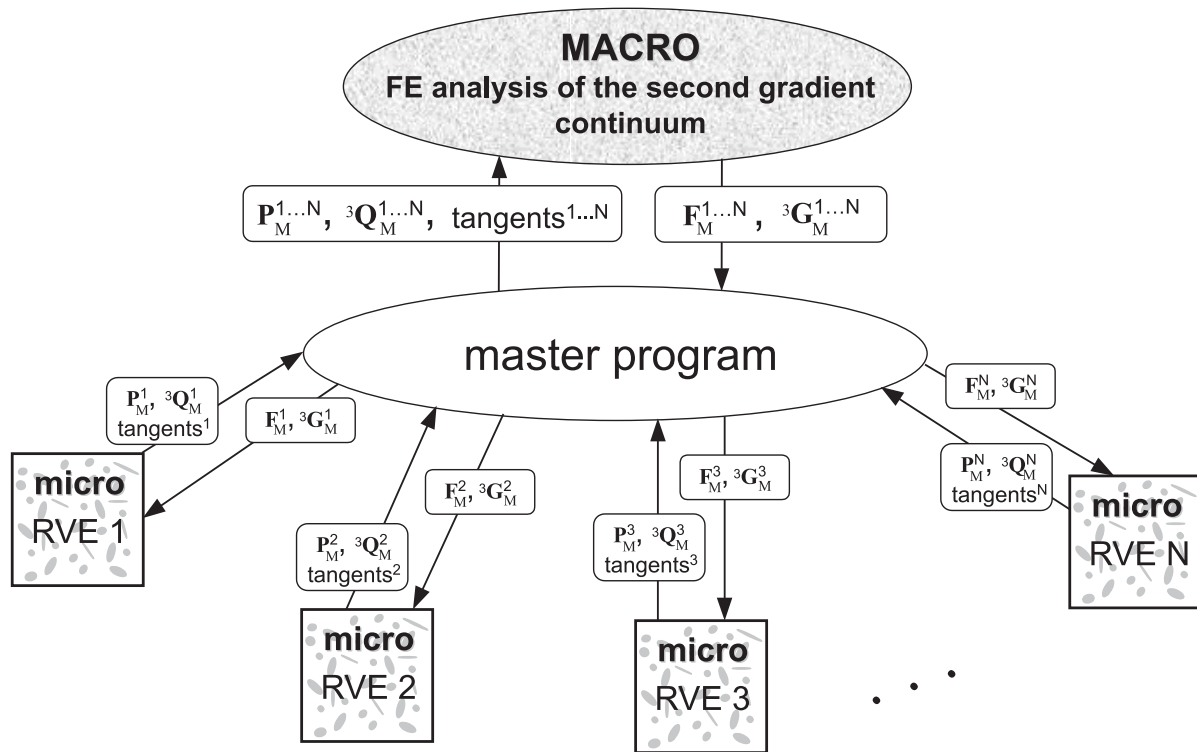


Figure 3.4: Scheme of the parallel implementation of the second-order micro-macro computational homogenization framework; N – number of the integration points in the macroscopic mesh.

parallel process initiation, data transmission, reception, etc. The micro-macro program largely follows a classical master-slaves scheme. The multi-scale analysis is fully controlled by the master program. This master program obtains from the macroanalysis the macroscopic integration point data (deformation gradient tensors and their gradients) and spawns the RVE calculations on the available slave processors along with the data for the RVEs. After the RVE analyses have been completed, the master program collects the RVE averaged stress tensors, the higher-order stress tensors and the constitutive tangents and sends these data back to the macrolevel. This is schematically depicted in Figure 3.4.

3.7 RVEs in the second-order computational homogenization

In the previous chapter the classical notion of a representative volume element has been considered (section 2.7). In the present section the concept of a representative cell in the context of the second-order computational homogenization is discussed.

In the second-order computational homogenization two conflicting requirements on the microstructural representative volume element have to be accommodated. On the one hand, the accurate determination of the overall behaviour of a multi-phase material requires a large representative cell with many (interacting) heterogeneities. On the other hand, the size of a representative cell used in the second-order computational homogenization scheme implicitly sets the macroscopic “resolution”. This resolution

is associated with the macroscopic length scale, which is in fact a length scale of the macroscopic homogenized higher-order continuum obtained through the second-order computational homogenization modelling. This length scale parameter should generally be determined from physical and/or numerical experiments. However, in most cases it is possible to give a reasonable estimate of the required size of the representative cell based on a consideration of the basic mechanisms of the underlying microstructural evolution and interaction.

The representative cell should be selected such that the size is large enough to allow the development of all governing microstructural physical mechanisms. For example, when a primary microstructural deformation mechanism is identified by the formation of microstructural shear bands, the size of the modelling cell should allow for the complete development of these shear bands. Taking the microstructural cell much larger than the minimum required size will in most cases result in a loss of resolution, i.e. in smoothing of the macroscopic fields. After the minimum size of the domain, on which the microstructural phenomena take place, has been defined, a number of different microstructural realizations of this size should be considered and their overall responses averaged. In order to reduce the number of analyses with different realizations of the microstructural cell in some practical cases, different arrangements of the microstructural heterogeneities within a cell should be made in such a way that the statistical characteristics of the microstructure are approximated as accurately as possible.

It is important to remark, that the requirement of statistical representativeness was also present in the definition of an RVE for the classical first-order homogenization approach. However, there was no restriction on the (maximum) size of a representative cell (on the contrary, taking an RVE as large as possible, allowed to represent given statistical characteristics more accurately). This is related to the fact that the classical first-order computational homogenization scheme (as well as most other conventional homogenization methods) deals with an ordinary local continuum on the macroscopic level. Such a continuum does not possess a material length scale and accordingly the size of a microstructural cell does not play a role. The second-order homogenization framework models the macrostructure as a higher-order continuum. The length scale of this continuum is related to the size of the microstructural cell and, consequently, to the size of the microstructural domain, where the basic microstructural phenomena take place. The same relationship appears also in other microstructurally based higher-order constitutive models (e.g. in the mechanism-based strain gradient plasticity theory, Gao et al. (1999)).

Another important aspect of the second-order computational homogenization is associated to the underlying assumption that the macroscopic deformation field varies linearly over the microstructural cell (of which the size should allow to capture the main microstructural deformation mechanisms). If this assumption does not apply (i.e. if the macroscopic fields vary too strongly on the scale of the microstructural constituents) a computational homogenization scheme cannot provide accurate results, since a separation of scales is not recognizable anymore. In such cases the analysis should be performed by detailed microstructural modelling.

Chapter 4

Second gradient continuum formulation for the macrolevel

As indicated in the previous chapter, within the framework of the second-order computational homogenization a proper description of the macrolevel requires a full second gradient equilibrium formulation. In this chapter the continuum description and a computational solution strategy for the second gradient medium are developed. The continuum formulation of the second gradient equilibrium problem is first elaborated. The weak form, which employs Lagrange multipliers to enforce the kinematic relation between the displacement and displacement gradient fields, is presented and its equivalence to the strong form is shown. The finite element formulation includes three unknown fields: displacements, displacement gradients and Lagrange multipliers. An incremental-iterative procedure based on a total Lagrangian setting is outlined. Several quadrilateral isoparametric elements of a mixed type are developed and their performance is examined and compared, using the patch test and the so-called boundary shear layer problem.

4.1 Introduction

The development of higher-order continuum theories started almost a century ago with the famous work of Cosserat and Cosserat (1909). They introduced a continuum, every point of which has six degrees of freedom: three degrees of freedom corresponding to the position in space and three rotational degrees of freedom. Although similar concepts existed before in various theories of beams and shells, the Cosserats were the first to give a systematic theory development for a three-dimensional solid. Another novel feature in the Cosserat theory was the appearance of a non-symmetric stress tensor and additionally a higher-order couple stress tensor. At that time however, the Cosserat theory did not receive much attention and applications were not searched after.

Important developments in higher-order theories have been made in the 1960's. At that time the Cosserat theory was reconsidered and other theories were developed

within the same philosophy. The most widely used among them are the couple stress theory and the full second gradient theory. In the couple stress theory (also called constrained Cosserat theory, Mindlin and Tiersten (1962); Toupin (1962, 1964); Koiter (1964)) the rotation field is determined as the curl of the displacement field in the point of interest. The full second gradient theory (Mindlin (1965); Mindlin and Eshel (1968); Fleck and Hutchinson (1997)) extends this idea to account not only for local rotations, but also for stretch gradients. A higher-order stress (also called double stress) enters the formulation as the work conjugate to the second gradient of the displacement field.

A rather general theory to describe a second-order continuum is the theory of a medium with microstructure, which has been initially developed by Mindlin (1964) and is also discussed in Germain (1973) and Chambon et al. (2001). This theory is based on a continuum concept, in which each point is considered as a deformable medium itself. The kinematics of a continuum with microstructure is defined by macro- and microdisplacement fields. The potential energy density of such a continuum is assumed to be a function of the macrodeformation, the microdeformation and the gradient of the microdeformation. With the addition of some kinematic constraints, this general theory recovers the previously mentioned theories as particular cases. If the symmetric part of the microdeformation vanishes, the Cosserat continuum is obtained. Additionally, requiring the macrorotation to be equal to the microrotation leads to the couple stress theory. Alternatively, assuming the microdeformation to equal the macrodeformation reduces the theory of a medium with microstructure to the full second gradient theory. Other higher-order continuum theories developed at that time are the micromorphic theory (Eringen (1964)), the micropolar theory (Eringen (1966)), the multipolar theory (Green and Rivlin (1964)), etc.

While the attention in the 1960's was mainly focused on the elaboration of the general concepts of elastic higher-order media, the past decades concentrated on various non-linear (e.g. elasto-plastic) higher-order theories, both phenomenological and microstructurally based. These theories have found most of their applications in the modelling of localization and size effects, particularly in the fields of geomechanics and metal plasticity. As has been recognized, the presence of higher-order gradients of kinematic quantities and/or internal variables in a formulation prevents loss of ellipticity of the governing equations and allows for a realistic description of localized deformations beyond the bifurcation point when the material is far in the softening regime. Additionally, an intrinsic length scale incorporated in higher-order theories allows for the modelling of size effects, often observed in experiments. Account of these theories and their applications may be found among a vast amount of references in e.g. Aifantis (1984); Vardoulakis and Aifantis (1991); de Borst and Mühlhaus (1992); de Borst et al. (1993); Fleck and Hutchinson (1993); Fleck et al. (1994); Fleck and Hutchinson (1997); Shu and Fleck (1999); Gao et al. (1999); Huang et al. (2000).

Even more so than for a conventional continuum, analytical solutions for higher-order continua may be obtained only for a few very simple problems. For the solution of practical problems one must resort to a numerical analysis, e.g. the finite element method. If a Cosserat continuum is to be modelled, the finite element implementation is relatively easy. In this case the classical displacement based formulation is simply extended by adding the rotational degrees of freedom to every node and properly rewriting the element matrices (e.g. de Borst (1991)). However, modelling of the constrained types of higher-order continua requires significantly more effort. The difficulty origi-

nates from the fact that in this case the higher-order kinematic quantities (e.g. rotation or the gradient of the deformation) are not independent of the displacement field. This leads to a virtual work statement, which includes the first- and second-order derivatives of the displacement. As a consequence, a displacement based finite element formulation should employ at least C^1 continuous interpolation functions for the displacement field. In the framework of the couple stress theory, Xia and Hutchinson (1996) have proposed C^1 continuous elements for anti-plane and plane strain deformation and later for the axisymmetric case (Begley and Hutchinson (1998)). Another C^1 continuous element for the full second gradient formulation has been recently proposed by Zervos et al. (2001). However, C^1 continuous elements are relatively complicated to formulate and implement due to the geometrical restrictions that apply to them. Moreover, as has been pointed out by Xia and Hutchinson (1996), these elements do not always lead to adequate results for the second-order continuum, even though similar elements are known to be superior for plate bending.

The lack of robust C^1 continuous elements motivated the same authors (Xia and Hutchinson (1996)) to develop a C^0 continuous element based on a mixed formulation for the couple stress theory, initially proposed by Herrmann (1983). In the mixed formulation the displacement and its gradient are considered as independent unknowns. The Lagrange multiplier technique is used to impose the kinematic constraints between these independent variables. Later Shu and Fleck (1998) have used a similar couple stress formulation, but they enforced the constraints using penalty functions. Shu et al. (1999) developed a series of C^0 mixed type quadrilateral and triangular elements for the full second gradient formulation and conducted a comparison of their performance. Recently also Amanatidou and Aravas (2002) and Matsushima et al. (2002) presented various types of mixed formulations and elements for the second gradient continuum. It is also worth mentioning that among all finite element formulations for a higher-order continuum only a few are developed within a large deformations framework (Shu and Barlow (2000); Matsushima et al. (2002)).

In this chapter, first the strong form of equilibrium for the full second gradient continuum is derived. In section 4.3.1 this strong form is recast into a mixed type weak form and the equivalence between the weak and the strong form is demonstrated. The finite element discretization of this weak form, which requires a discretization of three unknown fields: displacement, displacement gradient and Lagrange multipliers, is presented in section 4.3.2. The linearized form of the discrete system of equations in the total Lagrange framework is elaborated in section 4.3.3. Next, several types of nine and eight noded quadrilateral elements for the mixed second gradient formulation are proposed in section 4.3.4 and section 4.4 deals with the assessment and comparison of the performance of the elements developed. First, Mindlin's elastic constitutive model for a second gradient continuum is briefly summarized. Then the patch test is performed, which allows to indicate poorly behaving elements. Convergence and accuracy of the elements is further evaluated by comparing the numerical results with an analytical solution for the so-called boundary shear layer problem. This chapter concludes with recommendations on the choice of a suitable finite element for solving general boundary value problems for a second gradient continuum and for use within the framework of the second-order computational homogenization in particular.

4.2 Second gradient continuum formulation

Kinematics of a classical continuum is defined by the non-linear deformation mapping $\vec{x} = \vec{\phi}(\vec{X}, t)$, which maps the reference configuration position vector \vec{X} onto the current configuration position vector \vec{x} at time t . In classical models the internal work is determined by the gradient of this deformation mapping, i.e. the well-known deformation gradient tensor

$$\mathbf{F} = \left(\frac{\partial \vec{\phi}}{\partial \vec{X}} \right)^c = (\nabla_0 \vec{x})^c. \quad (4.1)$$

In the second gradient continuum theory also the gradient of the deformation gradient tensor

$${}^3\mathbf{G} = \frac{\partial}{\partial \vec{X}} \left(\frac{\partial \vec{\phi}}{\partial \vec{X}} \right)^c = \nabla_0 \mathbf{F}, \quad G_{ijk} = G_{kji} \quad (4.2)$$

is included into the mechanical description of a continuum. The internal work is then assumed to be determined by the deformation gradient tensor \mathbf{F} and its (Lagrangian) gradient ${}^3\mathbf{G}$. Following the classical arguments of objectivity (frame indifference) the virtual internal work increment per unit undeformed volume of a solid due to an arbitrary virtual variation $\delta \vec{u}$ of the displacement $\vec{u} = \vec{x} - \vec{X}$ is written as

$$\delta w_0^{int} = \mathbf{P} : \delta \mathbf{F}^c + {}^3\mathbf{Q} : \delta {}^3\mathbf{G}, \quad (4.3)$$

where the first Piola-Kirchhoff stress tensor \mathbf{P} is the work conjugate of the variation of the deformation gradient tensor $\delta \mathbf{F}$, and the higher-order stress ${}^3\mathbf{Q}$ (with the symmetry property $Q_{ijk} = Q_{kji}$, associated to the minor symmetry of the tensor ${}^3\mathbf{G}$) is the work conjugate of the variation of the gradient $\delta {}^3\mathbf{G}$ of the deformation gradient tensor.

The variation of the internal work for an initially undeformed volume V_0 equals

$$\delta W_0^{int} = \int_{V_0} \delta w_0 dV_0 = \int_{V_0} (\mathbf{P} : \delta \mathbf{F}^c + {}^3\mathbf{Q} : \delta {}^3\mathbf{G}) dV_0. \quad (4.4)$$

By explicitly writing the variation of the deformation gradient tensor and the variation of its gradient in terms of the displacement variation, (4.4) takes the form

$$\delta W_0^{int} = \int_{V_0} (\mathbf{P} : \nabla_0 \delta \vec{u} + {}^3\mathbf{Q} : \nabla_0 (\nabla_0 \delta \vec{u})^c) dV_0. \quad (4.5)$$

Using the following identities

$$\mathbf{P} : \nabla_0 \delta \vec{u} = \nabla_0 \cdot (\mathbf{P}^c \cdot \delta \vec{u}) - (\nabla_0 \cdot \mathbf{P}^c) \cdot \delta \vec{u}, \quad (4.6)$$

$${}^3\mathbf{Q} : \nabla_0 (\nabla_0 \delta \vec{u})^c = \nabla_0 \cdot ({}^3\mathbf{Q} : \nabla_0 \delta \vec{u}) - \nabla_0 \cdot (\delta \vec{u} \cdot (\nabla_0 \cdot {}^3\mathbf{Q})) + (\nabla_0 \cdot (\nabla_0 \cdot {}^3\mathbf{Q})^c) \cdot \delta \vec{u}, \quad (4.7)$$

and applying the divergence theorem, the work variation (4.5) is transformed into

$$\begin{aligned} \delta W_0^{int} = & - \int_{V_0} \left[\nabla_0 \cdot (\mathbf{P}^c - (\nabla_0 \cdot {}^3\mathbf{Q})^c) \right] \cdot \delta \vec{u} \, dV_0 \\ & + \int_{S_0} \vec{N} \cdot (\mathbf{P}^c - (\nabla_0 \cdot {}^3\mathbf{Q})^c) \cdot \delta \vec{u} \, dS_0 + \int_{S_0} \vec{N} \cdot {}^3\mathbf{Q} : \nabla_0 \delta \vec{u} \, dS_0, \end{aligned} \quad (4.8)$$

where \vec{N} is the unit outward normal to the surface S_0 of the body in its reference (undeformed) configuration. Note, that $\nabla_0 \delta \vec{u}$ is the full gradient, which cannot be determined from $\delta \vec{u}$ on the surface S_0 alone. If $\delta \vec{u}$ is known on the entire surface S_0 , the surface gradient of $\delta \vec{u}$ can be easily determined, but not the full gradient. Thus, in order to correctly identify the independent boundary conditions in a variational principle, the gradient $\nabla_0 \delta \vec{u}$ is decomposed into a surface gradient $\nabla_0^s \delta \vec{u}$ and a normal gradient $\vec{N} D_0 \delta \vec{u}$

$$\nabla_0 \delta \vec{u} = \nabla_0^s \delta \vec{u} + \vec{N} D_0 \delta \vec{u}, \quad (4.9)$$

where the surface gradient operator is defined as

$$\nabla_0^s = (\mathbf{I} - \vec{N} \vec{N}) \cdot \nabla_0 \quad (4.10)$$

and the normal gradient operator as

$$D_0 = \vec{N} \cdot \nabla_0. \quad (4.11)$$

In order to eliminate the surface gradient $\nabla_0^s \delta \vec{u}$ from (4.8) and to retain only the independent variations $\delta \vec{u}$ and $D_0 \delta \vec{u}$ the following mathematical manipulations are performed.

If \mathbf{A} is an arbitrary second-order tensor and \vec{a} a vector, then the identity

$$\mathbf{A} : \nabla_0 \vec{a} = \nabla_0^s \cdot (\mathbf{A}^c \cdot \vec{a}) - (\nabla_0^s \cdot \mathbf{A}^c) \cdot \vec{a} + \vec{N} \cdot \mathbf{A}^c \cdot D_0 \vec{a} \quad (4.12)$$

holds, where (4.9) and a relation similar to (4.6) (with ∇_0^s instead of ∇_0) have been used.

The following integral transformation holds for a continuously differentiable vector function \vec{f} defined on a surface S_0 bounded by a closed curve ℓ_0 (Brand (1947))

$$\int_{S_0} \nabla_0^s \cdot \vec{f} \, dS_0 = \int_{S_0} (\nabla_0^s \cdot \vec{N}) \vec{N} \cdot \vec{f} \, dS_0 + \oint_{\ell_0} \vec{m} \cdot \vec{f} \, d\ell_0, \quad (4.13)$$

where the vector \vec{m} satisfies $\vec{m} = \vec{T} \times \vec{N}$, with \vec{T} the unit tangent vector along the curve ℓ_0 defined such that \vec{m} is directed outward viewed from the surface S_0 . Suppose now that S_0 is a closed surface which is divided into two parts $S_0^{(1)}$ and $S_0^{(2)}$ by a curve ℓ_0 . Let $\ell_0^{(1)}$ and $\ell_0^{(2)}$ be the curves, closing the surfaces $S_0^{(1)}$ and $S_0^{(2)}$, respectively; in fact $\ell_0^{(1)}$ and $\ell_0^{(2)}$ indicate the same curve. According to the above procedure, along the curves $\ell_0^{(1)}$ and $\ell_0^{(2)}$ the following unit vectors are defined: the normals $\vec{N}^{(1)}$ and $\vec{N}^{(2)}$ (not necessarily equal), the tangents $\vec{T}^{(1)}$ and $\vec{T}^{(2)}$ (with $\vec{T}^{(2)} = -\vec{T}^{(1)}$), and the vectors $\vec{m}^{(1)} = \vec{T}^{(1)} \times \vec{N}^{(1)}$

and $\vec{m}^{(2)} = \vec{T}^{(2)} \times \vec{N}^{(2)}$. For each surface segment $S_0^{(1)}$ and $S_0^{(2)}$ (4.13) applies. For the whole surface S_0 it can be written then

$$\int_{S_0} \nabla_0^s \cdot \vec{f} \, dS_0 = \int_{S_0} (\nabla_0^s \cdot \vec{N}) \vec{N} \cdot \vec{f} \, dS_0 + \oint_{\ell_0^{(1)}} \vec{m}^{(1)} \cdot \vec{f}^{(1)} \, d\ell_0^{(1)} + \oint_{\ell_0^{(2)}} \vec{m}^{(2)} \cdot \vec{f}^{(2)} \, d\ell_0^{(2)}. \quad (4.14)$$

The contribution of the line integrals may be further elaborated according to

$$\begin{aligned} & \oint_{\ell_0^{(1)}} \vec{m}^{(1)} \cdot \vec{f}^{(1)} \, d\ell_0^{(1)} + \oint_{\ell_0^{(2)}} \vec{m}^{(2)} \cdot \vec{f}^{(2)} \, d\ell_0^{(2)} = \\ & \oint_{\ell_0^{(1)}} (\vec{T}^{(1)} \times \vec{N}^{(1)}) \cdot \vec{f}^{(1)} \, d\ell_0^{(1)} + \oint_{\ell_0^{(2)}} (\vec{T}^{(2)} \times \vec{N}^{(2)}) \cdot \vec{f}^{(2)} \, d\ell_0^{(2)} = \\ & \oint_{\ell_0^{(1)}} \left((\vec{T}^{(1)} \times \vec{N}^{(1)}) \cdot \vec{f}^{(1)} - (\vec{T}^{(1)} \times \vec{N}^{(2)}) \cdot \vec{f}^{(2)} \right) \, d\ell_0^{(1)} = \oint_{\ell_0^{(1)}} [\vec{m} \cdot \vec{f}] \, d\ell_0^{(1)}, \end{aligned} \quad (4.15)$$

where the symbol $[\dots]$ denotes the difference in value of the enclosed quantity as a given point on an edge $\ell_0^{(1)}$ is approached from either side. More generally, a piecewise smooth surface S_0 can be divided into a finite number of smooth parts. Then the integral transformation takes the form

$$\int_{S_0} \nabla_0^s \cdot \vec{f} \, dS_0 = \int_{S_0} (\nabla_0^s \cdot \vec{N}) \vec{N} \cdot \vec{f} \, dS_0 + \sum_n \oint_{\ell_0^{(n)}} [\vec{m} \cdot \vec{f}] \, d\ell_0^{(n)}. \quad (4.16)$$

If S_0 is a smooth surface (does not have edges and corners) then the last term in (4.16) vanishes.

Integrating (4.12) over the surface S_0 and using (4.16) with $\vec{f} = \mathbf{A}^c \cdot \vec{a}$ gives

$$\begin{aligned} \int_{S_0} \mathbf{A} : \nabla_0 \vec{a} \, dS_0 &= \int_{S_0} (\nabla_0^s \cdot \vec{N}) \vec{N} \cdot \mathbf{A}^c \cdot \vec{a} \, dS_0 - \int_{S_0} (\nabla_0^s \cdot \mathbf{A}^c) \cdot \vec{a} \, dS_0 \\ &+ \int_{S_0} \vec{N} \cdot \mathbf{A}^c \cdot D_0 \vec{a} \, dS_0 + \sum_n \oint_{\ell_0^{(n)}} [\vec{m} \cdot \mathbf{A}^c \cdot \vec{a}] \, d\ell_0^{(n)}. \end{aligned} \quad (4.17)$$

Now taking in the above relation $\vec{a} \equiv \delta \vec{u}$ and $\mathbf{A} \equiv \vec{N} \cdot \mathbf{Q}$, as present in the last term of (4.8), substituting the result back into (4.8) and combining terms in the variations $\delta \vec{u}$ and $D_0 \delta \vec{u}$, the variation of the internal work becomes

$$\begin{aligned} \delta W_0^{int} &= - \int_{V_0} \left[\nabla_0 \cdot (\mathbf{P}^c - (\nabla_0 \cdot \mathbf{Q})^c) \right] \cdot \delta \vec{u} \, dV_0 \\ &+ \int_{S_0} \left[\vec{N} \cdot (\mathbf{P}^c - (\nabla_0 \cdot \mathbf{Q})^c) + (\nabla_0^s \cdot \vec{N}) \vec{N} \cdot (\vec{N} \cdot \mathbf{Q})^c - \nabla_0^s \cdot (\vec{N} \cdot \mathbf{Q})^c \right] \cdot \delta \vec{u} \, dS_0 \\ &+ \int_{S_0} \left[\vec{N} \cdot \mathbf{Q} \cdot \vec{N} \right] \cdot D_0 \delta \vec{u} \, dS_0 + \sum_n \oint_{\ell_0^{(n)}} [\vec{m} \cdot (\vec{N} \cdot \mathbf{Q})^c] \cdot \delta \vec{u} \, d\ell_0^{(n)}. \end{aligned} \quad (4.18)$$

According to the principle of virtual work, the work performed by internal forces on virtual displacements equals the work of external forces on the same virtual displacements. Considering the structure of (4.18) the external work is assumed to be expressed according to

$$\delta W_0^{ext} = \int_{V_0} \vec{b} \cdot \delta \vec{u} \, dV_0 + \int_{S_0} \vec{t} \cdot \delta \vec{u} \, dS_0 + \int_{S_0} \vec{r} \cdot D_0 \delta \vec{u} \, dS_0 + \sum_n \oint_{\ell_0^{(n)}} \vec{p}^{(n)} \cdot \delta \vec{u} \, d\ell_0^{(n)}, \quad (4.19)$$

where \vec{b} is the body force per unit undeformed volume, while the loading vectors \vec{t} , \vec{r} and $\vec{p}^{(n)}$ are defined in the following. Combining (4.18) and (4.19), which are valid for any subdomain of V_0 and arbitrary variations $\delta \vec{u}$ and $D_0 \delta \vec{u}$, results in the local *equilibrium equation*

$$\nabla_0 \cdot (\mathbf{P}^c - (\nabla_0 \cdot \mathbf{Q})^c) + \vec{b} = \vec{0} \quad (4.20)$$

and boundary conditions on the part of the surface S_0 where tractions are prescribed. These natural (also called dynamic) boundary conditions consist of the *surface traction* \vec{t}

$$\vec{t} = \vec{N} \cdot (\mathbf{P}^c - (\nabla_0 \cdot \mathbf{Q})^c) + (\nabla_0^s \cdot \vec{N}) \vec{N} \cdot (\vec{N} \cdot \mathbf{Q})^c - \nabla_0^s \cdot (\vec{N} \cdot \mathbf{Q})^c \quad (4.21)$$

and the *double stress traction* \vec{r}

$$\vec{r} = \vec{N} \cdot \mathbf{Q} \cdot \vec{N}. \quad (4.22)$$

In case that S_0 is a piece-wise smooth surface on every edge $\ell_0^{(n)}$ the *line force* $\vec{p}^{(n)}$ is defined as

$$\vec{p}^{(n)} = \llbracket \vec{m} \cdot (\vec{N} \cdot \mathbf{Q})^c \rrbracket. \quad (4.23)$$

On the remaining part of S_0 , the displacement \vec{u} and its normal gradient $D_0 \vec{u}$ should be prescribed. Like for a classical medium combinations of kinematic and dynamic boundary conditions (mixed boundary conditions) are also admissible.

In order to complete the system of equations (4.20)-(4.23), constitutive relations are required. Here, however, no particular constitutive laws are specified. Instead, a general form of constitutive equations, relating the first Piola-Kirchhoff stress tensor \mathbf{P} and the higher-order stress tensor \mathbf{Q} to the history of the deformation tensor \mathbf{F} and its gradient \mathbf{G} , is supposed

$$\mathbf{P}(\vec{X}, t) = \mathcal{F}^P \{ \mathbf{F}(\vec{X}, \tau), \mathbf{G}(\vec{X}, \tau), \tau \in [0, t] \}, \quad (4.24)$$

$$\mathbf{Q}(\vec{X}, t) = \mathcal{F}^Q \{ \mathbf{F}(\vec{X}, \tau), \mathbf{G}(\vec{X}, \tau), \tau \in [0, t] \}. \quad (4.25)$$

4.3 Finite element implementation

The equilibrium equations derived above combined with constitutive equations and boundary conditions constitute a system of partial differential equations. This system is often non-linear due to geometrical and/or material non-linearities. Analytical solutions can be obtained only for extremely simple geometries and loading conditions.

Therefore, for the analysis of practical multi-dimensional problems with complex geometries and loading conditions approximate, numerical methods are required. Among other numerical techniques, the finite element method enables to obtain such an approximate solution in a systematic way. The finite element technique is widely used for the solution of engineering problems formulated for a classical continuum. The same methodology can be used for the numerical solution of higher-order continuum problems.

4.3.1 Weak formulation

The finite element discretization of a boundary value problem is based on a weak form, also called a weighted residuals form, or a variational form. The straightforward application of the weighted residuals approach to equilibrium equation (4.20) results in a weak formulation expressed as the virtual energy balance $\delta W_0^{int} = \delta W_0^{ext}$, with the variation of the internal work equivalent to (4.4), which includes the first and the second-order derivatives of the displacement. This immediately indicates that the direct usage of conventional displacement-based finite elements requires at least C^1 continuous interpolation functions, i.e. both the function and its first derivative are required to be continuous across inter-element boundaries. Several C^1 continuous elements have been proposed for a higher-order continuum (e.g. Xia and Hutchinson (1996); Begley and Hutchinson (1998); Zervos et al. (2001)). However, development of C^1 continuous elements suitable for general multi-dimensional non-linear problems is not straightforward, since these elements usually require additional assumptions (e.g. geometrical) and suffer from various restrictions.

Due to the lack of robust C^1 continuous elements, the use of C^0 continuous elements is preferred. Development of C^0 continuous elements for higher-order continua is based on a mixed (also called multi-field) formulation. The strategy is to introduce another unknown field of the second-order tensor, denoted $\hat{\mathbf{F}}$, in addition to the unknown displacement field \vec{u} . The kinematic constraint between these two fields is weakly enforced by means of Lagrange multipliers, also forming a second-order tensor field.

The weak form, which accounts for the appropriate field equations, (natural) boundary conditions and the relationships $\hat{\mathbf{F}} = \mathbf{F}$ in the volume, enforced by the Lagrange multiplier $\boldsymbol{\lambda}$, and $\hat{\mathbf{F}}_s = (\nabla_0^s \vec{u})^c$ on the surface (with $\hat{\mathbf{F}}_s = \hat{\mathbf{F}} - \hat{\mathbf{F}} \cdot \vec{N} \vec{N}$ the surface part of the tensor $\hat{\mathbf{F}}$), enforced by another Lagrange multiplier $\boldsymbol{\mu}$, may be written as (the proof of this statement is presented in the following)

$$\begin{aligned} & \int_{V_0} \left\{ \mathbf{P}(\mathbf{F}, {}^3\hat{\mathbf{G}}) : \delta \mathbf{F}^c + {}^3\mathbf{Q}(\mathbf{F}, {}^3\hat{\mathbf{G}}) : \delta {}^3\hat{\mathbf{G}} + \delta(\boldsymbol{\lambda} : (\hat{\mathbf{F}}^c - \mathbf{F}^c)) \right\} dV_0 \\ & + \int_{S_0} \delta(\boldsymbol{\mu} : (\hat{\mathbf{F}}_s^c - \nabla_0^s \vec{u})) dS_0 = \int_{V_0} \vec{b} \cdot \delta \vec{u} dV_0 + \int_{S_0} \vec{t} \cdot \delta \vec{u} dS_0 \\ & + \int_{S_0} \mathbf{R} : \delta \hat{\mathbf{F}}^c dS_0 + \sum_n \oint_{\ell_0^{(n)}} \vec{p}^{(n)} \cdot \delta \vec{u} d\ell_0^{(n)}, \end{aligned} \quad (4.26)$$

In (4.26) the deformation gradient tensor \mathbf{F} is obtained from the displacement field \vec{u} via the standard kinematics relation

$$\mathbf{F} = (\nabla_0 \vec{x})^c = \mathbf{I} + (\nabla_0 \vec{u})^c, \quad \delta \mathbf{F} = (\nabla_0 \delta \vec{u})^c. \quad (4.27)$$

The variable ${}^3\hat{\mathbf{G}}$ is a third-order tensor defined as the gradient of the field $\hat{\mathbf{F}}$, symmetrized on the first and the last indices

$$\hat{G}_{ijk} = \frac{1}{2}(\nabla_{0i}\hat{F}_{jk} + \nabla_{0k}\hat{F}_{ji}), \quad \delta\hat{G}_{ijk} = \frac{1}{2}(\nabla_{0i}\delta\hat{F}_{jk} + \nabla_{0k}\delta\hat{F}_{ji}). \quad (4.28)$$

In the right-hand side of (4.26) \mathbf{R} is a double traction tensor, which is related to the double traction vector \vec{r} by

$$\mathbf{R} = \vec{r}\vec{N}. \quad (4.29)$$

In the weak form (4.26) the dependence of the stress tensor and the higher-order stress tensor on kinematic quantities has been explicitly indicated. Thus, when the stress and the higher-order stress are calculated via the constitutive relations (4.24) and (4.25) the deformation gradient tensor according to (4.27) is used, while for the gradient of the deformation gradient tensor (4.28) is employed. This choice has been made in the present implementation, however, other alternatives are possible.

Only the first-order derivatives of the primary unknown fields \vec{u} and $\hat{\mathbf{F}}$ and their corresponding weighting functions $\delta\vec{u}$ and $\delta\hat{\mathbf{F}}$ appear in the weak form (4.26), so they are only required to be piece-wise differentiable, i.e. C^0 continuous. Following Shu et al. (1999), the unknown $\hat{\mathbf{F}}$ is sometimes called the “relaxed” deformation gradient tensor. It also should be noted that there are fundamental differences with respect to the assumed deformation used in mixed formulations for a classical continuum, namely the continuity requirements and the boundary conditions. No derivatives of the Lagrange multipliers appear in this weak form, so the Lagrange multipliers should only be piece-wise continuous functions of \vec{X} , so C^{-1} continuous functions.

In the following it is demonstrated that the weak form (4.26) is equivalent to the strong form (4.20)-(4.23). First, the first term in the left-hand side of (4.26) is elaborated by replacing $\delta\mathbf{F}^c$ with $\nabla_0\delta\vec{u}$, using (4.6) and applying the divergence theorem. This gives

$$\int_{V_0} \mathbf{P} : \delta\mathbf{F}^c \, dV_0 = - \int_{V_0} (\nabla_0 \cdot \mathbf{P}^c) \cdot \delta\vec{u} \, dV_0 + \int_{S_0} \vec{N} \cdot \mathbf{P}^c \cdot \delta\vec{u} \, dS_0 + \int_{S_0^{t,int}} [[\vec{N} \cdot \mathbf{P}^c]] \cdot \delta\vec{u} \, dS_0, \quad (4.30)$$

where $S_0^{t,int}$ is the “internal boundary”, i.e. the union of all surfaces (lines in two dimensions) on which a priori the stresses are allowed to be discontinuous in the body.

Next the second term in (4.26) is transformed in a similar way. Substitution of (4.28) into this term with account for the differentiation formula (where the symmetry property of ${}^3\mathbf{Q}$, $Q_{ijk} = Q_{kji}$ is used) according to

$${}^3\mathbf{Q} : \nabla_0\delta\hat{\mathbf{F}} = \nabla_0 \cdot ({}^3\mathbf{Q} : \delta\hat{\mathbf{F}}^c) - (\nabla_0 \cdot {}^3\mathbf{Q}) : \delta\hat{\mathbf{F}}^c \quad (4.31)$$

and application of the divergence theorem yields

$$\begin{aligned} \int_{V_0} {}^3\mathbf{Q} : \delta{}^3\hat{\mathbf{G}} \, dV_0 = & - \int_{V_0} (\nabla_0 \cdot {}^3\mathbf{Q}) : \delta\hat{\mathbf{F}}^c \, dV_0 + \int_{S_0} \vec{N} \cdot {}^3\mathbf{Q} : \delta\hat{\mathbf{F}}_s^c \, dS_0 \\ & + \int_{S_0} \vec{N} \cdot {}^3\mathbf{Q} : (\vec{N}\vec{N} \cdot \delta\hat{\mathbf{F}}^c) \, dS_0 + \int_{S_0^{r,int}} [[\vec{N} \cdot {}^3\mathbf{Q}]] : \delta\hat{\mathbf{F}}^c \, dS_0, \end{aligned} \quad (4.32)$$

where $\delta\hat{\mathbf{F}}$ on the boundary S_0 has been split into a tangential and a normal part $\delta\hat{\mathbf{F}}^c = \delta\hat{\mathbf{F}}_s^c + \vec{N}\vec{N} \cdot \delta\hat{\mathbf{F}}^c$; $S_0^{r,int}$ is the internal boundary, on which the higher-order stress might be discontinuous.

For the last term in the volume integral in the left-hand side of (4.26) the variational rule $\delta(uv) = \delta uv + u\delta v$ is used, followed by substitution of (4.27₂), application of (4.6) (with replacement of \mathbf{P} by $\boldsymbol{\lambda}$) and the divergence theorem

$$\begin{aligned} \int_{V_0} \delta(\boldsymbol{\lambda} : (\hat{\mathbf{F}}^c - \mathbf{F}^c)) dV_0 &= \int_{V_0} \delta\boldsymbol{\lambda} : (\hat{\mathbf{F}}^c - \mathbf{F}^c) dV_0 + \int_{V_0} \boldsymbol{\lambda} : \delta\hat{\mathbf{F}}^c dV_0 \\ + \int_{V_0} (\nabla_0 \cdot \boldsymbol{\lambda}^c) \cdot \delta\vec{u} dV_0 - \int_{S_0} \vec{N} \cdot \boldsymbol{\lambda}^c \cdot \delta\vec{u} dS_0 - \int_{S_0^{t,int}} [\vec{N} \cdot \boldsymbol{\lambda}^c] \cdot \delta\vec{u} dS_0. \end{aligned} \quad (4.33)$$

Similarly, the surface term in the left-hand side of (4.26) is elaborated

$$\begin{aligned} \int_{S_0} \delta(\boldsymbol{\mu} : (\hat{\mathbf{F}}_s^c - \nabla_0^s \vec{u})) dS_0 &= \int_{S_0} \delta\boldsymbol{\mu} : (\hat{\mathbf{F}}_s^c - \nabla_0^s \vec{u}) dS_0 + \int_{S_0} \boldsymbol{\mu} : \delta\hat{\mathbf{F}}_s^c dS_0 \\ - \int_{S_0} (\nabla_0^s \cdot \vec{N}) \vec{N} \cdot \boldsymbol{\mu}^c \cdot \delta\vec{u} dS_0 + \int_{S_0} (\nabla_0^s \cdot \boldsymbol{\mu}^c) \cdot \delta\vec{u} dS_0 - \sum_n \oint_{\ell_0^{(n)}} [\vec{m} \cdot \boldsymbol{\mu}^c] \cdot \delta\vec{u} d\ell_0^{(n)}, \end{aligned} \quad (4.34)$$

where the integral transformation (4.13) has been used.

Finally substituting (4.30)-(4.34) into (4.26) and recombining the terms results in

$$\begin{aligned} \int_{V_0} [\nabla_0 \cdot (\mathbf{P}^c - \boldsymbol{\lambda}^c) + \vec{b}] \cdot \delta\vec{u} dV_0 + \int_{V_0} (\nabla_0 \cdot {}^3\mathbf{Q} - \boldsymbol{\lambda}) : \delta\hat{\mathbf{F}}^c dV_0 - \int_{V_0} \delta\boldsymbol{\lambda} : (\hat{\mathbf{F}}^c - \mathbf{F}^c) dV_0 \\ + \int_{S_0} [\vec{t} - \vec{N} \cdot (\mathbf{P}^c - \boldsymbol{\lambda}^c) + (\nabla_0^s \cdot \vec{N}) \vec{N} \cdot \boldsymbol{\mu}^c - \nabla_0^s \cdot \boldsymbol{\mu}^c] \cdot \delta\vec{u} dS_0 \\ + \int_{S_0} [\vec{r} - \vec{N} \cdot {}^3\mathbf{Q} \cdot \vec{N}] \cdot (\vec{N} \cdot \delta\hat{\mathbf{F}}^c) dS_0 - \int_{S_0} (\boldsymbol{\mu} + \vec{N} \cdot {}^3\mathbf{Q}) : \delta\hat{\mathbf{F}}_s^c dS_0 \\ - \int_{S_0} \delta\boldsymbol{\mu} : (\hat{\mathbf{F}}_s^c - \nabla_0^s \vec{u}) dS_0 + \sum_n \oint_{\ell_0^{(n)}} [\vec{p}^{(n)} + [\vec{m} \cdot \boldsymbol{\mu}^c]] \cdot \delta\vec{u} d\ell_0^{(n)} \\ - \int_{S_0^{t,int}} [\vec{N} \cdot (\mathbf{P}^c - \boldsymbol{\lambda}^c)] \cdot \delta\vec{u} dS_0 - \int_{S_0^{r,int}} [\vec{N} \cdot {}^3\mathbf{Q}] : \delta\hat{\mathbf{F}}^c dS_0 = 0. \end{aligned} \quad (4.35)$$

Using the arbitrariness of the variations then gives

$$\nabla_0 \cdot (\mathbf{P}^c - \boldsymbol{\lambda}^c) + \vec{b} = \vec{0} \quad \text{in } V_0, \quad (4.36)$$

$$\boldsymbol{\lambda} = \nabla_0 \cdot \mathbf{Q} \quad \text{in } V_0, \quad (4.37)$$

$$\hat{\mathbf{F}}^c = \mathbf{F}^c \quad \text{in } V_0, \quad (4.38)$$

$$\vec{t} = \vec{N} \cdot (\mathbf{P}^c - \boldsymbol{\lambda}^c) - (\nabla_0^s \cdot \vec{N}) \vec{N} \cdot \boldsymbol{\mu}^c + \nabla_0^s \cdot \boldsymbol{\mu}^c \quad \text{on } S_0, \quad (4.39)$$

$$\vec{r} = \vec{N} \cdot \mathbf{Q} \cdot \vec{N} \quad \text{on } S_0, \quad (4.40)$$

$$\boldsymbol{\mu} = -\vec{N} \cdot \mathbf{Q} \quad \text{on } S_0, \quad (4.41)$$

$$\hat{\mathbf{F}}_s^c = \nabla_0^s \vec{u} \quad \text{on } S_0, \quad (4.42)$$

$$\vec{p}^{(n)} = -[\vec{m} \cdot \boldsymbol{\mu}^c] \quad \text{on } \ell_0^{(n)}, \quad (4.43)$$

$$[\vec{N} \cdot (\mathbf{P}^c - \boldsymbol{\lambda}^c)] = \vec{0} \quad \text{on } S_0^{t,int}, \quad (4.44)$$

$$[\vec{N} \cdot \mathbf{Q}] = \mathbf{0} \quad \text{on } S_0^{r,int}. \quad (4.45)$$

The above system constitutes the strong form of the equilibrium problem for a second gradient continuum with kinematic constraints (4.38) and (4.42) and Lagrange multipliers identified according to the relations (4.37) and (4.41). The interior continuity conditions (4.44) and (4.45) are not a part of the strong form (4.20)-(4.23), unless physical internal boundaries, e.g. material interfaces, are present. These interior continuity conditions became a part of (4.36)-(4.45) due to the choice of C^0 continuity for the trial and weighting functions. For smooth trial and weighting functions, the weak form implies only the equilibrium equation, the traction and double traction boundary conditions.

Assuming satisfaction of (4.38) in the volume in an averaged sense, ensures that the surface integral in the left-hand side of (4.26) is negligible, which allows to rewrite the weak form as

$$\begin{aligned} & \int_{V_0} \left\{ \mathbf{P} : \delta \mathbf{F}^c + \mathbf{Q} : \delta \hat{\mathbf{G}} + \delta (\boldsymbol{\lambda} : (\hat{\mathbf{F}}^c - \mathbf{F}^c)) \right\} dV_0 \\ &= \int_{V_0} \vec{b} \cdot \delta \vec{u} dV_0 + \int_{S_0} \vec{t} \cdot \delta \vec{u} dS_0 + \int_{S_0} \mathbf{R} : \delta \hat{\mathbf{F}}^c dS_0 + \sum_n \oint_{\ell_0^{(n)}} \vec{p}^{(n)} \cdot \delta \vec{u} d\ell_0^{(n)}, \end{aligned} \quad (4.46)$$

which for a sufficiently fine mesh does not introduce a significant error, while simplifying the finite element implementation. The same assumption has also been made by other authors (Shu et al. (1999); Matsushima et al. (2002)). However, in Amanatidou and Aravas (2002) the surface integral term has been retained.

In order to correctly formulate a boundary value problem for a smooth second gradient continuum body, six independent boundary conditions are required for a three-dimensional problem (four independent boundary conditions for a two-dimensional problem). A way to prescribe the boundary conditions associated with the primary unknown fields \vec{u} and $\hat{\mathbf{F}}$ has been addressed in Shu et al. (1999). Let a superscript $*$ indicate a prescribed quantity on the surface. If the stress traction \vec{t}^* and the double stress traction \vec{r}^* are given, the boundary conditions to be prescribed are simply

$$\vec{t} = \vec{t}^* \quad \text{and} \quad \mathbf{R} = \vec{r}^* \vec{N}. \quad (4.47)$$

If the displacement \vec{u}^* and the displacement gradient normal to the surface $(D_0\vec{u})^*$ are given, the boundary conditions are prescribed as

$$\vec{u} = \vec{u}^* \quad \text{and} \quad \hat{\mathbf{F}}^c = \vec{N}(D_0\vec{u})^* + \nabla_0^s \vec{u}^*, \quad (4.48)$$

where the surface gradient $\nabla_0^s \vec{u}^*$ is known because the displacement \vec{u}^* is given on the surface. Using these boundary conditions no error is introduced in (4.46) due to neglecting the boundary integral term in (4.26), since in this case the constraint $\hat{\mathbf{F}}_s^c = \nabla_0^s \vec{u}^*$ is automatically satisfied by (4.48). Mixed boundary conditions are obtained by combination of the dynamic and kinematic boundary conditions (4.47) and (4.48).

4.3.2 Finite element discretization

The higher-order equilibrium formulation is now discretized using finite elements. The body of interest is subdivided into N_{elem} elements with a total number of K_x , K_F and K_λ nodes for the three unknown fields describing the deformed position vector \vec{x} , the relaxed deformation gradient $\hat{\mathbf{F}}$ and the Lagrange multiplier λ , respectively. The finite element approximations for these unknown fields are written as

$$\vec{x} = \sum_{A=1}^{K_x} N_A^x \vec{x}_A \equiv N_A^x \vec{x}_A, \quad (4.49)$$

$$\hat{\mathbf{F}} = \sum_{A=1}^{K_F} N_A^F \hat{\mathbf{F}}_A \equiv N_A^F \hat{\mathbf{F}}_A, \quad (4.50)$$

$$\lambda = \sum_{A=1}^{K_\lambda} N_A^\lambda \lambda_A \equiv N_A^\lambda \lambda_A, \quad (4.51)$$

where N^x and N^F are C^0 continuous interpolants for the position vector and relaxed deformation gradient fields, respectively, and N^λ are C^{-1} continuous interpolants for the Lagrange multiplier field.

Here and in the following capital Latin subscripts indicate a nodal quantity, while small Latin subscripts will refer to components of vectors and tensors. Summation over repeated indices is implied in both cases. The range of the capital Latin letters is over all the nodes (of the mesh or the element, depending on the context); the range of the small Latin letters equals the number of dimensions of the configuration.

Following the standard Galerkin approach the interpolants N^x , N^F and N^λ are also used for the respective weighting functions

$$\delta \vec{x} = \delta \vec{u} = N_A^x \delta \vec{u}_A, \quad \delta \hat{\mathbf{F}} = N_A^F \delta \hat{\mathbf{F}}_A, \quad \delta \lambda = N_A^\lambda \delta \lambda_A. \quad (4.52)$$

The discrete approximations to the gradient relations (4.27) and (4.28) are

$$\mathbf{F} = \vec{x}_A \vec{B}_A^x, \quad \text{with} \quad \vec{B}_A^x = \frac{\partial N_A^x}{\partial \vec{X}}, \quad (4.53)$$

$${}^3\hat{\mathbf{G}} = \vec{B}_A^F \hat{\mathbf{F}}_A, \quad \text{with} \quad \vec{B}_A^F \quad \text{defined such that} \quad \hat{G}_{ijk} = \frac{1}{2} \left(\frac{\partial N_A^F}{\partial X_i} \hat{F}_{Aj k} + \frac{\partial N_A^F}{\partial X_k} \hat{F}_{A j i} \right). \quad (4.54)$$

Substitution of (4.49)-(4.54) into the weak form (4.46) (assuming for simplicity that the body has a smooth surface, so that the line integral vanishes) leads to

$$\begin{aligned} & \int_{V_0} \left\{ \mathbf{P} : \vec{B}_A^x \delta \vec{u}_A + {}^3\mathbf{Q} : \vec{B}_A^F \delta \hat{\mathbf{F}}_A \right\} dV_0 \\ & + \int_{V_0} \left\{ N_A^\lambda \delta \lambda_A : (N_B^F \hat{\mathbf{F}}_B^c - \vec{B}_B^x \vec{x}_B) + N_B^\lambda \lambda_B : (N_A^F \delta \hat{\mathbf{F}}_A^c - \vec{B}_A^x \delta \vec{u}_A) \right\} dV_0 \\ & = \int_{V_0} \vec{b} \cdot N_A^x \delta \vec{u}_A dV_0 + \int_{S_0} \vec{t} \cdot N_A^x \delta \vec{u}_A dS_0 + \int_{S_0} \mathbf{R} : N_A^F \delta \hat{\mathbf{F}}_A^c dS_0. \end{aligned} \quad (4.55)$$

Taking into account that the above equation must be satisfied for arbitrary weighting parameters $\delta \vec{u}_A$, $\delta \hat{\mathbf{F}}_A$ and $\delta \lambda_A$ results in a system of equations constituting the discrete force balances and additionally the discretized kinematic constraint

$$\int_{V_0} \mathbf{P} \cdot \vec{B}_A^x dV_0 + \lambda_B \cdot \vec{C}_{AB} = \int_{V_0} \vec{b} N_A^x dV_0 + \int_{S_0} \vec{t} N_A^x dS_0, \quad (4.56)$$

$$\int_{V_0} {}^3\mathbf{Q} \cdot \vec{B}_A^F dV_0 + \lambda_B^c E_{AB} = \int_{S_0} \mathbf{R}^c N_A^F dS_0, \quad (4.57)$$

$$\vec{C}_{BA} \vec{x}_B + E_{BA} \hat{\mathbf{F}}_B^c = \mathbf{0}, \quad (4.58)$$

where the following notation has been introduced

$$\vec{C}_{AB} = - \int_{V_0} \vec{B}_A^x N_B^\lambda dV_0, \quad E_{AB} = \int_{V_0} N_A^F N_B^\lambda dV_0. \quad (4.59)$$

The left-hand side of every equation in the system (4.56)-(4.58) represents the internal contribution. They must balance the external contributions present in the right-hand side of the system.

4.3.3 Iterative procedure

Due to the presence of geometrical and/or material non-linearities the system of equations (4.56)-(4.58) is generally non-linear. This means that the solution of this set of equations must be determined iteratively. A Newton-Raphson procedure is used for this purpose. The system of equations is linearized in each iteration with respect to the solution estimate obtained in the previous iteration. Solving the linearized system yields an iterative correction to the previous estimate. This process is repeated until some appropriate convergence criterion is satisfied. Thus, for the system (4.56)-(4.58) the solution estimate at iteration $i + 1$ is written as

$$\vec{x}^{(i+1)} = \vec{x}^{(i)} + \Delta \vec{x}, \quad (4.60)$$

$$\hat{\mathbf{F}}^{(i+1)} = \hat{\mathbf{F}}^{(i)} + \Delta \hat{\mathbf{F}}, \quad (4.61)$$

$$\lambda^{(i+1)} = \lambda^{(i)} + \Delta \lambda, \quad (4.62)$$

where $\Delta \vec{x}$, $\Delta \hat{\mathbf{F}}$ and $\Delta \lambda$ denote iterative corrections for the respective unknowns. Application to the stress and higher-order stress tensors gives

$$\mathbf{P}^{(i+1)} = \mathbf{P}^{(i)} + \Delta \mathbf{P}, \quad (4.63)$$

$${}^3\mathbf{Q}^{(i+1)} = {}^3\mathbf{Q}^{(i)} + \Delta {}^3\mathbf{Q}, \quad (4.64)$$

with iterative corrections $\Delta\mathbf{P}$ and $\Delta^3\mathbf{Q}$. Consistent linearization of the constitutive relations (4.24) and (4.25) leads to

$$\Delta\mathbf{P} = {}^4\mathbf{C}^{(1)} : \Delta\mathbf{F}^c + {}^5\mathbf{C}^{(2)} : \Delta^3\hat{\mathbf{G}}^{RC}, \quad (4.65)$$

$$\Delta^3\mathbf{Q} = {}^5\mathbf{C}^{(3)} : \Delta\mathbf{F}^c + {}^6\mathbf{C}^{(4)} : \Delta^3\hat{\mathbf{G}}^{RC}, \quad (4.66)$$

where $\Delta\mathbf{F}$ and $\Delta^3\hat{\mathbf{G}}$ are calculated from the iterative corrections $\Delta\vec{x}$ and $\Delta\hat{\mathbf{F}}$, respectively. In (4.65) and (4.66) the fourth-order tensor ${}^4\mathbf{C}^{(1)}$, the fifth-order tensors ${}^5\mathbf{C}^{(2)}$ and ${}^5\mathbf{C}^{(3)}$ and the sixth-order tensor ${}^6\mathbf{C}^{(4)}$ are the consistent tangent stiffnesses; the superscript *RC* indicates right conjugation, which for a third-order tensor ${}^3\mathbf{T}$ is defined as $T_{ijk}^{RC} = T_{ikj}$. When an explicit form of the constitutive relations (4.24) and (4.25) is specified, the consistent constitutive tangents can be obtained analytically or numerically. In section 4.4.1 a simple example will be given for an elastic Mindlin model. In case of computational homogenization the constitutive tangents are obtained numerically, based on the microstructural behaviour (see section 3.5.3). Examples of constitutive tangents for other higher-order constitutive models may be found in Shu and Fleck (1999) for small deformation rate dependent strain-gradient crystal plasticity, in Shu and Barlow (2000) for large deformation strain-gradient crystal plasticity, and in Zervos et al. (2001) and Matsushima et al. (2002) for different types of continuum strain-gradient elasto-plastic models.

Substitution of (4.60)-(4.66) into (4.56)-(4.58) leads, after linearization, to a linear system of equations

$$\begin{bmatrix} \underline{K} & \underline{L} & \underline{C} \\ \underline{M} & \underline{T} & \underline{E} \\ \underline{C}^T & \underline{E}^T & \underline{Q} \end{bmatrix} \begin{bmatrix} \Delta\vec{u} \\ \Delta\hat{\mathbf{F}} \\ \Delta\vec{\lambda} \end{bmatrix} = \begin{bmatrix} \underline{f}_{x,ext} - \underline{f}_{x,int}^{(i)} \\ \underline{f}_{F,ext} - \underline{f}_{F,int}^{(i)} \\ -\underline{f}_{\lambda,int}^{(i)} \end{bmatrix}, \quad (4.67)$$

where $\Delta\vec{u}$, $\Delta\hat{\mathbf{F}}$ and $\Delta\vec{\lambda}$ are the columns with iterative corrections to the components of the nodal unknowns. Matrices \underline{K} , \underline{L} , \underline{M} and \underline{T} are the matrix representations of the following tensors

$$\begin{aligned} K_{ijAB} &= \int_{V_0} B_{mA}^x C_{imjn}^{(1)} B_{nB}^x dV_0, & L_{ijkAB} &= \int_{V_0} B_{mA}^x C_{imjkn}^{(2)} B_{nB}^F dV_0, \\ M_{ijkAB} &= \int_{V_0} B_{mA}^F C_{ijmkn}^{(3)} B_{nB}^x dV_0, & T_{ijklAB} &= \int_{V_0} B_{mA}^F C_{ijmkl n}^{(4)} B_{nB}^F dV_0, \end{aligned} \quad (4.68)$$

\underline{C} and \underline{E} are matrix representations of (4.59); \underline{Q} is a zero matrix of the appropriate size; $\underline{f}_{x,int}^{(i)}$, $\underline{f}_{F,int}^{(i)}$, $\underline{f}_{\lambda,int}^{(i)}$, $\underline{f}_{x,ext}$ and $\underline{f}_{F,ext}$ are column representations of the following vector and tensor expressions

$$\vec{f}_{x,int A}^{(i)} = \int_{V_0} \mathbf{P}^{(i)} \cdot \vec{B}_A^x dV_0 + \boldsymbol{\lambda}_B^{(i)} \cdot \vec{C}_{AB}, \quad (4.69)$$

$$\mathbf{f}_{F,int A}^{(i)} = \int_{V_0} {}^3\mathbf{Q}^{(i)} \cdot \vec{B}_A^F dV_0 + \boldsymbol{\lambda}_B^c{}^{(i)} E_{AB}, \quad (4.70)$$

$$\mathbf{f}_{\lambda,int A}^{(i)} = \vec{C}_{BA} \vec{x}_B^{(i)} + E_{BA} \hat{\mathbf{F}}_B^c{}^{(i)}, \quad (4.71)$$

$$\vec{f}_{x,ext A} = \int_{V_0} \vec{b} N_A^x dV_0 + \int_{S_0} \vec{t} N_A^x dS_0, \quad \mathbf{f}_{F,ext A} = \int_{S_0} \mathbf{R}^c N_A^F dS_0. \quad (4.72)$$

Solving the set of linear equations (4.67) gives the corrections $\Delta \underline{u}$, $\Delta \hat{\underline{F}}$ and $\Delta \underline{\lambda}$, which can be used to update the nodal unknowns according to (4.60)-(4.62). The linear system can then be reassembled and solved for a new iteration step. This process is repeated until convergence has been achieved.

The total number of scalar unknowns in system (4.67) in the 2D case is equal to $2K_x + 4K_F + 4K_\lambda$, with K_x , K_F and K_λ the number of nodes in the mesh for the respective unknowns. This is significantly larger than for the standard displacement-based finite element formulation for a classical continuum. However, taking advantage of the weaker continuity requirements on the Lagrange multiplier λ , allows to define λ at element level such that elimination can be performed before assembly. This reduces the total number of unknowns in the assembled system of equations by $4K_\lambda^e N_{\text{elem}}$, with K_λ^e number of Lagrange multiplier nodes per element.

This elimination, however, cannot be performed directly from the element analogy of system (4.67). Therefore, a penalized form of the system has to be used

$$\begin{bmatrix} \underline{K}_e & \underline{L}_e & \underline{C}_e \\ \underline{M}_e & \underline{T}_e & \underline{E}_e \\ \underline{C}_e^T & \underline{E}_e^T & \underline{H}_e \end{bmatrix} \begin{bmatrix} \Delta \underline{u}_e \\ \Delta \hat{\underline{F}}_e \\ \Delta \underline{\lambda}_e \end{bmatrix} = \begin{bmatrix} \underline{f}_{x,ext_e} - \underline{f}_{x,int_e}^{(i)} \\ \underline{f}_{F,ext_e} - \underline{f}_{F,int_e}^{(i)} \\ - \underline{f}_{\lambda,int_e}^{(i)} \end{bmatrix}, \quad (4.73)$$

where $\Delta \underline{u}_e$, $\Delta \hat{\underline{F}}_e$ and $\Delta \underline{\lambda}_e$ are element unknowns, \underline{K}_e , \underline{L}_e , \underline{M}_e , \underline{T}_e , \underline{C}_e , \underline{E}_e are element counterparts of the global matrices defined above, and \underline{H}_e is a matrix composed of

$$H_{ABe} = \frac{1}{\alpha} \int_{V_{0e}} N_A^\lambda N_B^\lambda dV_0, \quad (4.74)$$

where α is a penalty parameter. The penalized system (4.73) can also be obtained directly from a perturbed Lagrangian form of the weak statement (4.46)

$$\begin{aligned} & \int_{V_0} \left\{ \mathbf{P} : \delta \mathbf{F}^c + {}^3\mathbf{Q} : \delta {}^3\hat{\mathbf{G}} + \delta \left(\boldsymbol{\lambda} : (\hat{\mathbf{F}}^c - \mathbf{F}^c) \right) + \frac{1}{\alpha} \boldsymbol{\lambda} : \delta \boldsymbol{\lambda}^c \right\} dV_0 \\ & = \int_{V_0} \vec{b} \cdot \delta \vec{u} dV_0 + \int_{S_0} \vec{t} \cdot \delta \vec{u} dS_0 + \int_{S_0} \mathbf{R} : \delta \hat{\mathbf{F}}^c dS_0 + \sum_n \oint_{\ell_0^{(n)}} \vec{p}^{(n)} \cdot \delta \vec{u} d\ell_0. \end{aligned} \quad (4.75)$$

Elimination of $\Delta \underline{\lambda}_e$ from system (4.73) gives

$$\begin{bmatrix} \underline{K}_e - \underline{C}_e \underline{H}_e^{-1} \underline{C}_e^T & \underline{L}_e - \underline{C}_e \underline{H}_e^{-1} \underline{E}_e^T \\ \underline{M}_e - \underline{E}_e \underline{H}_e^{-1} \underline{C}_e^T & \underline{T}_e - \underline{E}_e \underline{H}_e^{-1} \underline{E}_e^T \end{bmatrix} \begin{bmatrix} \Delta \underline{u}_e \\ \Delta \hat{\underline{F}}_e \end{bmatrix} = \begin{bmatrix} \underline{f}_{x,ext_e} - \underline{f}_{x,int_e}^{(i)} \\ \underline{f}_{F,ext_e} - \underline{f}_{F,int_e}^{(i)} \end{bmatrix}, \quad (4.76)$$

where

$$\underline{f}_{x,int_e}^{(i)} = \int_{V_{0e}} \underline{B}^x \underline{P}^{(i)} dV_0 - \underline{C}_e \underline{H}_e^{-1} \left(\underline{C}_e^T \underline{x}_e^{(i)} + \underline{E}_e^T \hat{\underline{F}}_e^{(i)} \right), \quad (4.77)$$

$$\underline{f}_{F,int_e}^{(i)} = \int_{V_{0e}} \underline{B}^F \underline{Q}^{(i)} dV_0 - \underline{E}_e \underline{H}_e^{-1} \left(\underline{C}_e^T \underline{x}_e^{(i)} + \underline{E}_e^T \hat{\underline{F}}_e^{(i)} \right), \quad (4.78)$$

with $\underline{P}^{(i)}$ and $\underline{Q}^{(i)}$ denoting columns with the components of the stress tensor and the higher-order stress tensor; \underline{B}^x and \underline{B}^F are matrix representations of the material derivatives of the shape functions (4.53) and (4.54). Assembly of the element contributions (4.76) leads to a global system of equations in the unknowns $\Delta \underline{u}$ and $\Delta \hat{\underline{F}}$ only.

As usual for large deformation problems, the external load is applied in a number of loading steps (increments). It is also worth mentioning that in the previous derivations the total Lagrangian formulation has been adopted, i.e. all the derivatives and integrals are taken with respect to the Lagrangian (material) coordinates \vec{X} . The same theory can also be formulated in terms of an updated Lagrangian procedure, as has been presented by Shu and Barlow (2000) and Matsushima et al. (2002). The updated Lagrangian formulation has an advantage over the total Lagrangian formulation when implementing rate-type constitutive models. However, the actual implementation has been developed for use in the context of a computational homogenization scheme, where the stress updates and the consistent tangents are obtained numerically from the microstructural analysis. As demonstrated in the previous chapters this can be done easier in a total Lagrangian framework.

4.3.4 Finite elements

In the following the attention is restricted to two-dimensional and plane strain problems only. Implementation of plane stress problems requires additional developments, since in this case gradients in the out-of-plane direction have to be taken into account (Chen et al. (2000)). Six two-dimensional isoparametric elements, which are sketched in Figure 4.1, have been developed and implemented. The quadrilateral elements, eight and nine noded as far as displacement degrees of freedom are concerned, differ in the number and the position of their nodes with the degrees of freedom corresponding to the displacements u_1 and u_2 , relaxed deformation gradient components \hat{F}_{11} , \hat{F}_{22} , \hat{F}_{12} and \hat{F}_{21} and Lagrange multipliers λ_{11} , λ_{22} , λ_{12} and λ_{21} . The elements are denoted by a leading letter Q (for quadrilateral) followed by the number of displacement nodes, deformation gradient nodes and Lagrange multiplier nodes, e.g. element QU8F4L4 has 8 displacement nodes, 4 deformation gradient nodes and 4 Lagrange multiplier nodes.

Elements with nine displacement nodes (QU9F4L4, QU9F4L1, QU9F9L4) use the standard biquadratic Lagrangian shape functions for the interpolation of the displacement degrees of freedom; the eight displacement node elements (QU8F4L4, QU8F4L1, QU8F8L4) are based on the conventional quadratic serendipity shape functions. The relaxed deformation gradient degrees of freedom are interpolated bilinearly for elements with four deformation gradient nodes located at the corner nodes (elements QU9F4L4, QU9F4L1, QU8F4L4, QU8F4L1); elements QU9F9L4 and QU8F8L4 use for the deformation gradient the biquadratic and serendipity shape functions, respectively. In the elements QU9F4L4, QU9F9L4, QU8F4L4 and QU8F8L4 the Lagrange multiplier is interpolated bilinearly between the nodal values given at the 2×2 Gauss quadrature points; in the elements QU9F4L1 and QU8F4L1 the Lagrange multiplier is assumed to be constant within the element and evaluated in one node located at the center of the element. It should also be mentioned that the nine noded elements (QU9F4L4, QU9F4L1, QU9F9L4) have been originally presented by Shu et al. (1999), who have additionally developed similar triangular elements. The eight noded element QU8F4L1 has been used by Matsushima et al. (2002). Amanatidou and Aravas (2002) have proposed an element similar to QU9F9L4, but with a continuous approximation for the Lagrange

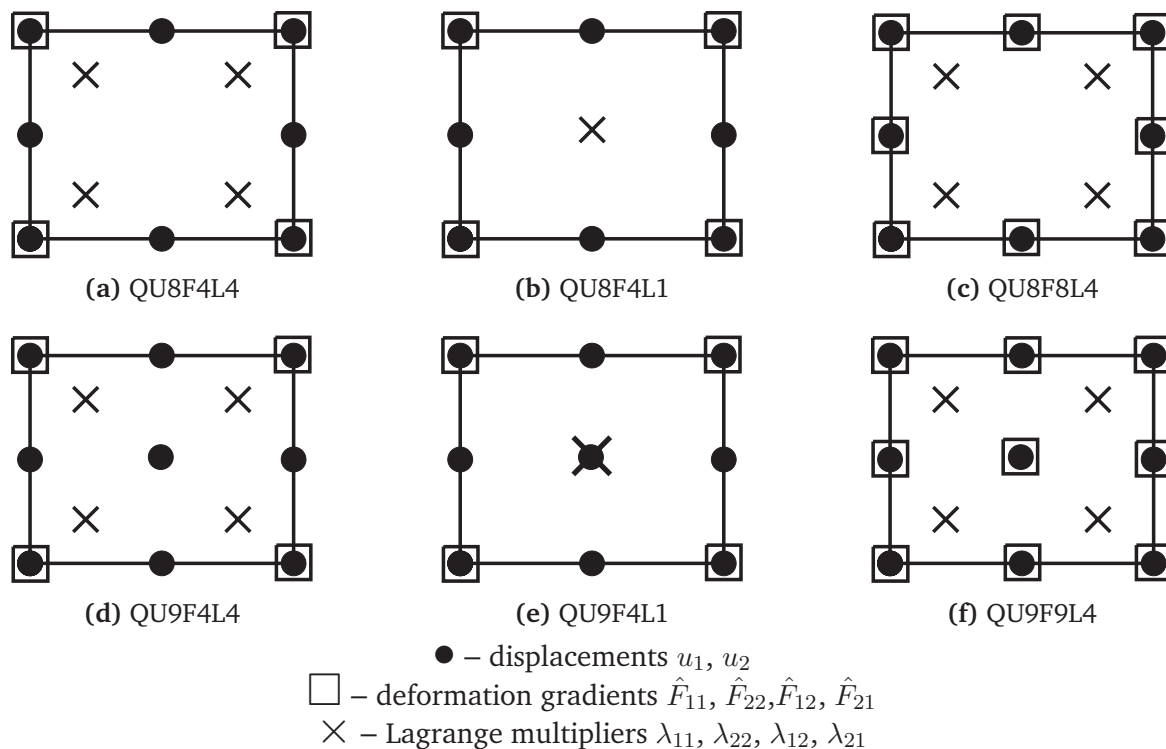


Figure 4.1: Finite elements for the second gradient continuum formulation.

multiplier.

4.4 Validation and choice of elements

In this section the finite element implementation of the second gradient continuum formulation is tested and the performance of the elements developed is evaluated and compared. First Mindlin’s elastic constitutive model is briefly summarized. This simple elastic model has been implemented and used for testing purposes. The patch test is used to check the completeness and stability properties of the elements. After that, the accuracy and convergence of the elements is examined by comparing numerical results with the analytical solution for a boundary shear layer problem.

4.4.1 Mindlin elastic constitutive model

Mindlin has developed a constitutive model for an isotropic linearly hyper-elastic second gradient solid, see Mindlin (1964); Mindlin and Eshel (1968). In the present work a simple extension of this linear model to account for geometrical non-linearities is used. The resulting constitutive model is geometrically non-linear, but physically linear. Not accounting for material non-linearities in case of large deformations and large gradients of deformation may be an unrealistic approximation to physical phenomena, but suffices for testing purposes. In the context of the second-order computational homogenization (next chapter) the macroscopic material behavior will be obtained from the microstructural response and includes both material and geometrical non-linearities.

The elastic strain energy per unit reference volume is expressed as

$$\begin{aligned} W_0 = & \frac{1}{2}\lambda E_{ii}E_{jj} + \mu E_{ij}E_{ij} \\ & + \frac{1}{2}a_1(G_{ijj}G_{ikk} + G_{jji}G_{kki}) + \frac{1}{2}a_2(G_{iki}G_{kjj} + G_{iki}G_{jjk}) + a_3G_{iki}G_{jjk} \\ & + a_4G_{ikj}G_{ikj} + \frac{1}{2}a_5(G_{ijk}G_{jik} + G_{ijk}G_{jki}), \end{aligned} \quad (4.79)$$

where \mathbf{E} is the Green-Lagrange strain tensor $\mathbf{E} = \frac{1}{2}(\mathbf{F}^c \cdot \mathbf{F} - \mathbf{I})$. The material parameters involved in (4.79) are the standard Lamé constants λ and μ and five additional constants a_i , $i = \overline{1,5}$ of dimension stress times length squared. In the present implementation these higher-order constitutive parameters were taken $a_1 = a_2 = a_3 = a_4 = a_5 = 0.5\mu\ell^2$, with ℓ a material length scale parameter. The first Piola-Kirchhoff stress tensor and the higher-order stress tensor are given by

$$\mathbf{P} = \frac{\partial W_0}{\partial \mathbf{F}} = \mathbf{F} \cdot \frac{\partial W_0}{\partial \mathbf{E}} = \mathbf{F} \cdot \mathbf{S} = \mathbf{F} \cdot (\lambda I_1(\mathbf{E})\mathbf{I} + 2\mu\mathbf{E}) = \mathbf{F} \cdot {}^4\mathbf{C} : \mathbf{E}, \quad (4.80)$$

$$\begin{aligned} {}^3\mathbf{Q} = \frac{\partial W_0}{\partial {}^3\mathbf{G}} = & a_1({}^3\mathbf{G} : \mathbf{II} + \mathbf{II} : {}^3\mathbf{G}) + \frac{1}{2}a_2({}^3\mathbf{G}^{LC} : \mathbf{II} + 2({}^3\mathbf{G} : \mathbf{II})^{LC} + \mathbf{II} : {}^3\mathbf{G}^{RC}) \\ & + 2a_3({}^3\mathbf{G}^{LC} : \mathbf{II})^{LC} + 2a_4{}^3\mathbf{G} + a_5({}^3\mathbf{G}^{LC} + ({}^3\mathbf{G}^{LC})^{RC}) = {}^6\mathbf{D} : {}^3\mathbf{G}^{RC} \end{aligned} \quad (4.81)$$

where \mathbf{S} is the second Piola-Kirchhoff stress tensor; $I_1(\mathbf{E})$ denotes the first invariant of \mathbf{E} ; ${}^4\mathbf{C}$ and ${}^6\mathbf{D}$ are tensors with material constants. Linearization of these constitutive relations is a straightforward operation

$$\delta \mathbf{P} = ({}^4\mathbf{I}^{RC} \cdot \mathbf{S} + \mathbf{F} \cdot {}^4\mathbf{C} : {}^4\mathbf{A}) : \delta \mathbf{F}^c, \quad (4.82)$$

$$\delta {}^3\mathbf{Q} = {}^6\mathbf{D} : \delta {}^3\mathbf{G}^{RC}, \quad (4.83)$$

with the components of the fourth-order unit tensor ${}^4\mathbf{I}$ defined in terms of the Kronecker delta as $I_{ijkl} = \delta_{il}\delta_{jk}$; the fourth-order tensor ${}^4\mathbf{A}$ is defined such that $\delta \mathbf{E} = {}^4\mathbf{A} : \delta \mathbf{F}^c$.

4.4.2 Patch test

The patch test has proven to be a valuable test for consistency and stability, which are the well-known necessary and sufficient conditions for convergence of a finite element formulation. The methodology of the patch test is well-established and summarized in many text books on finite elements (e.g. Zienkiewicz and Taylor (2000); Belytschko et al. (2000), see also research publications by Zienkiewicz and Taylor (1997); Zhang and Chen (1997); Dvorkin (2001)).

In order to check the stability of a mixed formulation, a rather complex mathematical inf-sup criterion (better known in the literature as the BB condition) has been formulated (Babuška (1973); Brezzi and Bathe (1990)). However, a very simple constraint count provides a necessary condition for stability of a mixed form and can immediately indicate elements that will fail, and others that may perform satisfactorily but require further testing, Zienkiewicz and Taylor (2000, 1997). This condition states that in the system of equations with all the boundary conditions enforced, the number of constraint unknowns (Lagrange multipliers) should not exceed the number of primary unknowns. Thus, in the context of the mixed formulation for the second gradient continuum developed above, this condition reads

$$n_u + n_F \geq n_\lambda, \quad (4.84)$$

where n_u , n_F and n_λ are the numbers of remaining (after application of the boundary conditions) degrees of freedom corresponding to \vec{u} , $\hat{\mathbf{F}}$ and $\boldsymbol{\lambda}$, respectively. Condition (4.84) is necessary for solvability, if it is not satisfied, the patch test fails. If (4.84) is satisfied, further tests should be performed to ensure that no zero eigenvalues of the global stiffness matrix are present.

Condition (4.84) has been checked for the six elements proposed (see Figure 4.1). Table 4.1 summarizes the results for the count test on an infinite patch.

Table 4.1: Count test. Number of primary unknowns $n_u + n_F$ vs. number of Lagrange multipliers n_λ per element in an infinite 2D patch.

element	$n_u + n_F$	n_λ	result
QU8F4L4	10	16	fail
QU8F4L1	10	4	pass
QU8F8L4	18	16	pass
QU9F4L4	12	16	fail
QU9F4L1	12	4	pass
QU9F9L4	24	16	pass

As can be seen from Table 4.1 the elements QU8F4L4 and QU9F4L4 fail the count test. Element QU8F8L4 passes the test marginally. Although it does pass the count test on an infinite patch, for many finite patches it will not pass the test. Therefore, the elements QU8F4L4 and QU9F4L4 (and, in general, QU8F8L4) should be excluded from further examinations, but nevertheless they are retained for generality. An additional stability analysis of the elements that pass the count test shows that these elements provide a non-singular matrix when integrated using a 3×3 integration point scheme. However, when using 2×2 Gauss quadrature points for numerical integration, the nine displacement node elements exhibit zero energy modes (just as it is the case for a classical continuum). The eight displacement node element QU8F4L1 has been used successfully with 2×2 integration points.

The second part of the patch test is a consistency check. In this test the patch of elements depicted in Figure 4.2 has been used. The linear reproduction condition, i.e. the ability of an element to reproduce (bi)linear displacement and constant deformation (and stress) fields, is checked by prescribing displacements of all the nodes on the boundary according to a linear polynomial. The patch test is passed if the finite element solution for displacements throughout the patch is given by the same polynomial. The strains should be constant and given by the application of the strain-displacement relations to the prescribed polynomial. All the elements developed pass this linear patch test.

For elements constructed for a classical continuum usually only the linear patch test needs to be satisfied. For the elements developed for the second gradient formulation it may be useful to perform a quadratic patch test, i.e. to check the ability of an element to reproduce a (bi)quadratic displacement, linear deformation and constant gradient of the deformation field. For this test the same patch configuration has been used (see Figure 4.2). Displacement and relaxed deformation gradient degrees of freedom of the boundary nodes have been prescribed according to a quadratic polynomial and its gradient, respectively. It is also remarked that an arbitrary quadratic displacement field will generally not satisfy equilibrium (4.20) in the absence of body forces. Therefore

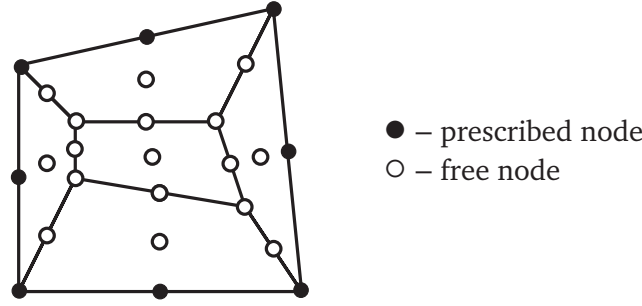


Figure 4.2: The finite element mesh for the patch test.

in the case of a quadratic patch test, special action should be taken to prescribe body forces in such a way that equilibrium is satisfied.

For an element size in the patch smaller than the material length scale ℓ involved in the second gradient constitutive model, element QU9F9L4 reproduces the quadratic displacement field (and the fields of its derivatives) exactly. For element sizes larger than ℓ , the solution is approximated with an error, which reduces upon reduction of the element size. Elements QU8F4L1 and QU9F4L1 reproduce a quadratic displacement field (and the fields of its derivatives) with a slight error even for element sizes smaller than ℓ . This error, however, is within accuracy limits acceptable for most applications. Therefore, combined with the fact that these two elements have roughly twice less degrees of freedom than the element QU9F9L4, elements QU8F4L1 and QU9F4L1 are considered to be good candidates for the solution of practical problems. The other elements do not pass the quadratic patch test, these, however, are the same elements that did not pass the count test.

4.4.3 Boundary shear layer problem

In this section the performance of the finite elements developed is evaluated and compared on the basis of a boundary shear layer problem.

Plane strain shear of a two-dimensional strip with height H in the X_2 direction and “infinite” in the X_1 direction, is considered, see Figure 4.3.

The boundary conditions are

$$\begin{aligned} u_1 = 0, \quad u_2 = 0, \quad F_{12} = 0, \quad F_{22} = 1 & \quad \text{on} \quad X_2 = 0 \\ u_1 = U^*, \quad u_2 = 0, \quad F_{12} = 0, \quad F_{22} = 1 & \quad \text{on} \quad X_2 = H. \end{aligned} \quad (4.85)$$

For this simple shear boundary value problem all field quantities are independent of X_1 . Neglecting displacement u_2 (which generally will be non-zero in a higher-order formulation), the only non-vanishing deformation gradient component is $F_{12} \equiv \gamma(X_2)$ and its gradient $G_{212} = \partial\gamma/\partial X_2$. Adopting Mindlin’s elastic model (see section 4.4.1) for the material behaviour, with shear modulus μ , and the higher-order constitutive parameters $a_1 = a_2 = a_3 = a_4 = a_5 = 0.5\mu\ell^2$, with ℓ the material length scale, the non-zero stress and higher-order stress components are

$$\begin{aligned} P_{11} = \mu\gamma^2, \quad P_{12} = P_{21} = \mu\gamma, \quad Q_{111} = \frac{3}{2}\mu\ell^2 G_{212}, \\ Q_{122} = Q_{221} = \frac{3}{4}\mu\ell^2 G_{212}, \quad Q_{212} = 2\mu\ell^2 G_{212}. \end{aligned} \quad (4.86)$$

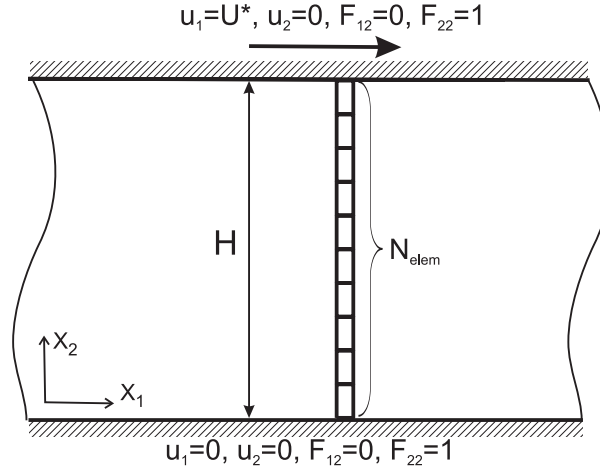


Figure 4.3: Geometry, boundary conditions and finite element mesh for the boundary shear layer problem.

Substitution of (4.86) into the higher-order equilibrium equation (4.20) while accounting for the boundary conditions (4.85) yields the following solution for the displacement

$$u_1 = \frac{U^*}{A} \left\{ -1 + \cosh\left(\frac{H}{\hat{\ell}}\right) - \frac{X_2}{\hat{\ell}} \sinh\left(\frac{H}{\hat{\ell}}\right) + \cosh\left(\frac{X_2}{\hat{\ell}}\right) - \cosh\left(\frac{H - X_2}{\hat{\ell}}\right) \right\}, \quad (4.87)$$

$$\text{with } A = -2 + 2 \cosh(H/\hat{\ell}) - H/\hat{\ell} \sinh(H/\hat{\ell}), \quad \hat{\ell} = \sqrt{2}\ell.$$

The distribution of the shear along the height of the strip can easily be obtained by differentiation of (4.87) with respect to X_2 . Note that no assumption on small strains has been made, so (4.87) is also valid for large values of the average shear $\gamma^* = U^*/H$. Using the formulas (4.21) and (4.22) the non-vanishing components of the traction t_1 and the double traction r_1 on the surface $X_2 = H$ are obtained as

$$t_1 = -\mu \frac{U^*}{\hat{\ell} A} \sinh\left(\frac{H}{\hat{\ell}}\right), \quad (4.88)$$

$$r_1 = \mu \frac{U^*}{A} \left(\cosh\left(\frac{H}{\hat{\ell}}\right) - 1 \right). \quad (4.89)$$

In the following the analytical solution for the boundary shear layer problem is used to validate the developed higher-order finite element code and to examine the ability of the finite elements constructed in section 4.3.4 to predict the analytical results. In Figure 4.3 the finite element mesh used in the calculations is sketched. The mesh consists of a column of quadrilateral elements. In height direction the layer H is discretized into N_{elem} identical elements. In the present analysis, meshes with $N_{\text{elem}} = 3, 5, 10, 20$ elements have been used. The boundary conditions on the top and bottom edges of the layer are prescribed according to (4.85) with the derivatives of the displacements written in terms of the components of the relaxed deformation gradient tensor $\hat{\mathbf{F}}$. In order to enforce uniformity in the X_1 direction, periodic boundary conditions on every nodal degree of freedom are applied along the left and right sides of the mesh. The condition $u_2 = 0$ is prescribed on the left and right boundary nodes. The material and geometrical parameters used in these test calculations are the shear modulus $\mu = 2000$ MPa, the bulk

modulus $K = 5000$ MPa, the material length scale $\ell = 0.05$ mm, the height of the layer $H = 1$ mm and a prescribed displacement $U^* = 0.03$ mm.

The model problem has been solved numerically using all six types of elements introduced in section 4.3.4. Figure 4.4 shows the distribution of the shear component of the deformation gradient tensor along the height of the layer. Convergence of the numerical solution towards the analytical solution upon mesh refinement is clearly achieved. Results are presented for the elements QU8F4L4, QU8F4L1 and QU9F9L4. It is clear from Figure 4.4 that with increasing refinement of the mesh the finite element solution converges quickly to the analytical solution for these elements. For the other elements the results are similar. For the elements QU8F4L4, QU8F4L1 the convergence rate is slower than for element QU9F9L4, which is due to the higher-order of approximation for the deformation gradient components used in the latter element.

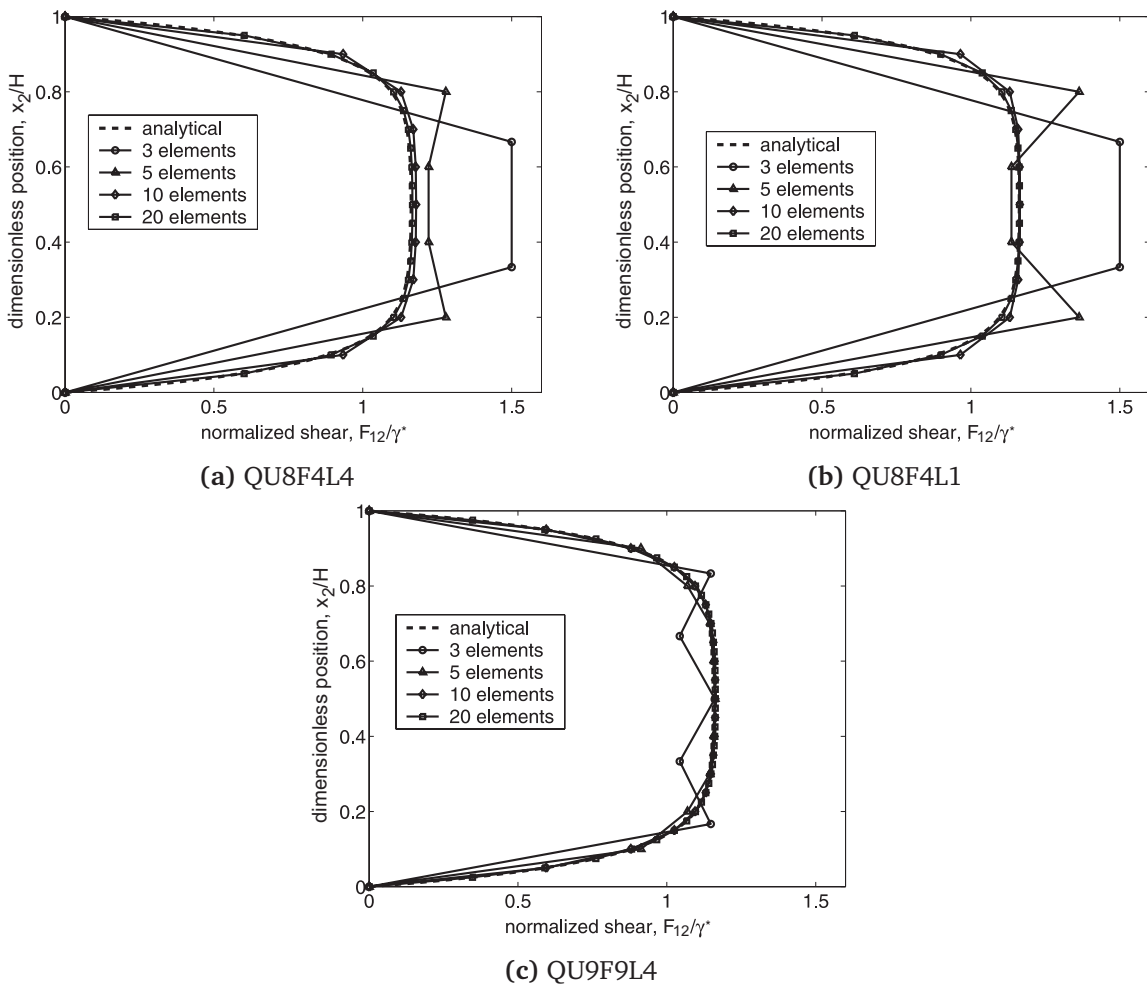


Figure 4.4: Shear strain distribution along the height of the boundary shear layer. Convergence of the numerical solution to the analytical one upon mesh refinement for different types of elements.

In order to further evaluate the accuracy of the elements, the calculated traction t_1 and double traction r_1 on the top boundary of the layer $X_2 = H$ have been compared to the analytical values according to (4.88) and (4.89). The results are summarized in Table 4.2. Again, the elements QU8F4L1 and QU9F9L4 demonstrate good convergence of the numerically obtained values to the analytical solution, with a higher convergence

rate for element QU9F9L4. As can be noticed from Table 4.2 element QU8F4L4 provides traction values that deviate significantly from the analytical solution even for a rather fine discretization (but still converges). However, it should be recalled that this element did pass neither the count test nor the quadratic patch test. So the results for the boundary tractions illustrate once more the relatively bad properties of element QU8F4L4.

Table 4.2: Comparison between the calculated and analytical values of the tractions and double tractions on the upper boundary of the shear layer for different elements and discretizations.

element type	mesh, N_{elem}	traction t_1 , [N/mm]	double traction r_1 , [N]
QU8F4L4	3	79.0500	-9.5250
	5	73.4013	-6.7006
	10	70.8174	-5.4088
	20	70.1209	-5.0605
QU8F4L1	3	71.5500	-5.7750
	5	69.8863	-4.9432
	10	69.8827	-4.9414
	20	69.8828	-4.9414
QU9F9L4	3	69.8633	-4.9316
	5	69.8828	-4.9414
	10	69.8830	-4.9415
	20	69.8830	-4.9415
analytical		69.8829	-4.9415

4.4.4 Choice of elements

Recommendations on the choice of appropriate finite elements for the numerical solution of second gradient equilibrium problems can now be easily formulated. As has been indicated by the patch test, the elements QU8F4L4, QU8F8L4 and QU9F4L4 cannot be recommended, since they do not possess acceptable stability and convergence properties. Based on the tests performed so far, the other three elements developed: QU8F4L1, QU9F4L1 and QU9F9L4 all seem to be well-suited for practical use. Element QU9F9L4 provides a better accuracy, however leads to a system of equations, which is about two times larger than for the other two elements. To avoid the appearance of zero energy modes, the nine displacement node elements QU9F4L1 and QU9F9L4 should be used only with a 3×3 Gauss integration scheme. Element QU8F4L1 also performs well with a 2×2 Gauss integration scheme. This observation is crucial for the selection of an element for the second-order computational homogenization analysis, where generally at every macroscopic integration point a microstructural analysis has to be performed. The use of a 9 integration points scheme instead of 4 integration points would increase the number of required microstructural analyses more than twice. Therefore, in this work all of the coupled second-order micro-macro computations (next chapter) will be performed using element QU8F4L1.

Chapter 5

Comparative analyses

In the previous chapters the first-order and second-order computational homogenization schemes have been elaborated. This chapter focuses on the comparison of the performance of these two techniques. Several examples are discussed. First, in section 5.1 microstructural representative cells subjected to a given macroscopic deformation path are analyzed. The results obtained from the first-order and the second-order computational homogenization modelling are compared and the ability of the second-order scheme to capture size and gradient effects is demonstrated. Two examples of coupled multi-scale computational homogenization are presented. In section 5.2 a benchmark problem, which allows an evaluation of the performance of the first-order and the second-order computational homogenization techniques upon macroscopic localization, is considered. Finally, in section 5.3 the second-order computational homogenization approach is used to model a configuration with a boundary shear layer.

5.1 Microstructural analyses

In this section some advanced features of the novel second-order computational homogenization scheme are illustrated by the analysis of a single representative volume element subjected to a given macroscopic loading path. The microstructural responses resulting from the first-order and the second-order scale transition are compared. The first example deals with the macroscopic deformation corresponding to the upper part of a specimen under macroscopic bending, so that the deformation field is a superposition of bending and tension. In the second example, the macroscopic deformation path is extracted from data describing the deformation in the vicinity of the notch of a notched specimen under tension. Finally, the ability of the second-order scheme to capture geometrical size effects and gradient effects is illustrated.

All examples in this section consider voided aluminum (initially 12% volume fraction of voids) at the microlevel. The undeformed representative volume element (RVE), with the finite element discretization used in the calculations, is shown in Figure 5.1. The absolute dimensions of the RVE are chosen such that the second-order deformation

mode will be clearly visible. The characteristic microstructural size (average size of voids) will be specified for every particular example. The aluminum matrix is described by an elasto-visco-plastic Bodner-Partom constitutive model. This non-linear history and strain rate dependent model is formulated in a finite kinematics context and is briefly outlined in appendix A.3. In the present calculations the material parameters for annealed aluminum AA 1050 determined by van der Aa et al. (2000) have been used; elastic parameters: shear modulus $G = 2.6 \times 10^4$ MPa, bulk modulus $K = 7.8 \times 10^4$ MPa and viscosity parameters: $\Gamma_0 = 10^8 \text{ s}^{-2}$, $m = 13.8$, $n = 3.4$, $Z_0 = 81.4$ MPa, $Z_1 = 170$ MPa.

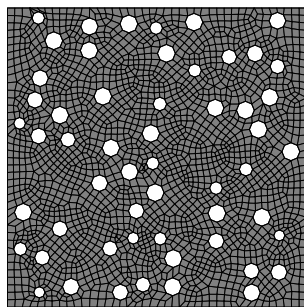


Figure 5.1: Undeformed representative volume element (RVE), discretized with a finite element mesh.

5.1.1 Macroscopic bending and tension

Bending is probably one of the most appealing cases for which the local gradients of the deformation are not negligible and significantly determine the deformation pattern. Therefore in the first example the macroscopic deformation path (deformation gradient tensor \mathbf{F}_M and its gradient ${}^3\mathbf{G}_M$) has been taken from a point in the upper part of the specimen, as indicated in Figure 5.2. The deformation path, which is a superposition of bending and tension, has been applied on the microstructural voided RVE (shown in Figure 5.1) with an average size of the voids in the undeformed configuration equal to $6.625 \mu\text{m}$. The resulting deformed RVE with the equivalent plastic strain distribution is shown in Figure 5.3a. For a comparison an RVE of the same size but modelled within the first-order framework, for which only the deformation tensor \mathbf{F}_M and pure periodic boundary conditions are prescribed, is depicted in Figure 5.3b.

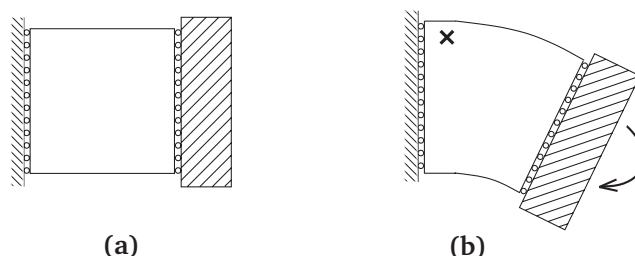


Figure 5.2: Schematic representation of the macroscopically bended specimen: initial configuration (a) and deformed configuration (b). The point at which the deformation path (deformation gradient tensor \mathbf{F}_M and its gradient ${}^3\mathbf{G}_M$) has been recorded for use in the microstructural analysis is indicated.

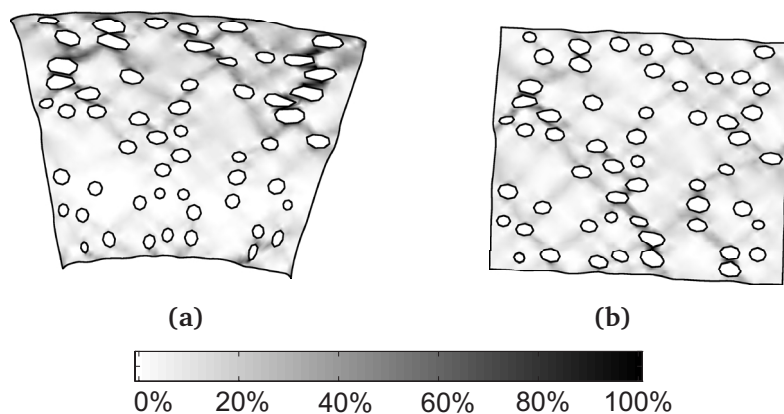


Figure 5.3: Distribution of the equivalent plastic strain in the deformed RVEs subjected to a macroscopic bending-tension deformation path according to the second-order scheme (a) and the first-order scheme (b).

The macroscopic bending mode is clearly visible for the second-order RVE (Figure 5.3a). Moreover it can be observed that although the overall bending-tension deformation mode is prescribed, due to the “generalized” periodic boundary conditions (3.14) and (3.17), some freedom is provided to the microstructural fluctuations on the boundary. It is easy to notice that this fluctuation field is periodic on the boundaries, while the overall deformation of the RVE is not.

It is emphasized that using the first-order or the second-order approach to prescribe the deformation mode of the RVE, not only results in different overall deformation modes (and consequently in different averaged responses), but also reveals considerable differences in the deformation patterns within the microstructure. This can be clearly seen by comparing the local distribution of the equivalent plastic strain in an RVE undergoing the second-order deformation mode (Figure 5.3a) and the first-order deformation mode (Figure 5.3b). Apparently, local deformations can be much larger in the higher-order case. Depending on the non-linear character of the material behaviour of the microstructure, this difference in local deformations may lead to considerable differences in the extracted macroscopic stresses. Additionally, the difference in local microstructural fields obtained from the first and second-order computational homogenization modelling is relevant if a local failure criterion is used (e.g. if a critical local stress and/or strain should be taken into account). Moreover, if the microstructural constitutive behaviour is gradient-sensitive (e.g. discrete lattices etc.), the response obtained with incorporation of the gradients (the second-order framework) will substantially differ from the case without gradients included (the first-order framework).

5.1.2 Macroscopic model of a notched specimen under tension

At the macroscopic level this example deals with a notched tensile specimen. The gradients of the deformation are quite large in the vicinity of the notch. It is characteristic in this example that stretch gradients prevail over rotation gradients.

The stretch and rotation gradients may be separated by decomposition of the gradient of the deformation gradient tensor ${}^3\mathbf{G}_M = \nabla_{0M}\mathbf{F}_M$ into a symmetric part ${}^3\mathbf{G}_M^S$ and an antisymmetric part ${}^3\mathbf{G}_M^A$, see e.g. Fleck and Hutchinson (1997). The symmetric part,

representing the stretch gradients is obtained as

$$G_{Mijk}^S = \frac{1}{3} (G_{Mijk} + G_{Mjki} + G_{Mkij}). \quad (5.1)$$

Consequently the antisymmetric part, which describes the rotation gradients, is defined by

$${}^3G_M^A = {}^3G_M - {}^3G_M^S. \quad (5.2)$$

This tensor ${}^3G_M^A$ is a third-order tensorial representation of the second-order curvature tensor, which is the only higher-order deformation quantity in the couple-stress theory, as given for example in Mindlin and Tiersten (1962); Koiter (1964); Fleck et al. (1994).

In order to investigate the influence of the macroscopic stretch and rotation gradients on the overall microstructural behaviour in the particular case of the notched tensile specimen, the macroscopic deformation path at the point near the tip of the notch, as indicated in Figure 5.4, has been extracted from the numerical analysis. First this deformation path (deformation gradient tensor F_M and its full gradient 3G_M) has been applied on the RVE, shown in Figure 5.1, with the average size of the voids in the undeformed configuration equal to $0.133 \mu\text{m}$. The deformed shape of the RVE and the distribution of the equivalent plastic strain are presented in Figure 5.5a. Next, the deformation path prescribed by the deformation gradient tensor F_M and only the rotation gradients, which are represented by ${}^3G_M^A$ and calculated according to (5.2), has been applied on the same undeformed RVE. The deformed RVE in this case is shown in Figure 5.5b.

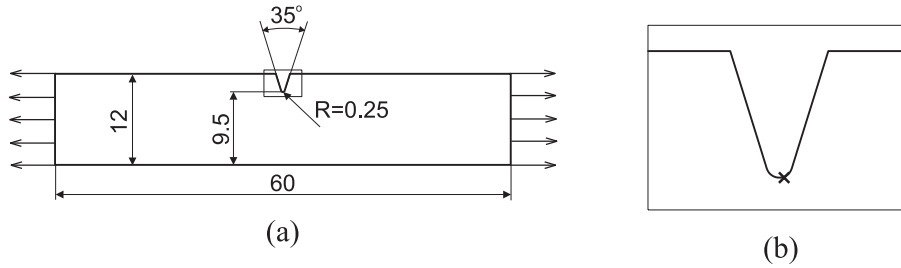


Figure 5.4: Schematic representation of the notched specimen (with dimensions in mm) under tension (a) and a magnified area near the notch (b). The point at which the deformation path (the deformation gradient tensor F_M and its gradient 3G_M) has been recorded for use in the microstructural analysis is indicated. Note that the point is located slightly right of the symmetry axis.

The higher-order deformation mode in this example is dominated by stretch gradients, the contribution of the rotation gradients (although present) remains small. As a result the RVE subjected to the deformation described by F_M and the antisymmetric tensor ${}^3G_M^A$ (Figure 5.5b) deforms almost periodically, which deviates considerably from the deformed shape of the RVE subjected to F_M and the full tensor 3G_M (Figure 5.5a). This indicates that the well-established couple-stress theories, which include only the rotational gradients ${}^3G_M^A$, would not give satisfactory results in this case, since these theories do not account for the stretch gradients, which are dominant in this case. This motivates the use of the full second gradient formulation for the description at the macrolevel within the second-order computational homogenization framework.

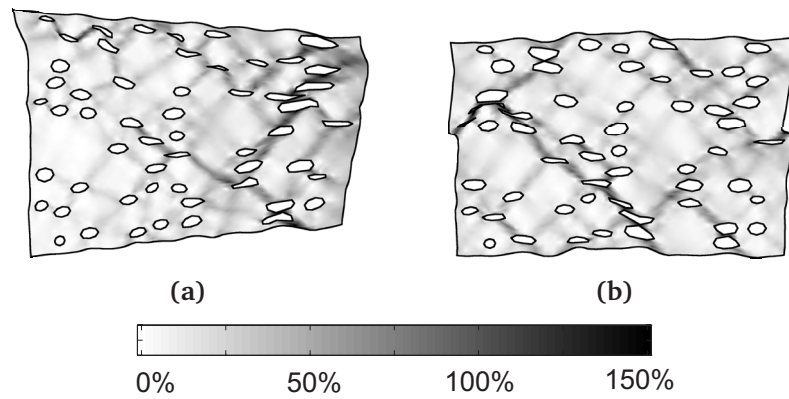


Figure 5.5: Distribution of the equivalent plastic strain in the deformed RVEs subjected to the deformation path in the vicinity of the notch of the macroscopic notched tensile specimen; (a) the RVE is subjected to the deformation gradient tensor \mathbf{F}_M and its full gradient ${}^3\mathbf{G}_M$; (b) the RVE is subjected to the deformation gradient tensor \mathbf{F}_M and only the rotational part ${}^3\mathbf{G}_M^A$ of its gradient.

5.1.3 Microstructural and size effects

Influence of the size of the microstructural constituents

In this section the capability of the second-order computational homogenization approach to account for the size of microstructural constituents is demonstrated. For this purpose, microstructures having a different absolute size are considered. A number of initially morphologically identical RVEs (Figure 5.1) with a different average size of the voids, ranging from $0.013 \mu\text{m}$ to $6.625 \mu\text{m}$, have been subjected to the same macroscopic bending-tension deformation path as the one used in section 5.1.1. Figure 5.6 shows the resulting deformed RVEs with different microstructural dimensions.

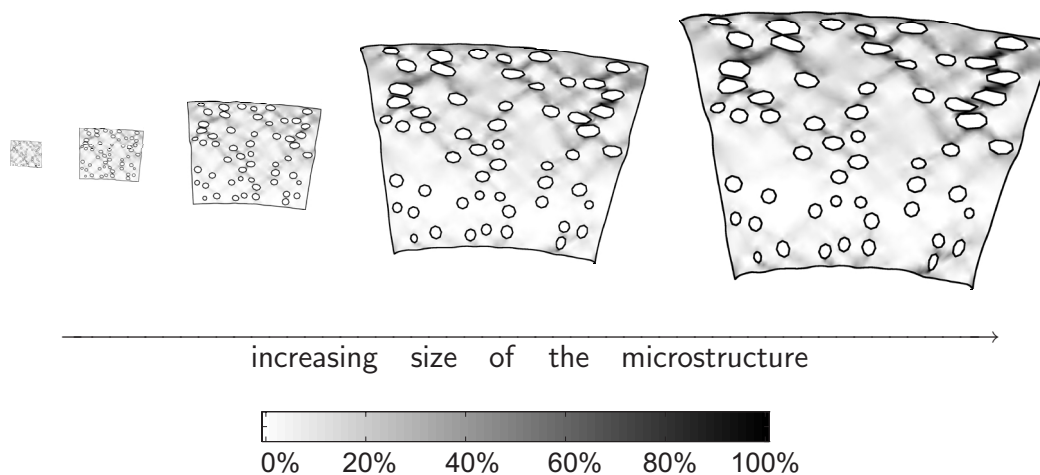


Figure 5.6: Dependence of the overall deformation mode and the local equivalent plastic strain on the size of the microstructure. Average size of the voids in the initial configuration (from the left to the right): $0.133 \mu\text{m}$ (5 times extra magnified), $1.325 \mu\text{m}$, $2.650 \mu\text{m}$, $5.300 \mu\text{m}$ and $6.625 \mu\text{m}$. All the RVEs are subjected to the macroscopic bending-tension deformation path earlier mentioned.

Clearly, the deformation mode depends on the size of the microstructure. As a consequence the overall response, extracted from such a model also depends on the microstructural size, as can be observed in Figure 5.7, where the scalar equivalent values of the RVE averaged first Piola-Kirchhoff stress tensor $P_M^{\text{eq}} = (P_{Mij}P_{Mij})^{1/2}$ and the higher-order stress tensor $Q_M^{\text{eq}} = (Q_{Mijk}Q_{Mijk})^{1/2}$ are considered as a function of the characteristic size of the microstructure. This figure clearly illustrates the influence of the size of the microstructural constituents in the second-order computational homogenization framework.

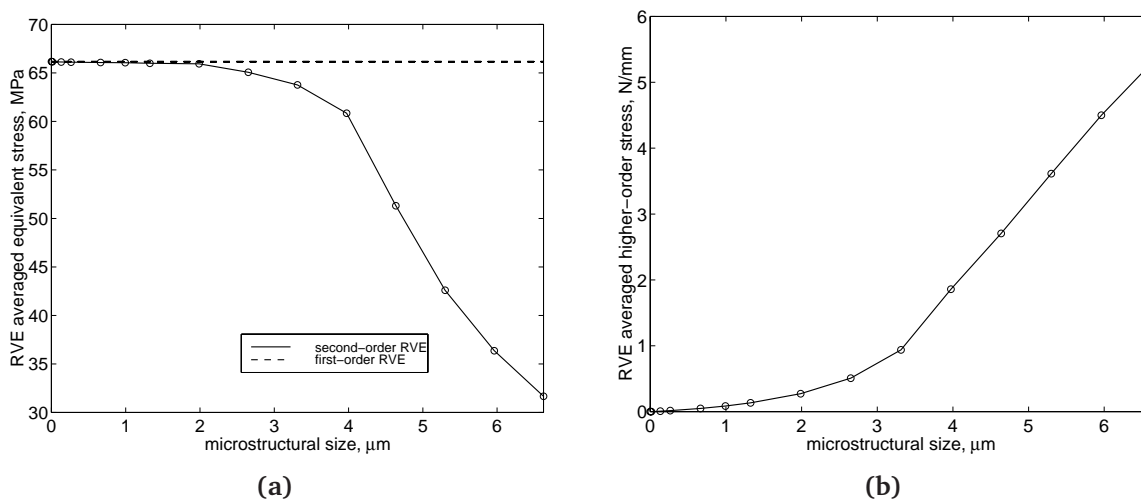


Figure 5.7: Equivalent measures of the RVE averaged first Piola-Kirchhoff stress tensor (a) and the higher-order stress tensor (b) vs. the characteristic microstructural size (averaged size of the voids).

It is important to notice that the second-order approach is a natural extension of the first-order technique. When the microstructural size becomes negligible (with respect to the length scale of spatial variations in the applied macroscopic deformation field) the influence of the higher-order deformation modes vanishes and the structure deforms periodically, see Figure 5.6 (left). The same conclusion follows from a consideration of the RVE averaged stress and higher-order stress, Figure 5.7. The result inherently depends on the size of the microstructure and upon reducing the size, the stress state converges to the response of the first-order case.

Size effects for a given microstructure

The microstructural size effects discussed in the above section concern changes in the overall macroscopic response due to variations of the characteristic size of the microstructural components (in this case prescribed by the average diameter of the voids). However, when the microstructural size does not change (a material with a given microstructure is considered), yet another type of size effect may appear. This is the case if the microstructural size is no longer negligible with respect to the characteristic length of the macroscopic deformation field. This may occur due to a relatively small size of the macroscopic configuration (e.g. thin layers, thin wires or miniaturized components) or when localization of deformation takes place at the macrolevel. These size effects, which are generally associated with a dominant influence of the microstructure at the macrolevel, usually manifest themselves through the dependence of the overall mate-

rial response not only on the value and history of the deformation tensor but also on its gradient. A collection of examples showing such size effects may be found in Fleck and Hutchinson (1997). Classical continuum mechanics material models and, consequently, the first-order computational homogenization scheme, are not able to describe this size effect, since they do not incorporate a microstructural length scale. The second-order framework, on the other hand, is well capable to deal with these size effects, due to the application of higher-order boundary conditions and the straightforward account of the macroscopic gradient of the deformation tensor. This is illustrated in the following example.

Identical microstructural RVEs (average size of the voids $13.25 \mu\text{m}$) have been subjected to different tensile-bending macroscopic deformation histories. In these histories the deformation tensor \mathbf{F}_M is the same, but its gradient, while representing the same deformation mode (bending), has different intensities. This has been achieved by a component-wise linear increase of the components of the prescribed ${}^3\mathbf{G}_M$, actually reflecting bending of macroscopically decreasing samples. The resulting deformed RVEs (for an equivalent value $G_M^{\text{eq}} = (G_{Mijk}G_{Mijk})^{1/2}$ of the gradient of the deformation equal to 0 mm^{-1} , 0.19 mm^{-1} , 0.39 mm^{-1} , 0.78 mm^{-1} and 0.98 mm^{-1}) are shown in Figure 5.8. The left picture in Figure 5.8 corresponds to the first-order case, not accounting for the gradient of the deformation. Clearly, depending on the intensity of the gradient of the deformation tensor, the overall deformation mode differs, which will result in different extracted overall responses, thereby capturing the size effect. Also it may be observed from Figure 5.8 that when the gradient of the macroscopic deformation becomes negligible (with respect to the microstructural size) the influence of the higher-order deformation mode vanishes. This again demonstrates the natural convergence of the second-order computational homogenization scheme to the first-order scheme at vanishing gradients of the macroscopic deformation field.

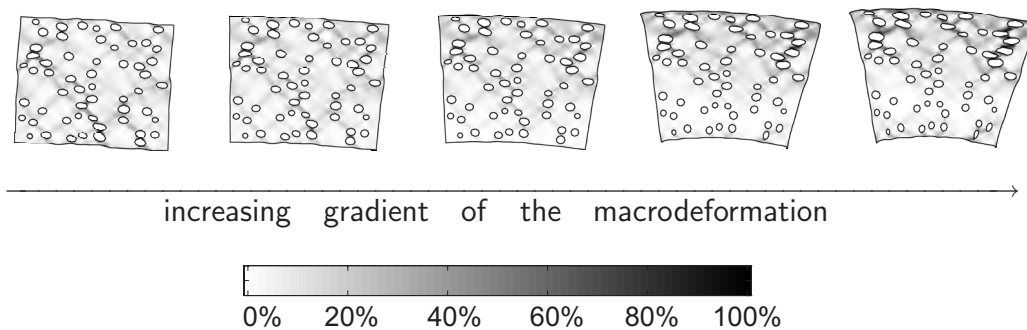


Figure 5.8: Dependence of the overall deformation mode and the local equivalent plastic strain on the intensity of the gradient of the macroscopic deformation tensor. All the RVEs (initially identical, average size of the voids $13.25 \mu\text{m}$) have been subjected to a macroscopic bending-tension deformation history with the same deformation tensor \mathbf{F}_M and a different gradient ${}^3\mathbf{G}_M$ with intensities (from the left to the right): $G_M^{\text{eq}} = 0 \text{ mm}^{-1}$, 0.19 mm^{-1} , 0.39 mm^{-1} , 0.78 mm^{-1} and 0.98 mm^{-1} .

Although it is recognizable that the two types of size effects considered above, i.e. due to variations of the size of the microstructure and due to variations of the gradients of the macroscopic deformation, are, in fact, identical from a conceptual point of view, it has been found instructive to illustrate them in separate examples, since they both

can be independently captured within the second-order computational homogenization framework.

5.2 Computational homogenization modelling of macroscopic localization

This section investigates the ability of the first- and second-order computational homogenization techniques to deal with macroscopic localization phenomena. To this purpose, an academic benchmark problem will be considered.

A regularly perforated structure (with areas of homogeneous material at the edges) under tensile loading is modelled. Exploiting the symmetry of the problem only one quarter, as depicted in Figure 5.9a, will be analyzed. The size of this quarter is $7d$ by $12d$, with d the stacking distance of the void pattern. The diameter of a void is $0.4d$, which results in a volume fraction of voids of approximately 12.5%. In the present computations the geometrical parameter d has been taken equal to $10\ \mu\text{m}$. Plane strain conditions are assumed. The behaviour of the matrix material is described by the elastoplastic model, summarized in appendix A.2. The material parameters correspond to commercial steel T67CA, Young's modulus $E = 210 \times 10^3\ \text{MPa}$, Poisson's ratio $\nu = 0.3$ and the yield stress $\sigma_{y0} = 507\ \text{MPa}$, hardening is neglected. In order to trigger localization, a smooth material imperfection has been introduced. In the imperfection region the yield stress of the matrix material has been gradually reduced in a range of 4% to 20%, as depicted in Figure 5.9a. A smooth imperfection has been used in order to avoid that the width of the localization band depends on the imperfection area size. To evaluate the results obtained by computational homogenization, also a "direct" simulation is performed, in which the whole macrostructure is analyzed, using the finite element mesh shown in Figure 5.9b (note that in the center of the plate the mesh is extra refined). Results of this direct modelling are considered as a reference solution.

Evidently, the example considered has a coarse microstructure. This benchmark problem is used to explore limitations of the homogenization methods presented, thus computational efficiency is not the main issue. Furthermore, as remarked several times before, the true limiting factor is the ratio of the characteristic length of the deformation field with respect to the size of the microstructure.

The macroscopic model and the microstructural unit cell for the homogenization analysis are shown in Figure 5.10. The particular choice of the simplest unit cell for the actual analysis is motivated by the fact that this unit cell contains all statistical information and for the truly periodic configuration (which is considered here) it is known to be a valid representative volume element in the first-order homogenization framework. It is emphasized that the size d of the square unit cell is important in the second-order computational homogenization, while this size is irrelevant for the first-order homogenization analysis. To account for the imperfection zone, the yield stress of the matrix material of the unit cells, corresponding to macroscopic points within this zone has been reduced by the respective value.

It is remarked that in the problem described, no material softening of the matrix material is present. Possible softening at a macroscopic material point is therefore entirely due to geometrical softening of the attributed microstructural unit cell. The response of a single unit cell under uniaxial tension is shown in Figure 5.11. Only a slight geomet-

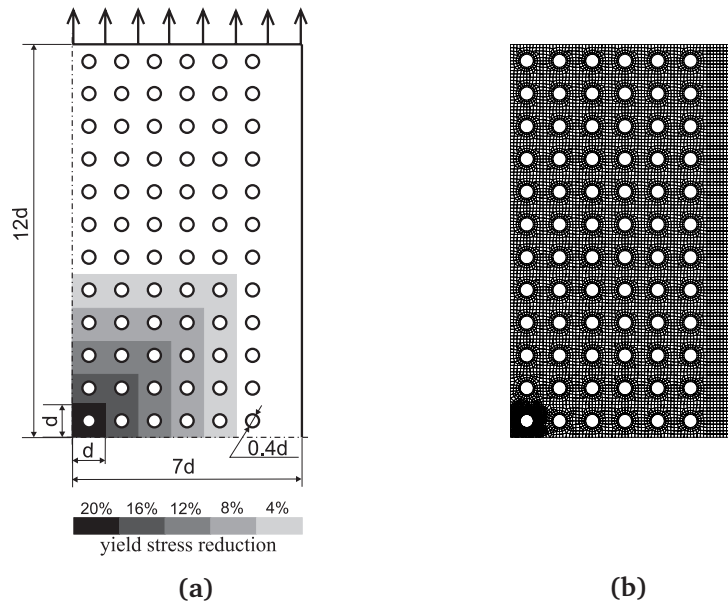


Figure 5.9: (a) The perforated plate (one quarter) under tensile loading; the shaded area indicates a gradual material imperfection with a reduced yield stress. (b) The finite element mesh for the reference solution.

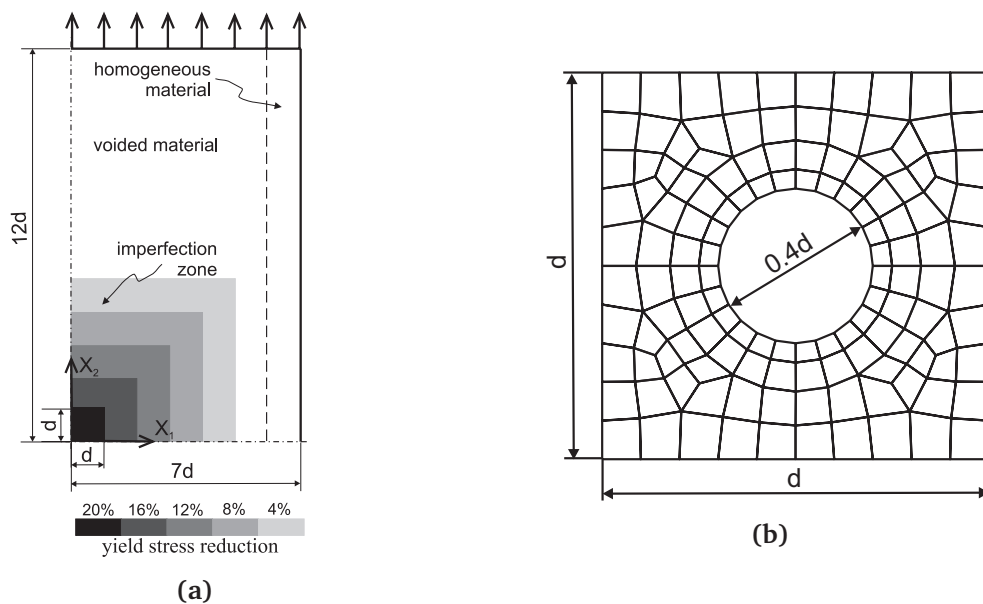


Figure 5.10: The macroscopic model (a) and the microstructural unit cell with the finite element mesh (b) for the homogenization analysis.

rical softening can be observed.

The homogenization analysis of this problem has been performed using the first- and second-order computational homogenization schemes. For the solution at the macroscopic level, two finite element discretizations with different sizes of elements in the imperfection zone have been used, as shown in Figure 5.12. For the purpose of the following discussion these finite element meshes will be referred to as “coarse” (Figure 5.12a) and “fine” (Figure 5.12b). For the first-order computational homogenization analysis standard eight-noded plane strain elements have been used. For the second-

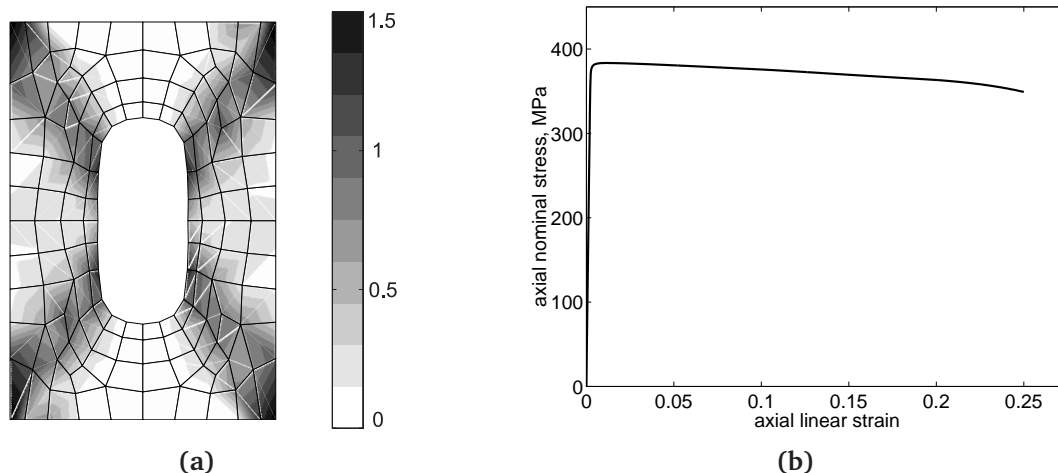


Figure 5.11: Single unit cell under uniaxial tension. (a) Deformed geometry and distribution of the equivalent Green-Lagrange strain within the unit cell. (b) Stress-strain response.

order computational homogenization modelling, which deals with a second gradient continuum on the macrolevel, the element QU8F4L1 developed in chapter 4 has been employed (see section 4.3.4 for the description of this element). For both the first- and second-order finite element analyses a 2×2 Gauss integration scheme has been applied.

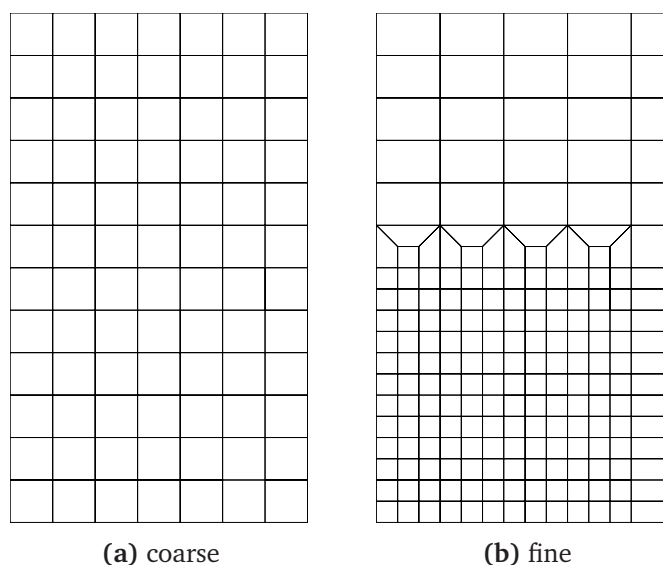


Figure 5.12: Finite element discretizations of the macrostructure used in the first- and second-order computational homogenization analyses.

Note that the finite element size of the macromesh is by no means related to the underlying microstructure, since this size is only a discretization parameter for the numerical solution of the macroscopic continuum problem. For the considered benchmark problem it might therefore happen that macroscopic finite elements are smaller than the coarse microstructural length scale (size of the unit cell). Again, this is not regarded as a problem, since the macroscopic numerical discretization has to be independent of the microstructure. At a macroscopic material point the mechanical response is obtained by averaging over the corresponding unit cell.

Along the edges of the domain boundary conditions have to be specified. In the first-order computational homogenization analysis a classical boundary value problem has to be solved, thus only displacements and/or tractions have to be prescribed on the boundary. The second-order scheme deals with an equilibrium problem for the second gradient continuum on the macrolevel. This requires additional higher-order boundary conditions. In the present implementation the higher-order boundary conditions are accommodated through prescribed components of the relaxed deformation gradient tensor $\hat{\mathbf{F}}$ and/or the double stress tensor \mathbf{R} (see chapter 4 for the definition of these quantities). For the problem considered here, the boundary conditions to be imposed on the macrostructure are taken according to

$$\begin{aligned} t_1 = 0, \quad u_2 = 0, \quad \hat{F}_{21} = 0, \quad R_{11} = 0, \quad R_{22} = 0, \quad R_{12} = 0 \quad \text{on} \quad X_2 = 0, \\ t_1 = 0, \quad u_2 = U^*, \quad \hat{F}_{21} = 0, \quad R_{11} = 0, \quad R_{22} = 0, \quad R_{12} = 0 \quad \text{on} \quad X_2 = 12d, \\ u_1 = 0, \quad t_2 = 0, \quad \hat{F}_{12} = 0, \quad R_{11} = 0, \quad R_{22} = 0, \quad R_{21} = 0 \quad \text{on} \quad X_1 = 0, \\ t_1 = 0, \quad t_2 = 0, \quad R_{11} = 0, \quad R_{22} = 0, \quad R_{12} = 0, \quad R_{21} = 0 \quad \text{on} \quad X_1 = 7d, \end{aligned}$$

where U^* is the prescribed tensile displacement. The actual choice of the higher-order boundary conditions made here is rather arbitrary and in fact requires additional investigations, which are beyond the scope of the present work.

Figure 5.13 presents the macroscopic force-displacement curves (for the quarter modelled) obtained from the first-order computational homogenization (Figure 5.13a) and the second-order computational homogenization (Figure 5.13b) using the two finite element discretizations of the macrostructure. To enable a comparison the reference solution obtained from the detailed modelling of the heterogeneous macrostructure is also presented.

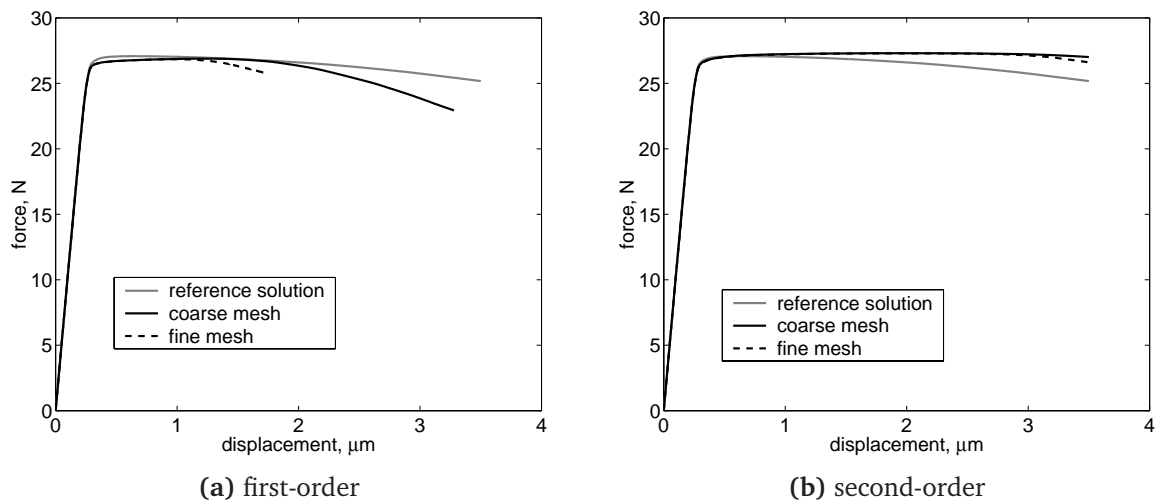


Figure 5.13: Macroscopic force-displacement curves obtained from the first-order (a) and the second-order (b) computational homogenization schemes for the two finite element discretizations of the macrostructure. The reference solution resulting from a detailed modelling of the heterogeneous macrostructure is also shown.

The onset of yielding of the macroscopic heterogeneous structure is slightly better predicted by the second-order computational homogenization scheme, which is related

to the participation of the macroscopic gradient of the deformation field in addition to the deformation field itself. The first-order analysis underestimates the force at the onset of yielding a little bit. The initial stage of yielding is described well by both schemes. However, as the macroscopic localization develops, the difference between the first- and second-order computational homogenization approaches becomes apparent. The macroscopic response obtained by the first-order technique clearly exhibits a strong mesh dependency. Each grade of mesh refinement results in an earlier peak load combined with a higher decrease rate of the force. Moreover, the first-order computations could not be performed over the whole range of the prescribed macroscopic displacement. As can be noticed from Figure 5.13a, the analyses stopped earlier (especially for the fine mesh) due to excessive deformation concentrated in the volume related to one single integration point and the highly distorted mesh of the respective microstructural unit cell.

The second-order scheme provides mesh independent results. A very small difference in the responses obtained from the different discretizations is observed at the very late stage of loading, which can be eliminated through further mesh refinement. As can be noticed, the response obtained by the second-order approach slightly overestimates the reference solution. This may be attributed to the fact that at this stage of loading the macroscopic fields fluctuate strongly over the scale of the microstructure, so that the underlying assumption in the second-order approach, on a linear variation of the macroscopic deformation field over the microstructural cell does not exactly apply.

The comparison of the results obtained from the first- and second-order computational homogenization modelling is continued by an examination of the distributions of the macroscopic deformation field. Figure 5.14 presents the distribution of the macroscopic equivalent total strain resulting from the first-order computational homogenization analysis for the two finite element discretizations at a prescribed macroscopic displacement $U^* = 1.76 \mu\text{m}$. Again, a strong mesh dependency is observed. The deformation localizes according to the size of the elements used. Observe also the significantly increasing value of the maximum equivalent strain obtained with refinement of the finite element mesh. While for the coarse mesh the maximum strain in the localization zone is about 30%, for the fine mesh it reaches 63%. Since there is no singularity present in this problem, the increase in the maximum strain upon mesh refinement is purely due to the localization of the deformation in the decreasing volume related to the size of the elements.

A noticeably different macroscopic deformation pattern is obtained from the second-order computational homogenization modelling. Figure 5.15 shows the distribution of the macroscopic equivalent Green-Lagrange strain resulting from the second-order computational homogenization analysis for the two finite element discretizations at the same prescribed macroscopic displacement as for the first-order case, $U^* = 1.76 \mu\text{m}$. Clearly, as well as it is the case for the force-displacement response, the local macroscopic deformation field pattern obtained by the second-order scheme is mesh independent.

The distribution of the equivalent strain obtained from the direct finite element modelling of the heterogeneous macrostructure is shown in Figure 5.16a. However, these equivalent strain values cannot be compared quantitatively to the values of the macroscopic strain obtained from the homogenization analyses, since the former, in fact, apply to the microscale, while the latter correspond to the deformation field over the macro-

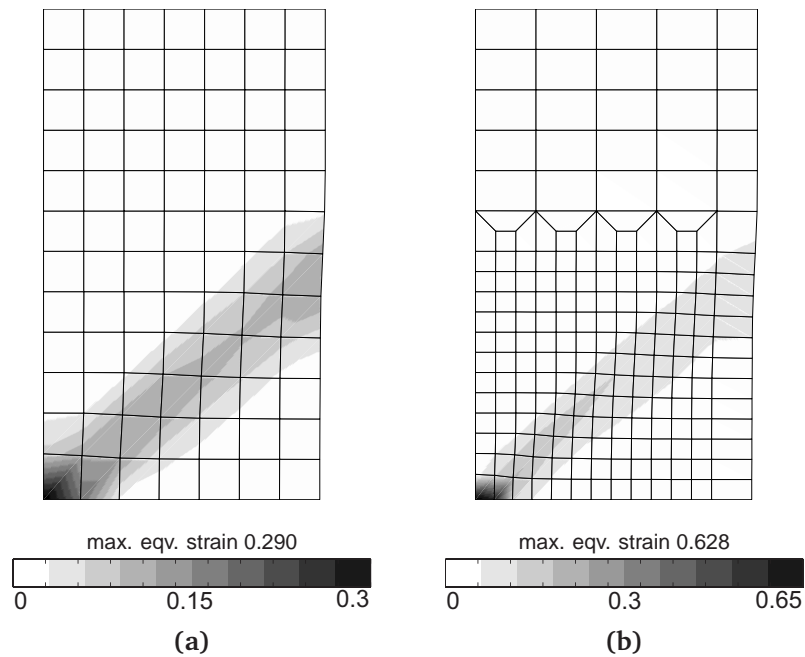


Figure 5.14: Distribution of the equivalent Green-Lagrange strain resulting from the first-order computational homogenization modelling for the two finite element discretizations: (a) coarse mesh and (b) fine mesh at the prescribed macroscopic displacement $U^* = 1.76 \mu\text{m}$. The actual maximum equivalent strain values are indicated.

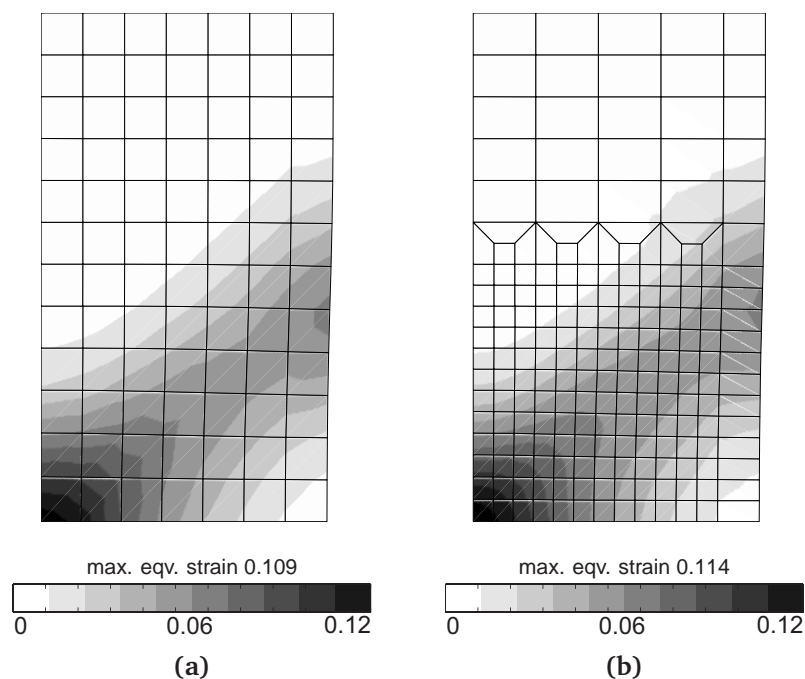


Figure 5.15: Distribution of the equivalent Green-Lagrange strain resulting from the second-order computational homogenization modelling for the two finite element discretizations: (a) coarse mesh and (b) fine mesh at the prescribed macroscopic displacement $U^* = 1.76 \mu\text{m}$. The actual maximum equivalent strain values are indicated.

scopic homogenized structure. In order to be able to perform a comparison between the macroscopic deformation patterns resulting from the homogenization modelling and the reference solution, the deformation field obtained by the detailed modelling has been (volume-)averaged over every “unit cell” of the perforated structure and visualized using the standard interpolation procedure. This results in the macroscopic deformation pattern of the reference solution presented in Figure 5.16b. Comparison of this reference solution with the results of the first- (Figure 5.14) and second-order (Figure 5.15) computational homogenization, reveals that although the deformation pattern corresponding to the second-order modelling is less sharp compared to the reference pattern it reproduces the reference solution significantly better than the first-order scheme. Here again, the slightly “violated” assumption on the linear variation of the macroscopic deformation field over the microstructural cell may be a possible explanation of the less sharp deformation pattern obtained by the second-order scheme compared to the reference solution. Moreover, only the deformation gradient tensor field was used to plot the distribution of the equivalent strain measure, while the field of the gradient of the deformation gradient tensor was left out of consideration.

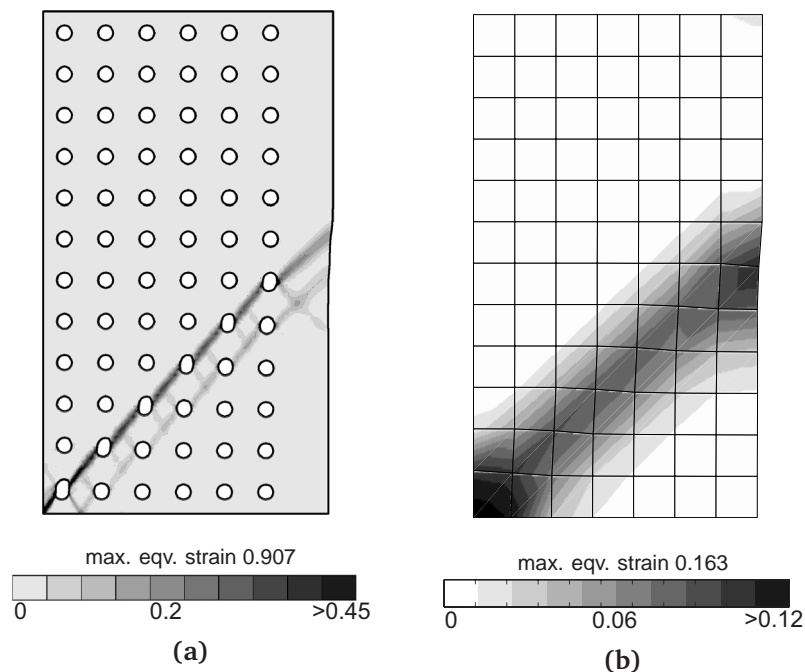


Figure 5.16: Results of the direct finite element modelling of the heterogeneous macrostructure at the prescribed macroscopic displacement $U^* = 1.76 \mu\text{m}$. Distribution of the equivalent Green-Lagrange strain. (a) Microscale solution. (b) Macroscale solution obtained by the volume averaging of the fine scale solution. The actual maximum equivalent strain values are indicated.

One of the important advantages of computational homogenization techniques over other homogenization methods is that they provide not only the overall response of a homogenized macrostructure (in terms of global loading curves and distribution of the macroscopic fields), but also simultaneously allow insight into the deformation processes occurring at the level of the heterogeneous microstructure. Figure 5.17 shows the distribution of the equivalent strain within the macrostructure and several microstructural unit cells corresponding to different macroscopic points resulting from the first-

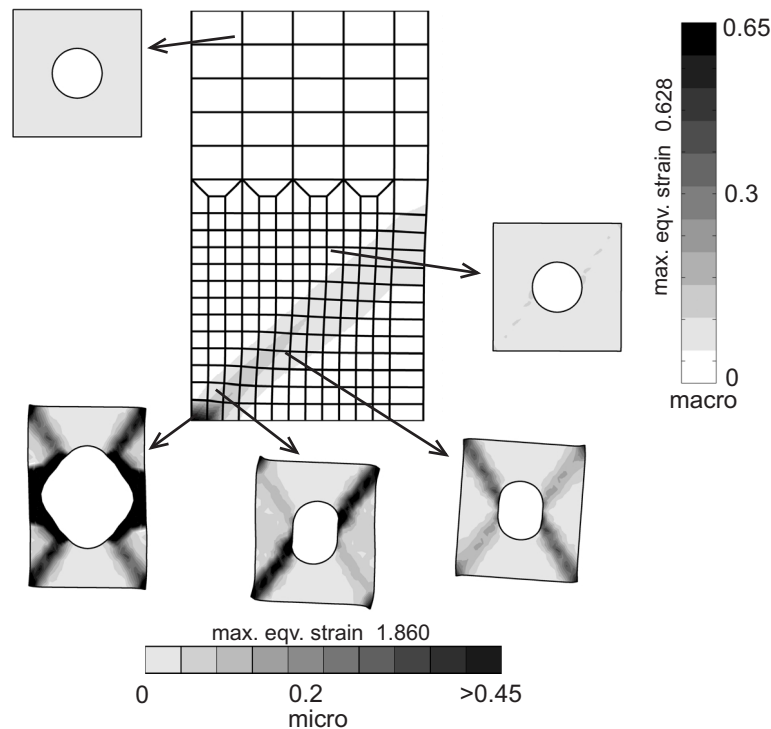


Figure 5.17: Distribution of the equivalent Green-Lagrange strain in the deformed macrostructure and several deformed microstructural unit cell, corresponding to different points of the macrostructure, obtained by the first-order computational homogenization analysis at the prescribed macroscopic displacement $U^* = 1.76 \mu\text{m}$.

order computational homogenization modelling at the prescribed macroscopic displacement $U^* = 1.76 \mu\text{m}$. The respective plot obtained from the second-order analysis is presented in Figure 5.18. Examination of the microstructural strain distribution and the overall deformation of the microstructural unit cells within the macroscopic localization zone reveals a significant difference in the microstructural responses resulting from the first- and second-order computational analyses. An excessive deformation of the microstructural cell in the localization zone obtained from the first-order computational analysis can be clearly observed. This is again a manifestation of the ill-posedness of the first-order macroscopic problem upon softening, which results in localization of the deformation in the smallest possible volume, i.e. the volume of one element. In case of the second-order computational homogenization modelling, which results in a mesh-independent width of the macroscopic localization band, the deformation is distributed more evenly over the microstructural cells within this band.

To conclude, it is pointed out that the dependence of the results (both the global response and the distribution of local fields) on the finite element discretization is typical when modelling of localization phenomena is attempted within the framework of the classical (local) continuum theory without appropriate regularization. This is a well-known fact for closed-form constitutive softening models, as has been extensively investigated by many authors in the past decade (e.g. Schreyer and Chen (1986); Bažant and Pijaudier-Cabot (1988); Aifantis (1992); de Borst and Mühlhaus (1992); de Borst and Pamin (1996); Peerlings et al. (1996); Svedberg and Runesson (1997); Geers et al.

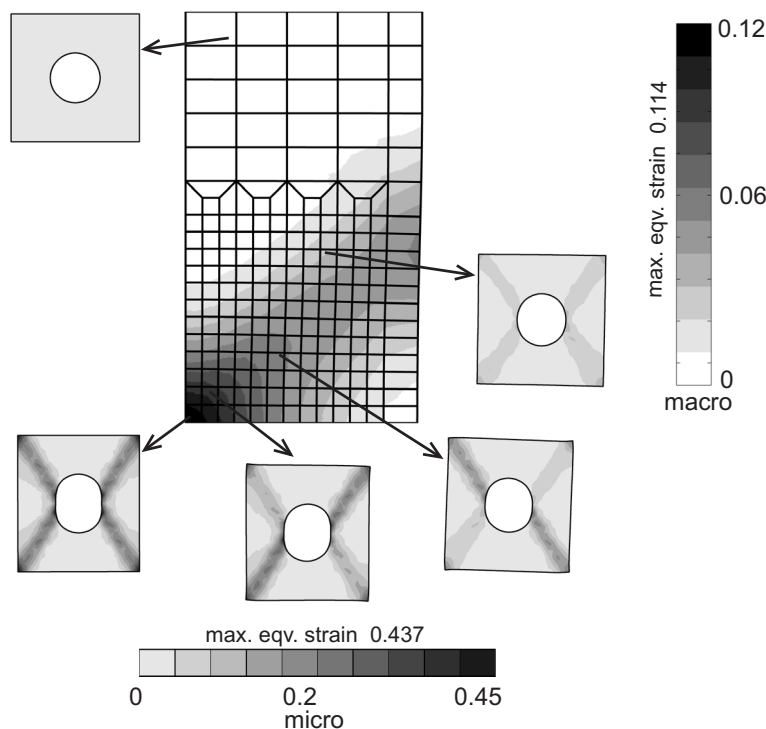


Figure 5.18: Distribution of the equivalent Green-Lagrange strain in the deformed macrostructure and several deformed microstructural unit cell, corresponding to different points of the macrostructure, obtained by the second-order computational homogenization analysis at the prescribed macroscopic displacement $U^* = 1.76 \mu\text{m}$.

(1998); Engelen et al. (2002)). Not surprisingly, the same observations are made here in the context of the first-order computational homogenization. Clearly, the first-order homogenization scheme inherits all the troublesome characteristics of the standard (local) softening models. This technique complies with the principle of local action at the macroscale, for which a softening microstructural cell cannot be used. Note that this observation even becomes more critical when the size of the finite elements is much larger than the microstructure (as normally is the case for the first-order analysis). The dissipated energy in the softening branch is then fully dominated by the (large) size of the finite elements. The second-order computational homogenization scheme, on the other hand, deals with a second gradient continuum on the macrolevel. This provides the necessary regularization and allows a realistic modelling of macroscopic zones of localized deformation.

Finally, it is repeated, that in this example the softening at a macroscopic material point was entirely due to geometrical softening of a microstructural cell. The effects observed in this section will be substantially more pronounced, if, in addition to (or instead of) geometrical softening of a microstructural cell, one or more microstructural constituents would exhibit material softening.

5.3 Computational homogenization modelling of boundary shear layers

The mechanical response of micro-systems (e.g. in micro-electronics, MEMS etc.) is known to be definitely sensitive to the characteristics of boundary (or interface) layers. In this section the modelling of boundary layer effects within the computational homogenization framework is examined by the analysis of a frequently used example, i.e. simple shear of a constrained heterogeneous strip. The boundary shear layer problem was already introduced in section 4.4.3 in the validation of the finite element implementation for the second gradient continuum, where a closed-form higher-order elastic constitutive model has been used. Here, the fully coupled multi-scale approach is pursued, with the macroscopic second gradient constitutive response obtained from the analysis of the underlying microstructure.

On the macroscopic level, plane strain shear of a two-dimensional strip with height H in the X_2 direction and “infinite” in the X_1 direction, is considered, see Figure 5.19a.

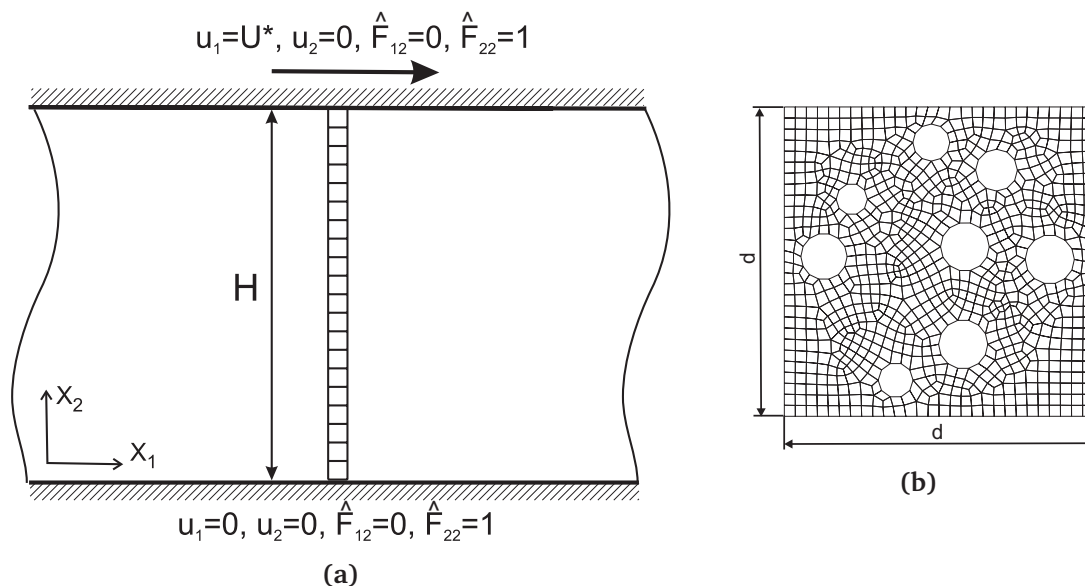


Figure 5.19: The macroscopic model (a) and the microstructural unit cell (b) for the computational homogenization analysis of the boundary shear layer problem.

In order to model the constraints at the (upper and lower) edges (which physically may be due to, for example, rigid substrates, oxide layers or a hard coating) higher-order boundary conditions prescribing vanishing shear at the surface are applied. Again, the selection of the higher-order boundary conditions is a matter of choice. As has been shown, for example, by Shu et al. (2001), not all of the possible combinations of higher-order boundary conditions give rise to a boundary layer effect. Appropriate boundary conditions in the present analysis are

$$\begin{aligned} u_1 &= 0, & u_2 &= 0, & \hat{F}_{12} &= 0, & \hat{F}_{22} &= 1 & \text{on } X_2 &= 0, \\ u_1 &= U^*, & u_2 &= 0, & \hat{F}_{12} &= 0, & \hat{F}_{22} &= 1 & \text{on } X_2 &= H, \end{aligned}$$

where $U^* = \gamma^* H$, with γ^* the prescribed shear. Instead of the condition $\hat{F}_{22} = 1$ also the normal component of the double stress traction r_2 may be set to vanish on the upper

and lower boundaries, however, this possibility is left out of consideration. The second gradient plane strain quadrilateral element QU8F4L1, as developed in section 4.3.4, has been used for the numerical analysis. Since for this simple shear problem all quantities are independent of X_1 , one single row of two-dimensional plane strain elements, as indicated in Figure 5.19a, suffices. Periodicity conditions are applied between the left and right sides of the mesh, tying the associated degrees of freedom.

The material considered consists of an elasto-plastic matrix with randomly distributed voids (12% volume fraction). The behaviour of the matrix material is described by the elasto-plastic model summarized in appendix A.2. The material parameters correspond to commercial steel T67CA, Young's modulus $E = 210 \times 10^3$ MPa, Poisson's ratio $\nu = 0.3$, the initial yield stress $\sigma_{y0} = 507$ MPa and the (constant) hardening modulus $h = 200$ MPa.

For the microscopic analysis the unit cell plotted in Figure 5.19b is used. The average diameter of the voids is $32 \mu\text{m}$. The size of the square microstructural unit cell is taken as $d = 0.2$ mm. In the present calculations the height of the macroscopic layer H has been varied between 1 mm and 10 mm, while keeping the size of the microstructural cell d unchanged. This allowed to investigate the influence of the ratio H/d , between the height of the strip and the characteristic size of the microstructure, on the development of the boundary layer. Macroscopic shear loading has been applied up to an averaged shear of $\gamma^* = 0.01$.

When the boundary value problem stated above is modelled in the context of a classical (local) continuum (with the higher-order boundary conditions left out of consideration), the solution is characterized by a homogeneous shear across the layer. The first-order computational homogenization is fully consistent with the local continuum formulation, and thus also predicts macroscopically homogeneous deformation. The second-order computational homogenization, on the other hand, allows the complete incorporation of the boundary constraints via the higher-order boundary conditions. This leads to a non-uniform macroscopic deformation distribution over the strip. Figure 5.20 shows the distribution of the shear (shear component F_{12} of the deformation gradient tensor normalized by the averaged prescribed shear γ^*) along the height of the strip for different ratios of H/d at the final shear value $\gamma^* = 0.01$. Boundary layers with a vanishing shear can be clearly observed. The width of the boundary layers reduces with an increasing ratio of H/d . For smaller values of H/d ($H/d = 5$ and $H/d = 10$) the boundary layer extends practically over the full thickness of the strip, while for larger values of H/d the zones of reduced shear and of homogeneous deformation are clearly distinguishable.

The overall shear stress-strain response obtained from the second-order computational homogenization modelling for different ratios H/d is presented in Figure 5.21. When H/d is reduced from 50 to 5 the elastic stiffness, the yield strength and the hardening rate slightly increase. Thus, the presence of constraint boundaries gives rise to a size effect, which in this case can be formulated as: "smaller is stronger". The appearance of a size effect in the elastic regime is specifically remarked. This is inherent to the second-order approach which applies to both the elastic and the elasto-plastic regimes. This clearly differs from some of the gradient plasticity theories, in which the higher-order boundary conditions are related to the plastic deformation only and thus no size effect is taken into account in the elastic region.

The development of boundary shear layers is further illustrated in Figure 5.22, which

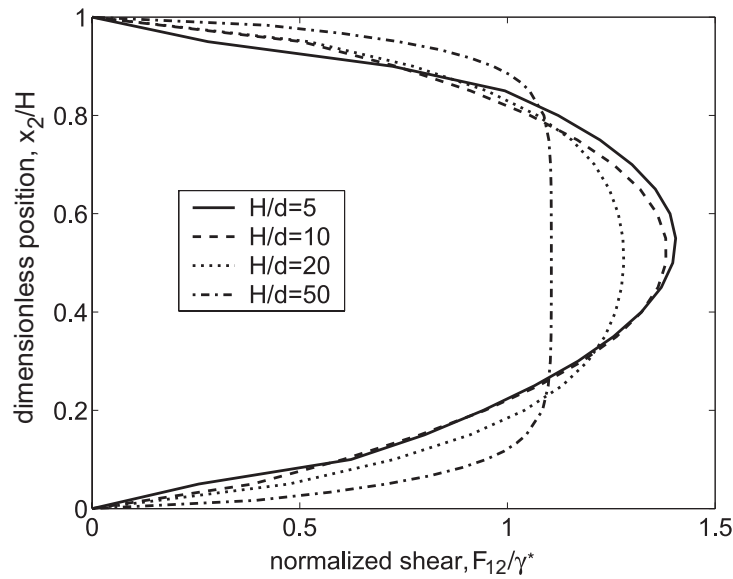


Figure 5.20: Shear strain distribution along the height of the strip for several values of H/d at the averaged prescribed shear $\gamma^* = 0.01$.

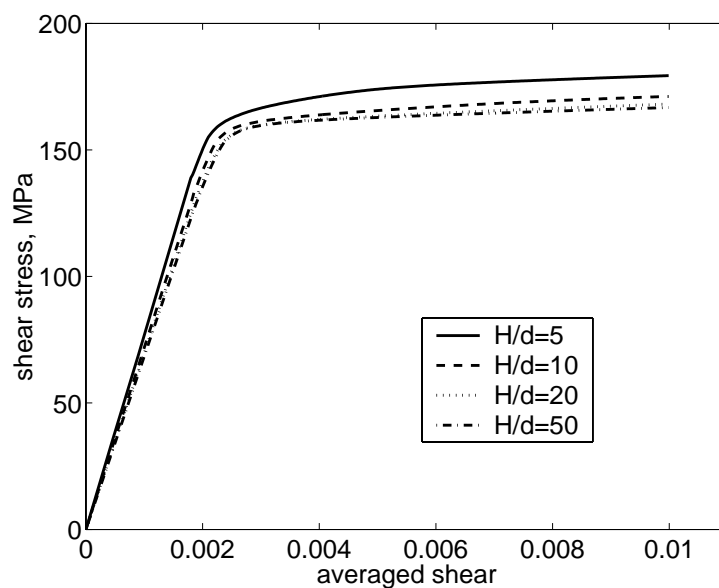


Figure 5.21: Overall shear stress-strain response of the strip obtained from the second-order computational homogenization modelling for several values of H/d .

shows the shear distributions over the strip (normalized by the averaged shear γ^*) at four selected values of the averaged prescribed strain γ^* in the range of 0.0025 to 0.01 for different ratios H/d . Clearly, the width of the boundary layer does not only depend on the ratio H/d , but also on the level of the prescribed averaged shear. At small values of the prescribed shear the boundary layer is relatively thin, while it widens as the loading progresses. However, after having reached a certain level of loading the thickness of the boundary layer does not evolve further. Note that the “peaks” observed in the shear profile for $H/d = 50$ at a prescribed shear $\gamma^* = 0.0025$ are purely of a numerical nature and are due to an element size inappropriate to resolve the high deformation

gradients occurring near the boundary. Obviously, these “peaks” can be eliminated by mesh refinement.

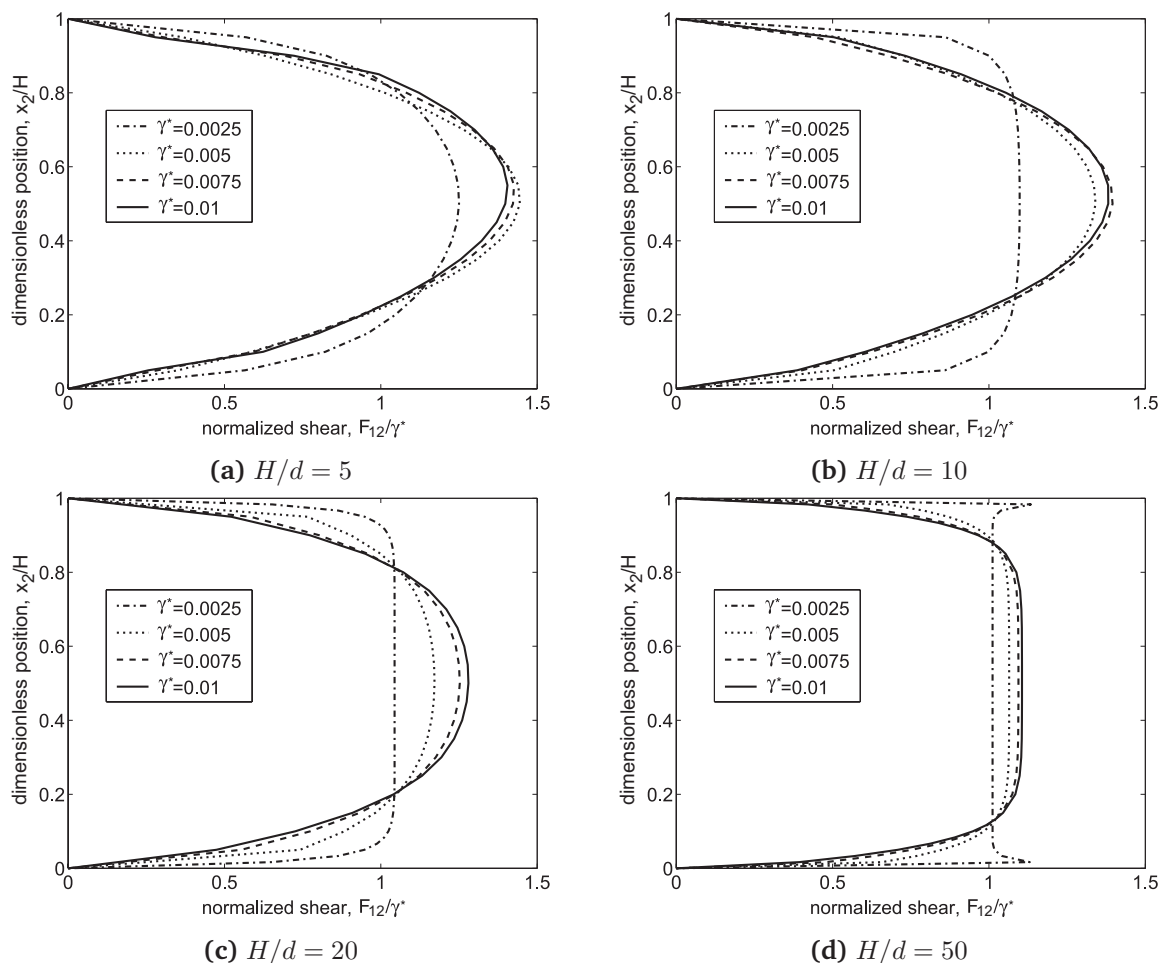


Figure 5.22: Shear strain distributions along the height of the strip at various values of the averaged shear γ^* for several ratios H/d .

The evolution of the shear profiles with ongoing loading may be related to the formation of microstructural shear bands. Figure 5.23 illustrates the development of a shear band in the microstructural unit cell located near $X_2 = H/2$ for the case $H/d = 20$. As can be seen, at small values of the averaged shear (e.g. $\gamma^* = 0.0025$) the microstructural cell is deformed only slightly and the overall deformation of the cell can be characterized as almost uniform shear (Figure 5.23a). This corresponds to the macroscopic shear profile in Figure 5.22c with a relatively thin boundary layer and a substantial region of uniform deformation across the macroscopic strip. With increasing macroscopic shear a microstructural shear band starts to develop between the voids. At the macrolevel this corresponds to an extension of the boundary layer. Finally, as the shear band across the unit cell is fully developed, further deformation of the microstructural cell is almost completely realized through plastic yielding within this band. As a result the macroscopic shear profile does not alter its geometry anymore upon further loading (at least not in the range of the macroscopic deformation considered).

Figure 5.24 shows the deformed macroscopic finite element meshes (displacements are 10 times magnified to emphasize the boundary layers) and the distribution of the equivalent plastic strain in the three microstructural unit cells corresponding to three

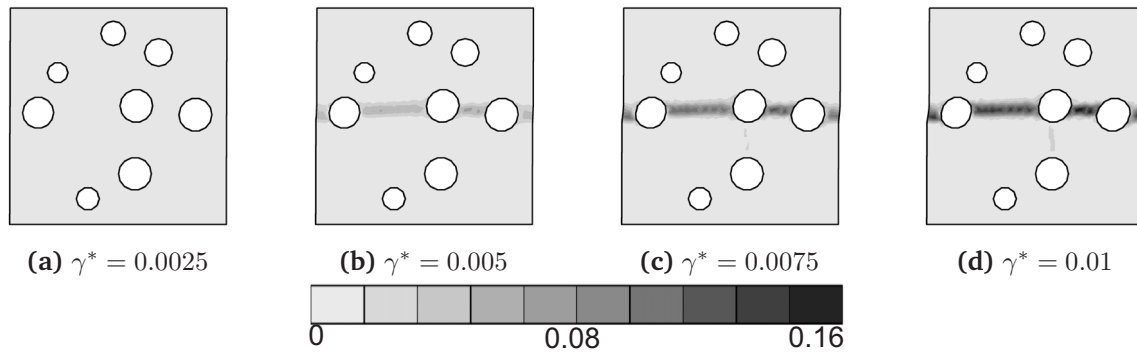


Figure 5.23: Development of a shear band in the microstructural unit cell located near $X_2 = H/2$ for a ratio $H/d = 20$ at increasing values of the prescribed macroscopic shear γ^* ; distribution of the equivalent plastic strain.

different points along the macroscopic layer. Figure 5.24a applies for the case $H/d = 5$ and Figure 5.24b for $H/d = 50$, both at a prescribed shear $\gamma^* = 0.01$. The constraining conditions along the boundary of the macroscopic strip result in a very small amount of deformation in the microstructural cells close to the boundary. The macroscopic shear is mostly accommodated through the formation of microstructural shear bands in the bulk of the strip. As has been pointed out already, for $H/d = 5$ the shear profile is non-uniform across the whole height of the strip. At the microscale this is reflected by a varying amount of deformation of the unit cells with varying macroscopic locations. The microscopic equivalent plastic strain concentration is considerably higher in the unit cell near the center line of the macroscopic strip, than in a unit cell further away from the center, see Figure 5.24a. On the other hand, in case of $H/d = 50$, the deformation profile shows a region of uniform shear (as can be seen also in Figure 5.22d). Consequently, at the microstructural level it can also be observed that the microstructural unit cells within this region are in a comparable state of loading.

Finally, it is remarked that the formation of boundary layers in a metallic single crystal strip has been intensively investigated by Shu et al. (2001). The results obtained in this reference and in the present work cannot be directly compared due to fundamentally different underlying physical mechanisms. Dislocation based simulations typically involve dislocation slip and formation of dislocation pile-ups against a constrained boundary (where dislocation slip is prescribed to vanish). In the present analysis the occurrence of microstructural shear bands between voids in the isotropic elasto-plastic matrix material and the appearance of a boundary layer, originates from the prescribed higher-order boundary conditions and the interaction between voids. However, some qualitative comparison of results can still be made. In both cases (i.e. dislocation dynamics simulations by Shu et al. (2001) and the present second-order computational homogenization analysis) a comparable size effect and a dependence of the shear strain profiles on a microstructural length scale parameter, as well as the evolution of the deformation profile with increasing prescribed shear, have been observed. It has additionally been shown by Shu et al. (2001), that the strain-gradient plasticity theories generally capture the other effects, but do not always predict the thickening of the boundary layer with increasing strain.

The example discussed in this section, despite its simplicity, clearly demonstrated the ability of the second-order computational homogenization scheme to capture higher-

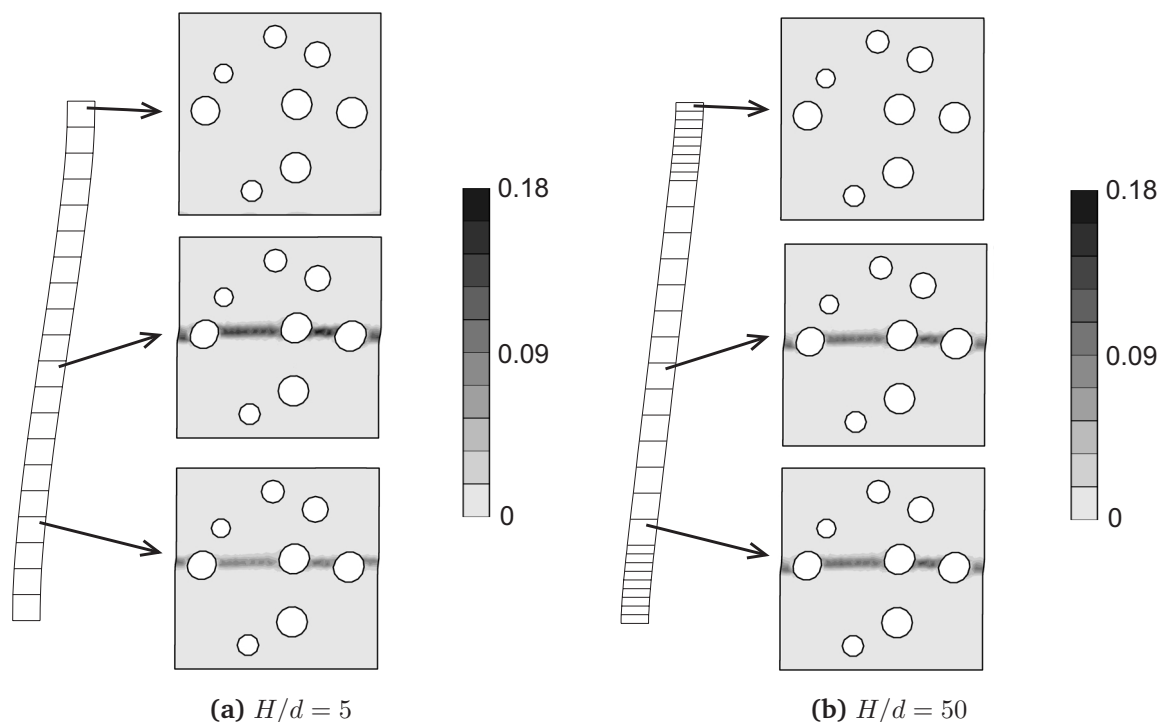


Figure 5.24: The deformed macroscopic mesh (displacements are 10 times magnified) and the distribution of the equivalent plastic strain in the deformed unit cells corresponding to three different points along the macroscopic layer at the prescribed shear $\gamma^* = 0.01$ for different ratios H/d .

order boundary effects (e.g. the effect of a constrained boundary). The value of the second-order computational homogenization as a natural way to retrieve a higher-order continuum response is also worth mentioning. Moreover, as has been illustrated by this example, a computational homogenization technique allows a direct investigation of the relation between a macroscopically observed response and microstructural phenomena (up to the scale at which they are modelled). It is also remarked that the present implementation of a second-order continuum with an underlying microstructure reveals qualitatively all the features of strain gradient plasticity for the shear layer problem. This might suggest that the second-order approximation along with its enriched boundary conditions is the adequate method to resolve this type of problems.

Chapter 6

Conclusions and recommendations

The multi-phase nature of almost all technological and biological materials and the increased necessity to exploit the complex micro-macro structure-property relations of heterogeneous materials, calls for advanced multi-scale modelling techniques. The objective of the present research was to develop an enhanced computational homogenization approach for a multi-scale analysis of non-linear deformation processes in (possibly evolving) multi-phase materials.

From time and costs viewpoints, performing straightforward experimental measurements on a number of material samples, with various phase properties, volume fractions and loading histories is a hardly feasible task. On the other hand, due to the usually enormous difference in length scales involved, it is impossible, for instance, to generate a finite element mesh that accurately represents the microstructure and concurrently allows to determine the numerical response of a macroscopic structural component within a reasonable amount of time on today's computational systems. To overcome this problem various homogenization techniques have been created to obtain an adequate constitutive model to be inserted at the macroscopic level. However, most of the homogenization methods developed are not suitable to deal with large deformations and complex loading paths nor do they account for evolving microstructures, moreover they do not allow the use of local failure criteria.

A promising alternative approach for the homogenization of engineering multi-phase materials is the so-called computational homogenization method, which was the main topic of this work. This technique is essentially based on the solution of nested boundary value problems, one for each scale. The most important characteristics of this solution strategy may be summarized as follows.

- On the macrolevel no constitutive assumptions are required, since the macroscopic constitutive response is numerically obtained from the solution of a microscale boundary value problem. This is especially advantageous when the microstructural constituents exhibit a non-linear and evolving thermo-mechanical behaviour, because in this case it is extremely difficult (if possible at all) to make well-motivated assumptions on the format of a macroscopic constitutive relation, and even more difficult to account for changes due to a microstructural evolution.

Additionally, as has been demonstrated in this work, macroscopic constitutive tangent operators, necessary for the solution of a macroscopic problem within, for example, a finite element framework, can be obtained easily from the microscopic overall stiffness matrix by static condensation. Importantly, consistency is preserved through this scale transition.

- The method deals with large deformations and large rotations on both microlevel and macrolevel in a straightforward way. The formulation of the micro-macro transition within a geometrically non-linear framework allows the modelling of heterogeneous structures under large deformations, which generally causes some difficulties using most of the other homogenization procedures. Moreover, possible anisotropy of a microstructure is correctly accounted for upon macroscopic finite rotations without any additional precautions.
- Different phases in the microstructure can be modelled with arbitrary non-linear constitutive models. The methodology is not restricted to any particular type of microstructural constitutive behaviour. Moreover, only the characteristics of each single phase and of the various interfaces are to be described. Fortunately, there is a lot more knowledge on the structure and physics of a single phase compared to the collective behaviour of multi-phase microstructures. As soon as a proper characterization of the microstructural phases and interfaces has been obtained, it can be directly included into the computational homogenization scheme without any limitations. For example, a common cause of material degradation on the macroscale like microstructural debonding can be analyzed in a straightforward manner, if the interface behaviour is appropriately modelled.
- The microscale formulation defines a standard boundary value problem, for which any appropriate solution technique may be applied. In the present work the finite element method has been used, however other classical and alternative approaches to the solution of boundary value problems may also be employed, e.g. the boundary element method, meshless methods, etc. The use of the standard finite element method for microstructural modelling may require extremely fine meshes around material interfaces and possibly remeshing. This may be necessary even at moderate macroscopic deformations, since in some cases the maximum microscopic strain may be an order of magnitude higher than the maximum macroscopic one. The micro-macro computational homogenization analysis coupled with the standard finite element method easily suffers from an extremely distorted microstructural mesh, which may limit the calculations unless remeshing is performed. In order to postpone (or avoid) remeshing, use of methods that do not require the meshing of the internal boundaries, but employ enriched finite element spaces, e.g. the extended finite element method, could be suggested. Approaches of this type have been recently applied for unit cell modelling (Strouboulis et al. (2000); Sukumar et al. (2001)). Incorporation of these techniques in the coupled computational homogenization analysis would certainly be beneficial.

Also it should be noted that, in general, the present computational homogenization approach is not restricted to cases where microstructural phases are modelled as a continuum. Among discrete microstructural models, which can be applied,

one finds atomistic models, molecular and discrete dislocation dynamics, lattice and cohesive zone models. For example, the use of a dislocation dynamics model on the microscale would allow to investigate the relation between the collective behaviour of dislocations and the phenomena observed at larger scales. Additionally, this would contribute to the validation of existing and the development of new dislocation based continuum models.

The classical (first-order) computational homogenization scheme fits entirely in a standard local continuum mechanics framework. The concepts of the first-order computational homogenization have been presented and elaborated in chapter 2. In the context of the first-order scheme, the macroscopic deformation (gradient) tensor is calculated for every material point of the macrostructure (e.g. an integration point of the macromesh within a finite element environment). This deformation tensor is used to formulate kinematic boundary conditions (usually periodic) to be imposed on the microstructural representative volume element (RVE) that is assigned to the macroscopic point. Upon the solution of the microstructural boundary value problem, the macroscopic stress tensor is obtained by averaging the resulting RVE stress field over the volume of the microstructural cell. From a macroscopic point of view, a (numerical) stress-strain relationship at every macroscopic point is readily obtained. The first-order computational homogenization technique proves to be a valuable tool in retrieving the macroscopic mechanical response of non-linear multi-phase materials.

However, there are a few severe limitations in the application of the first-order scheme, which in fact originate from the underlying assumption of locality at the macro-level. These limitations are summarized in the following.

- The first-order framework is completely insensitive to the absolute size of the microstructural constituents. Thus, size effects related to the absolute size at the microscale cannot be dealt with. Note that microstructural size effects (e.g. the Hall-Petch effect), which are to be modelled at the microscale itself, can be captured if an appropriate framework is used (e.g. a discrete model or a gradient dependent model).
- The characteristic wave length of the macroscopic loading must be large compared to the size of the microstructure, so that uniformity of the macroscopic (stress-strain) fields over the corresponding microstructural representative cell applies.
- If a macroscopic material point exhibits softening behaviour (due to geometrical or material softening of the attributed microstructural cell) the solution obtained from the first-order computational homogenization approach fully localizes according to the size of the elements used in the macromesh, i.e. the macroscopic boundary value problem becomes ill-posed leading to a mesh dependent macroscopic response. The example in section 5.2 has demonstrated this feature.

In order to eliminate these limitations, a novel second-order computational homogenization procedure has been proposed in this thesis (chapter 3). The second-order scheme is based on a proper incorporation of the macroscopic gradient of the deformation tensor into the kinematical micro-macro framework. The macroscopic stress tensor and the higher-order stress tensor are retrieved in a natural way, based on an extended version of the Hill-Mandel energy condition. A full second gradient continuum has

been obtained on the macroscale. The equilibrium formulation and the finite element implementation for the second gradient continuum has been presented in chapter 4.

The most important property of the second-order computational homogenization method is, in fact, that it incorporates the length scale of the second gradient continuum via the size of the microstructural representative cell, which is directly related to the size of the microstructural domain in which the basic microstructural deformation mechanisms occur. This allows the analysis of certain phenomena, not addressed within the first-order scheme, such as size effects and macroscopic localization. As has been observed from several microstructural analyses (section 5.1) the second-order computational homogenization framework is suitable to capture the change of the macroscopic response due to variations of the microstructural size as well as variations of the macroscopic gradient of the deformation. If the microstructural size becomes negligible with respect to the wave length of the macroscopic deformation field, the results obtained by the second-order modelling coincide with those of the first-order analysis. This important observation demonstrates that the second-order computational homogenization scheme is a natural extension of the first-order framework. Moreover, the second-order computational homogenization modelling of macroscopic localization provides mesh independent results with the width of the localization zone determined by the microstructurally related macroscopic length scale (section 5.2). Additionally, the second-order framework allows the modelling of surface layer effects via the incorporation of higher-order boundary conditions, as has been illustrated on the example in section 5.3. Finally it should be mentioned, that computational homogenization seems to make higher-order continuum modelling considerably easier. The second-order constitutive response, which is difficult to capture in a closed-format with many constitutive parameters to be quantified, is retrieved directly from a microstructural analysis.

Based on the comparative evaluation of the performance of the first-order and the second-order computational homogenization strategies the following recommendations may be given with respect to the practical use of one or another technique.

- As long as the principle of separation of scales continues to hold, i.e. macroscopic gradients remain small with respect to the size of the microstructure and no softening occurs at macroscopic points, the use of the first-order computational homogenization method is recommended.
- If microstructurally related macroscopic localization takes place, it is clear that a second-order technique is necessary to obtain physically meaningful results.
- Likewise, if the size of the microstructure is not negligible with respect to the geometry of the macrospecimen, the second-order approach should be used to capture the occurring geometrical size effects.
- Some of the higher-order boundary effects (e.g. the presence of boundary layers) also can be analyzed within the second-order framework.
- Moreover, if the microstructural constitutive response is gradient-sensitive, the second-order computational homogenization framework ensures that a macroscopic gradient is passed to the microscale. For example, discrete models often show gradient-sensitivity (e.g. dislocation models, where the effect of geometrically necessary dislocations is triggered through the gradients of the plastic deformation). As long as the phases are modelled using gradient-insensitive continuum

approaches, this major advantage of the second-order framework will not become visible. Typically, linking advanced fine scale models in which gradients generally have a role through the discrete nature of matter, to a coarse scale cannot be done without a higher-order homogenization framework.

However, when using the second-order computational homogenization scheme one should carefully validate the underlying assumption of a linear variation of the macroscopic deformation field over the representative microstructural cell. If this condition is strongly violated (i.e. if the macroscopic fields vary strongly on the scale of the microstructural constituents) a second-order computational homogenization scheme does not lead to an accurate approximation. In such cases the analysis should be performed by embedded scales instead.

The main objection against the use of coupled micro-macro computational homogenization strategies for practical problems, often stated in the literature, is related to the significantly larger computation time compared to the solution time of a macroscopic problem with closed-form homogenized constitutive equations. Certainly, a coupled analysis at higher computational costs should be performed only if an added value is provided, e.g. (i) in case of a geometrically and/or physically non-linear microstructural response; (ii) in case of evolving microstructures; (iii) if not only the macroscopic response, but also information on the local microstructural fields (e.g. for a local failure criterion) is of interest; (iv) in the cases that second-order computational homogenization is significantly easier than closed-form homogenization towards a higher-order continuum (especially in the non-linear regime). Moreover, the value of computational homogenization approaches to validate other homogenization methods and microstructurally based constitutive models should not be underestimated.

Furthermore, the calculation time required for a coupled numerical analysis may be substantially reduced by the use of parallel computations. One of the possible parallel implementation schemes has been presented in this work. Another option is selective usage, where non-critical regions are modelled by continuum closed-form homogenized constitutive relations (or by the constitutive tangents derived from the microstructure in case an incremental update of these tangents can be omitted, e.g. if the material hardly evolves or unloads) while in critical regions a multi-scale analysis of the microstructure is fully performed.

It should also be mentioned, that, compared to the first-order framework, in the second-order computational homogenization the only additional computational effort is the solution of the higher-order equilibrium problem on the macrolevel, since the microstructural boundary value problem remains classical. The higher computational requirements for the numerical solution of the second gradient continuum problem are mostly related to the increased number of degrees of freedom per node in a finite element mesh. For example, the simplest element for the second gradient continuum developed in chapter 4 has 36 degrees of freedom. This issue may possibly be resolved by use of the continuous/discontinuous Galerkin method recently introduced by Engel et al. (2002). The applicability of this approach within the second-order computational homogenization framework, however, still has to be evaluated.

Undoubtedly, many aspects, especially those related to the newly developed second-order computational homogenization, still need to be explored. Among them is the assessment of macroscopic higher-order boundary conditions based on the response of the microstructural behaviour close to the boundary and a better understanding of

the relation between the size of the microstructural representative volume element and the length scale of the macroscopic higher-order continuum, introduced via the scale transition. Extension of the second-order computational homogenization to include a higher-order continuum at the microlevel is also possible. This would allow to bridge the length scale gap between micromechanical models, capturing well the fine scale physical behaviour valid in micron-sized domains, and engineering problems that are formulated on meter-sized domains.

Despite the required computational efforts, multi-scale computational homogenization strategies seem to be a versatile tool to establish micro-macro structure-property relations in materials, where the collective behaviour of an evolving multi-phase heterogeneous structure cannot be predicted by any other method.

Appendix A

Constitutive models

In this appendix the constitutive models used for the modelling of microstructural constituents in various numerical examples throughout the dissertation are briefly summarized.

A.1 Compressible Neo-Hookean model

In the isotropic compressible hyperelastic Neo-Hookean model the constitutive relation is given by

$$\boldsymbol{\tau} = K(J - 1)\mathbf{I} + G\bar{\mathbf{B}}^d, \quad (\text{A.1})$$

where $\boldsymbol{\tau} = J\boldsymbol{\sigma}$ denotes the Kirchhoff stress tensor, $J = \det(\mathbf{F})$ the volume ratio, $\bar{\mathbf{B}}^d$ the deviator of the isochoric left Cauchy-Green (Finger) tensor $\bar{\mathbf{B}} = J^{-2/3}\mathbf{B}$ with $\mathbf{B} = \mathbf{F} \cdot \mathbf{F}^c$. The material parameters are the bulk modulus K and the shear modulus G .

A.2 Elasto-plastic model

In this hypo-elasto-plastic model the deformation rate tensor $\mathbf{D} = \frac{1}{2}((\nabla\vec{v})^c + \nabla\vec{v})$ (with \vec{v} the velocity of a material point) is additively decomposed in an elastic part \mathbf{D}_e and a plastic part \mathbf{D}_p

$$\mathbf{D} = \mathbf{D}_e + \mathbf{D}_p. \quad (\text{A.2})$$

The elastic part \mathbf{D}_e is coupled to the Cauchy stress $\boldsymbol{\sigma}$ by the hypo-elastic relation

$$\overset{\circ}{\boldsymbol{\sigma}} = {}^4\mathbf{C} : \mathbf{D}_e, \quad (\text{A.3})$$

where a superimposed circle denotes the objective Jaumann rate. The fourth-order tensor ${}^4\mathbf{C}$ is the usual isotropic elastic Hookean material tensor

$${}^4\mathbf{C} = \frac{\nu E}{(1 + \nu)(1 - 2\nu)}\mathbf{\Pi} + \frac{E}{1 + \nu}{}^4\mathbf{I}, \quad (\text{A.4})$$

with E Young's modulus and ν Poisson's ratio.

Deformation increments can be either elastic or elasto-plastic. A yield function f is used to determine whether elastic or elasto-plastic deformation takes place. The deformation rate in a material point is elastic if elastic loading ($f < 0$) or elastic unloading ($\dot{f} < 0$) occurs. During elasto-plastic deformation $f = 0$ and $\dot{f} = 0$ apply (the latter condition is known as the consistency relation).

The von Mises yield function, used in the present work, is given by

$$f(\boldsymbol{\sigma}, \bar{\epsilon}_p) = \bar{\sigma}^2 - \sigma_y^2, \quad (\text{A.5})$$

in which the equivalent von Mises stress is defined in the standard way according to

$$\bar{\sigma} = \sqrt{\frac{3}{2} \boldsymbol{\sigma}^d : \boldsymbol{\sigma}^d}. \quad (\text{A.6})$$

The current yield stress $\sigma_y = \sigma_y(\bar{\epsilon}_p)$ is a given function (hardening relation) of the equivalent plastic strain $\bar{\epsilon}_p$, which is defined by the following evolution equation

$$\dot{\bar{\epsilon}}_p = \sqrt{\frac{2}{3} \mathbf{D}_p^d : \mathbf{D}_p^d}. \quad (\text{A.7})$$

The plastic deformation rate is given by the associated flow rule, which can be written as

$$\mathbf{D}_p = \frac{3\dot{\bar{\epsilon}}_p}{2\sigma_y} \boldsymbol{\sigma}^d. \quad (\text{A.8})$$

A.3 Bodner-Partom model

The modified version of the elasto-visco-plastic Bodner-Partom model, used in the present work, incorporates a stress dependent viscosity, initially proposed by Bodner and Partom (1975), supplemented with a hardening contribution to describe the strain rate dependent yield and post-yield behaviour of metals (at elevated temperatures). In the present version this Bodner-Partom viscosity is implemented in the framework of a generalized Leonov model proposed by Baaijens (1991), which is a compressible version of the model established by Leonov (1976).

Point of departure is the classical multiplicative decomposition of the total deformation into an elastic and a plastic contribution, the latter assumed isochoric. The elastic deformation tensor \mathbf{F}_e is related to the Kirchhoff stress tensor $\boldsymbol{\tau} = J\boldsymbol{\sigma}$ according to an isotropic compressible Neo-Hookean relationship

$$\boldsymbol{\tau} = K(J - 1)\mathbf{I} + G\bar{\mathbf{B}}_e^d, \quad (\text{A.9})$$

where $J = \det(\mathbf{F}_e)$ is the volume change ratio, $\bar{\mathbf{B}}_e^d$ the deviator of the isochoric left Cauchy-Green tensor $\bar{\mathbf{B}}_e = J^{-2/3}\mathbf{B}_e$ with $\mathbf{B}_e = \mathbf{F}_e \cdot \mathbf{F}_e^c$, K the bulk modulus, and G the shear modulus. The dissipative plastic deformation rate tensor \mathbf{D}_p is related to the deviator of the Cauchy stress tensor $\boldsymbol{\sigma}^d$ according to a generalized Newtonian flow rule

$$\mathbf{D}_p = \frac{\boldsymbol{\sigma}^d}{2\eta}, \quad (\text{A.10})$$

with the stress dependent viscosity η defined as

$$\eta = \frac{\bar{\sigma}}{\sqrt{12}\Gamma_0} \exp\left(\frac{1}{2} \left[\frac{Z}{\bar{\sigma}}\right]^{2n}\right), \quad (\text{A.11})$$

where the equivalent von Mises stress $\bar{\sigma}$ is defined by (A.6). The material parameters Γ_0 and n reflect the smoothness of the elastic-to-plastic transition and the strain rate sensitivity, respectively. The state variable Z controls the hardening as the resistance to plastic flow, which is defined here by the following evolution equation

$$Z = Z_1 + (Z_0 - Z_1)e^{-m\bar{\epsilon}_p}, \quad (\text{A.12})$$

where the constants Z_0 and Z_1 denote the lower and upper bounds of Z , respectively, and m is a material constant controlling the rate of hardening. The internal variable $\bar{\epsilon}_p$ represents the equivalent plastic strain, which is defined according to the evolution equation (A.7).

A summary of this model and the material parameter identification procedure may be found in van der Aa et al. (2000).

Bibliography

- Aifantis, E. C. (1984). On the microstructural origin of certain inelastic models. *Trans. ASME J. Engrg. Mater. Tech.*, 106:326–330.
- Aifantis, E. C. (1992). On the role of gradients in the localization of deformation and fracture. *Int. J. Eng. Sci.*, 30:1279–1299.
- Amanatidou, E. and Aravas, A. (2002). Mixed finite element formulations of strain-gradient elasticity problems. *Comput. Methods Appl. Mech. Engrg.*, 191:1723–1751.
- Baaijens, F. P. T. (1991). Calculation of residual stresses in injection-molded products. *Rheol. Acta*, 30:284–299.
- Babuška, I. (1973). The finite element method with Lagrange multipliers. *Numer. Math.*, 20:179–192.
- Bao, G., Hutchinson, J. W., and McMeeking, R. M. (1991). Plastic reinforcement of ductile materials against plastic flow and creep. *Acta Metall. Mater.*, 39(8):1871–1882.
- Barsoum, M. W., Kangutkar, P., and Wang, A. S. D. (1992). Matrix crack initiation in ceramic matrix composites. Part I: Experiments and test results. *Compos. Sci. Tech.*, 44:257–269.
- Bažant, Z. P. and Pijaudier-Cabot, G. (1988). Nonlocal continuum damage, localization instability and convergence. *J. Appl. Mech.*, 55:287–293.
- Begley, M. R. and Hutchinson, J. W. (1998). The mechanics of size-dependent indentation. *J. Mech. Phys. Solids*, 46(10):2049–2068.
- Belytschko, T., Liu, W. K., and Moran, B. (2000). *Nonlinear finite elements for continua and structures*. Wiley, Chichester.
- Bensoussan, A., Lionis, J.-L., and Papanicolaou, G. (1978). *Asymptotic analysis for periodic structures*. North-Holland, Amsterdam.
- Bodner, S. R. and Partom, Y. (1975). Constitutive equation for elastic-viscoplastic strain-hardening materials. *J. Appl. Mech.*, 42:385–389.
- Boutin, C. (1996). Microstructural effects in elastic composites. *Int. J. Solids Structures*, 33(7):1023–1051.

- Bouyge, F., Jasiuk, I., and Ostoja-Starzewski, M. (2001). A micromechanically based couple-stress model of an elastic two-phase composite. *Int. J. Solids Structures*, 38:1721–1735.
- Brand, L. (1947). *Vector and tensor analysis*. John Wiley & Sons.
- Brezzi, F. and Bathe, K. J. (1990). A discourse on the stability conditions for mixed finite element formulations. *Comput. Methods Appl. Mech. Engrg.*, 82:27–57.
- Brockenbrough, J. R., Suresh, S., and Wienecke, H. A. (1991). Deformation of metal-matrix composites with continuous fibers: geometrical effect of fiber distribution and shape. *Acta Metall. Mater.*, 39(5):735–752.
- Budiansky, B. (1965). On the elastic moduli of some heterogeneous materials. *J. Mech. Phys. Solids*, 13:223–227.
- Chambon, R., Caillerie, D., and Matsuchima, T. (2001). Plastic continuum with microstructure, local second gradient theories for geomaterials: localization studies. *Int. J. Solids Structures*, 38:8503–8527.
- Chen, J. Y., Huang, Y., Hwang, K. C., and Xia, Z. C. (2000). Plane-stress deformation in strain gradient plasticity. *J. Appl. Mech.*, 67:105–111.
- Christensen, R. M. and Lo, K. H. (1979). Solutions for effective shear properties in three phase sphere and cylinder models. *J. Mech. Phys. Solids*, 27:315–330.
- Christman, T., Needleman, A., and Suresh, S. (1989). An experimental and numerical study of deformation in metal-ceramic composites. *Acta Metall.*, 37(11):3029–3050.
- Cook, R. D., Malkus, D. S., and Plesha, M. E. (1989). *Concepts and applications of finite element analysis*. Wiley, Chichester.
- Cosserat, E. and Cosserat, F. (1909). *Théorie des Corps Déformables*. Hermann & Fils, Paris.
- de Borst, R. (1991). Simulation of strain localization: a reappraisal of the Cosserat continuum. *Eng. Comp.*, 8:317–332.
- de Borst, R. and Mühlhaus, H.-B. (1992). Gradient-dependent plasticity: formulation and algorithmic aspects. *Int. J. Numer. Meth. Engrg.*, 35:521–539.
- de Borst, R. and Pamin, J. (1996). Some novel developments in finite element procedures for gradient-dependent plasticity and finite elements. *Int. J. Numer. Meth. Engrg.*, 39:2477–2505.
- de Borst, R., Sluys, L. J., Mühlhaus, H.-B., and Pamin, J. (1993). Fundamental issues in finite element analysis of localization of deformation. *Eng. Comp.*, 10:99–121.
- de Felice, G. and Rizzi, N. (1997). Homogenization for materials with microstructure. In *Recent advances in solids/structures and application of metallic materials*, PVP-Vol. 369, pages 33–38. ASME.
- Devries, F., Dumontet, H., Duvaut, G., and Lene, F. (1989). Homogenization and damage for composite structures. *Int. J. Numer. Meth. Engrg.*, 27:285–298.
- Drugan, W. J. and Willis, J. R. (1996). A micromechanics-based nonlocal constitutive equation and estimates of representative volume element size for elastic composites. *J. Mech. Phys. Solids*, 44(4):497–524.

- Dvorkin, E. N. (2001). On the convergence of incompressible finite element formulations. The patch test and the inf-sup condition. *Eng. Comp.*, 18:539–556.
- Engel, G., Garikipati, K., Hughes, T. J. R., Larson, M. G., Mazzei, L., and Taylor, R. L. (2002). Continuous/discontinuous finite element approximations of fourth-order elliptic problems in structural and continuum mechanics with applications to thin beams and plates, and strain gradient elasticity. *Comput. Meth. Appl. Mech. Engrg.*, 191:3669–3750.
- Engelen, R. A. B., Geers, M. G. D., and Baaijens, F. P. T. (2002). Nonlocal implicit gradient-enhanced softening plasticity. *Int. J. Plasticity*. In press.
- Eringen, A. C. (1964). Mechanics of micromorphic materials. In Görtler, H., editor, *Proc. 11th Int. Congress of Appl. Mech.*, pages 131–138, New York. Springer-Verlag.
- Eringen, A. C. (1966). Linear theory of micropolar elasticity. *J. Math. Mech.*, 15(6):909–923.
- Eshelby, J. D. (1957). The determination of the field of an ellipsoidal inclusion and related problems. *Proc. R. Soc. Lond A*, 241:376–396.
- Feyel, F. and Chaboche, J.-L. (2000). FE² multiscale approach for modelling the elastoviscoplastic behaviour of long fiber SiC/Ti composite materials. *Comput. Methods Appl. Mech. Engrg.*, 183:309–330.
- Fish, J., Yu, Q., and Shek, K. (1999). Computational damage mechanics for composite materials based on mathematical homogenisation. *Int. J. Numer. Meth. Engrg.*, 45:1657–1679.
- Fleck, N. A. and Hutchinson, J. W. (1993). A phenomenological theory for strain gradient effects in plasticity. *J. Mech. Phys. Solids*, 41(12):1825–1857.
- Fleck, N. A. and Hutchinson, J. W. (1997). Strain gradient plasticity. *Adv. Appl. Mech.*, 33:295–361.
- Fleck, N. A., Muller, G. M., Ashby, M. E., and Hutchinson, J. W. (1994). Strain gradient plasticity: theory and experiment. *Acta Metall. Mater.*, 42(2):475–487.
- Forest, S., Barbe, F., and Cailletaud, G. (2000). Cosserat modelling of size effects in the mechanical behaviour of polycrystals and multi-phase materials. *Int. J. Solids Structures*, 37:7105–7126.
- Forest, S., Dendievel, R., and Canova, G. R. (1999). Estimating the overall properties of heterogeneous Cosserat materials. *Model. Simul. Mater. Sci. Eng.*, 7:829–840.
- Forest, S., Pradel, F., and Sab, K. (2001). Asymptotic analysis of heterogeneous Cosserat media. *Int. J. Solids Structures*, 38:4585–4608.
- Forest, S. and Sab, K. (1998). Cosserat overall modeling of heterogeneous materials. *Mech. Res. Comm.*, 25(4):449–454.
- Gao, H., Huang, Y., Nix, W. D., and Hutchinson, J. W. (1999). Mechanism-based strain gradient plasticity – I. Theory. *J. Mech. Phys. Solids*, 47:1239–1263.
- Geers, M. G. D., de Borst, R., Brekelmans, W. A. M., and Peerlings, R. H. J. (1998). Strain-based transient-gradient damage model for failure analyses. *Comput. Meth. Appl. Mech. Engrg.*, 160(1-2):133–154.

- Geers, M. G. D., Kouznetsova, V., and Brekelmans, W. A. M. (2000a). Constitutive approaches for the multi-level analysis of the mechanics of microstructures. In *Proceedings of 5th National Congress on Theoretical and Applied Mechanics*, pages 179–182, Louvain-la-Neuve, Belgium.
- Geers, M. G. D., Kouznetsova, V., and Brekelmans, W. A. M. (2001a). Gradient-enhanced computational homogenization for the micro-macro scale transition. *J. Phys. IV*, 11:145–152.
- Geers, M. G. D., Kouznetsova, V., and Brekelmans, W. A. M. (2001b). Micro-macro scale transitions for engineering materials in the presence of size effects. In Wall, W. A., Bletzinger, K.-U., and Schweizerhof, K., editors, *Trends in Computational Structural Mechanics*, pages 118–127, CIMNE, Barcelona, Spain.
- Geers, M. G. D., Kouznetsova, V., and Brekelmans, W. A. M. (2001c). Non-local macroscopic constitutive behaviour for the incorporation of microstructural mechanics. In *Proceedings of the 2nd European Conference on Computational Mechanics*, on CD-ROM, Cracow, Poland.
- Geers, M. G. D., Kouznetsova, V., and Brekelmans, W. A. M. (2002a). Multi-scale mechanics in micro-electronics: a paradigm in miniaturisation. In Ernst, L. J., Zhang, G. Q., Dudek, R., and de Saint Leger, O., editors, *Proceedings of EuroSIME*, pages 133–139, Paris, France.
- Geers, M. G. D., Kouznetsova, V., and Brekelmans, W. A. M. (2002b). Perspectives in multi-scale modelling of composite and heterogeneous materials upon localization. In Mang, H. A., Rammerstorfer, F. G., and Eberhardsteiner, J., editors, *Proceedings of the 5th World Congress on Computational Mechanics*, <http://wccm.tuwien.ac.at>, Vienna, Austria.
- Geers, M. G. D., Kouznetsova, V., Brekelmans, W. A. M., and Peerlings, R. H. J. (2000b). Gradient-enhanced macroscopic constitutive principles for the mechanical description of microstructures. In Michel, B., Winkler, T., Werner, M., and Fecht, H., editors, *Micro Materials: Proceedings of MicroMat*, pages 734–737, Berlin, Germany.
- Geist, A., Beguelin, A., Dongarra, J. J., Jiang, W., Manchek, R., and Sunderam, V. (1994). *PVM: parallel virtual machine. A user's guide and tutorial for networked parallel computing*. MIT Press, Cambridge.
- Germain, P. (1973). The method of virtual power in continuum mechanics. Part 2: Microstructure. *SIAM J. Appl. Math.*, 25(3):556–575.
- Ghosh, S., Lee, K., and Moorthy, S. (1995). Multiple scale analysis of heterogeneous elastic structures using homogenisation theory and Voronoi cell finite element method. *Int. J. Solids Structures*, 32(1):27–62.
- Ghosh, S., Lee, K., and Moorthy, S. (1996). Two scale analysis of heterogeneous elastic-plastic materials with asymptotic homogenisation and Voronoi cell finite element model. *Comput. Methods Appl. Mech. Engrg.*, 132:63–116.
- Ghosh, S., Lee, K., and Raghavan, P. (2001). A multi-level computational model for multi-scale damage analysis in composite and porous materials. *Int. J. Solids Structures*, 38:2335–2385.

- Govaert, L. E., Timmermans, P. H. M., and Brekelmans, W. A. M. (2000). The influence of intrinsic strain softening on strain localization in polycarbonate: modeling and experimental validation. *J. Engrg. Mat. Technol.*, 122:177–185.
- Green, A. E. and Rivlin, R. S. (1964). Multipolar continuum mechanics. *Arch. Ration. Mech. Anal.*, 17:113–147.
- Guedes, J. M. and Kikuchi, N. (1990). Preprocessing and postprocessing for materials based on the homogenization method with adaptive finite element methods. *Comput. Methods Appl. Mech. Engrg.*, 83:143–198.
- Hall, R. A. (1991). Computer modelling of rubber-toughened plastics: random placement of monosized core-shell particles in a polymer matrix and interparticle distance calculations. *J. Mater. Sci.*, 26:5631–5636.
- Hashin, Z. (1962). The elastic moduli of heterogeneous materials. *J. Appl. Mech.*, 29:143–150.
- Hashin, Z. (1983). Analysis of composite materials. A survey. *J. Appl. Mech.*, 50:481–505.
- Hashin, Z. and Shtrikman, S. (1963). A variational approach to the theory of the elastic behaviour of multiphase materials. *J. Mech. Phys. Solids*, 11:127–140.
- Herrmann, L. R. (1983). Mixed finite elements for couple-stress analysis. In Atluri, S. N., Gallagher, R. H., and Zienkiewicz, O. C., editors, *Hybrid and mixed finite element methods*, pages 1–17. John Wiley & Sons Ltd.
- Hill, R. (1963). Elastic properties of reinforced solids: some theoretical principles. *J. Mech. Phys. Solids*, 11:357–372.
- Hill, R. (1965). A self-consistent mechanics of composite materials. *J. Mech. Phys. Solids*, 13:213–222.
- Hill, R. (1984). On macroscopic effects of heterogeneity in elastoplastic media at finite strain. *Math. Proc. Camb. Phil. Soc.*, 95:481–494.
- Hollister, S. J. and Kikuchi, N. (1992). A comparison of homogenization and standard mechanics analysis for periodic porous composites. *Comput. Mech.*, 10:73–95.
- Huang, Y., Gao, H., Nix, W. D., and Hutchinson, J. W. (2000). Mechanism-based strain gradient plasticity – II. Analysis. *J. Mech. Phys. Solids*, 48:99–128.
- Huet, C. (1990). Application of variational concepts to size effects in elastic heterogeneous bodies. *J. Mech. Phys. Solids*, 38(6):813–841.
- Huet, C. (1999). Coupled size and boundary-condition effects in viscoelastic heterogeneous and composite bodies. *Mech. Mater*, 31:787–829.
- Koiter, W. T. (1964). Couple-stresses in the theory of elasticity. *Proc. K. Ned. Acad. Wet. (B)*, 67(1):17–44.
- Kouznetsova, V., Brekelmans, W. A. M., and Baaijens, F. P. T. (2000a). Micro-macro modeling of heterogeneous materials. In *Proceedings of the European Congress on Computational Methods in Applied Sciences and Engineering ECCOMAS*, on CD-ROM, CIMNE, Barcelona, Spain.

- Kouznetsova, V., Brekelmans, W. A. M., and Baaijens, F. P. T. (2001a). An approach to micro-macro modeling of heterogeneous materials. *Comput. Mech.*, 27:37–48.
- Kouznetsova, V., Brekelmans, W. A. M., de Vree, J. H. P., and Baaijens, F. P. T. (1999). A multi-level large strain analysis for forming. In Wunderlich, W., editor, *Proceedings of the European Conference on Computational Mechanics*, on CD-ROM, München, Germany.
- Kouznetsova, V., Brekelmans, W. A. M., and Geers, M. G. D. (2001b). Gradient-enhanced constitutive analysis of materials with incorporation of the microstructure. In *Proceedings of the 2nd European Conference on Computational Mechanics*, on CD-ROM, Cracow, Poland.
- Kouznetsova, V., Brekelmans, W. A. M., and Geers, M. G. D. (2001c). Gradient-enhanced framework for the constitutive analysis of microstructures at large deformations. In Habraken, A. M., editor, *Proceedings of the 4th international ESAFORM conference on Material Forming*, pages 449–452, Liege, Belgium.
- Kouznetsova, V., Brekelmans, W. A. M., Geers, M. G. D., and Baaijens, F. P. T. (2000b). Multi-level modelling of heterogeneous micro materials. In Michel, B., Winkler, T., Werner, M., and Fecht, H., editors, *Micro Materials: Proceedings of MicroMat*, pages 550–553, Berlin, Germany.
- Kouznetsova, V., Geers, M. G. D., and Brekelmans, W. A. M. (2002). Multi-scale constitutive modelling of heterogeneous materials with a gradient-enhanced computational homogenization scheme. *Int. J. Numer. Meth. Engrg.*, 54:1235–1260.
- Leonov, A. I. (1976). Non-equilibrium thermodynamics and rheology of viscoelastic polymer media. *Rheol. Acta*, 15:85–98.
- Mackay, R. A. (1990). Effect of fiber spacing on interfacial damage in a metal matrix composite. *Scripta Metall. Mater.*, 24:167–172.
- Matsushima, T., Chambon, R., and Caillerie, D. (2002). Large strain finite element analysis of a local second gradient model: application to localization. *Int. J. Numer. Meth. Engrg.*, 54:499–521.
- McHugh, P. E., Asaro, R. J., and Shin, C. F. (1993a). Computational modeling of metal matrix composite materials — II. Isothermal stress-strain behaviour. *Acta Metall. Mater.*, 41(5):1477–1488.
- McHugh, P. E., Asaro, R. J., and Shin, C. F. (1993b). Computational modeling of metal matrix composite materials — III. Comparison with phenomenological models. *Acta Metall. Mater.*, 41(5):1489–1499.
- Michel, J. C., Moulinec, H., and Suquet, P. (1999). Effective properties of composite materials with periodic microstructure: a computational approach. *Comput. Methods Appl. Mech. Engrg.*, 172:109–143.
- Miehe, C. (1996). Numerical computation of algorithmic (consistent) tangent moduli in large-strain computational inelasticity. *Comput. Methods Appl. Mech. Engrg.*, 134:223–240.
- Miehe, C. and Koch, A. (2002). Computational micro-to-macro transition of discretized microstructures undergoing small strain. *Arch. Appl. Mech.*, 72:300–317.

- Miehe, C., Schotte, J., and Schröder, J. (1999a). Computational micro-macro transitions and overall moduli in the analysis of polycrystals at large strains. *Comput. Mater. Sci.*, 16:372–382.
- Miehe, C., Schröder, J., and Schotte, J. (1999b). Computational homogenization analysis in finite plasticity. Simulation of texture development in polycrystalline materials. *Comput. Methods Appl. Mech. Engrg.*, 171:387–418.
- Mindlin, R. D. (1964). Micro-structure in linear elasticity. *Arch. Ration. Mech. Anal.*, 16:51–78.
- Mindlin, R. D. (1965). Second gradient of strain and surface-tension in linear elasticity. *Int. J. Solids Structures*, 1:417–438.
- Mindlin, R. D. and Eshel, N. N. (1968). On first strain-gradient theories in linear elasticity. *Int. J. Solids Structures*, 4:109–124.
- Mindlin, R. D. and Tiersten, H. F. (1962). Effects of couple-stress in linear elasticity. *Arch. Ration. Mech. Anal.*, 11:415–448.
- Mori, T. and Tanaka, K. (1973). Average stress in the matrix and average elastic energy of materials with misfitting inclusions. *Acta Metall.*, 21:571–574.
- Moulinec, H. and Suquet, P. (1998). A numerical method for computing the overall response of non-linear composites with complex microstructure. *Comput. Methods Appl. Mech. Engrg.*, 157:69–94.
- Nakamura, T. and Suresh, S. (1993). Effect of thermal residual stress and fiber packing on deformation of metal-matrix composites. *Acta Metall. Mater.*, 41(6):1665–1681.
- Nemat-Nasser, S. (1999). Averaging theorems in finite deformation plasticity. *Mech. Mater.*, 31:493–523.
- Nemat-Nasser, S. and Hori, M. (1993). *Micromechanics: overall properties of heterogeneous materials*. Elsevier, Amsterdam.
- Ostoja-Starzewski, M. (1998). Random field models of heterogeneous materials. *Int. J. Solids Structures*, 35(19):2429–2455.
- Ostoja-Starzewski, M. (1999). Scale effects in materials with random distributions of needles and cracks. *Mech. Mater.*, 31:883–893.
- Ostoja-Starzewski, M., Boccara, S. D., and Jasiuk, I. (1999). Couple-stress moduli and characteristic length of a two-phase composite. *Mech. Res. Comm.*, 26(4):387–396.
- Pecullan, S., Gibiansky, L. V., and Torquato, S. (1999). Scale effects on the elastic behavior of periodic and hierarchical two-dimensional composites. *J. Mech. Phys. Solids*, 47:1509–1542.
- Peerlings, R. H. J., de Borst, R., Brekelmans, W. A. M., and de Vree, J. H. P. (1996). Gradient-enhanced damage for quasi-brittle materials. *Int. J. Numer. Meth. Engrg.*, 39:3391–3403.
- Peerlings, R. H. J. and Fleck, N. A. (2001). Numerical analysis of strain gradient effects in periodic media. *J. Phys. IV*, 11:153–160.
- Ponte Castañeda, P. and Suquet, P. (1998). Nonlinear composites. *Adv. Appl. Mech.*, 34:171–302.

- Sanchez-Palencia, E. (1980). *Non-homogeneous media and vibration theory. Lecture notes in physics 127*. Springer-Verlag, Berlin.
- Schreyer, H. and Chen, Z. (1986). One-dimensional softening with localization. *J. Appl. Mech.*, 53:791–979.
- Shan, Z. and Gokhale, A. M. (2002). Representative volume element for non-uniform micro-structure. *Comp. Mat. Sci.*, 24:361–379.
- Shu, J. Y. and Barlow, C. Y. (2000). Strain gradient effects on microscopic strain field in a metal matrix composite. *Int. J. Plasticity*, 16:563–591.
- Shu, J. Y. and Fleck, N. A. (1998). The prediction of a size effect in microindentation. *Int. J. Solids Structures*, 35(13):1363–1383.
- Shu, J. Y. and Fleck, N. A. (1999). Strain gradient crystal plasticity: size-dependent deformation of bicrystals. *J. Mech. Phys. Solids*, 47:297–324.
- Shu, J. Y., Fleck, N. A., van der Giessen, E., and Needleman, N. (2001). Boundary layers in constrained plastic flow: comparison of nonlocal and discrete dislocation plasticity. *J. Mech. Phys. Solids*, 49:1361–1395.
- Shu, J. Y., King, W. E., and Fleck, N. A. (1999). Finite elements for materials with strain gradient effects. *Int. J. Numer. Meth. Engrg.*, 44:373–391.
- Smit, R. J. M. (1998). *Toughness of heterogeneous polymeric systems*. PhD thesis, Eindhoven University of Technology, Eindhoven, The Netherlands.
- Smit, R. J. M., Brekelmans, W. A. M., and Meijer, H. E. H. (1998). Prediction of the mechanical behaviour of non-linear heterogeneous systems by multi-level finite element modeling. *Comput. Methods Appl. Mech. Engrg.*, 155:181–192.
- Smit, R. J. M., Brekelmans, W. A. M., and Meijer, H. E. H. (1999). Prediction of the large-strain mechanical response of heterogeneous polymer systems: local and global deformation behaviour of a representative volume element of voided polycarbonate. *J. Mech. Phys. Solids*, 47:201–221.
- Smyshlyaev, V. P. and Cherednichenko, K. D. (2000). On rigorous derivation of strain gradient effects in the overall behaviour of periodic heterogeneous media. *J. Mech. Phys. Solids*, 48:1325–1357.
- Smyshlyaev, V. P. and Fleck, N. A. (1994). Bounds and estimates for linear composites with strain gradient effects. *J. Mech. Phys. Solids*, 42(12):1851–1882.
- Smyshlyaev, V. P. and Fleck, N. A. (1995). Bounds and estimates for the overall plastic behaviour of composites with strain gradient effects. *Proc. R. Soc. Lond. A*, 451:795–810.
- Smyshlyaev, V. P. and Fleck, N. A. (1996). The role of strain gradients in the grain size effect for polycrystals. *J. Mech. Phys. Solids*, 44(4):465–495.
- Strouboulis, T., Copps, K., and Babuška, I. (2000). The generalized finite element method: an example of its implementation and illustration of its performance. *Int. J. Numer. Meth. Engrg.*, 47:1401–1417.
- Sukumar, N., Chopp, D. L., Moës, N., and Belytschko, T. (2001). Modeling holes and inclusions by level sets in the extended finite-element method. *Comput. Meth. Appl. Mech. Engrg.*, 190:6183–6200.

- Suquet, P. M. (1985). Local and global aspects in the mathematical theory of plasticity. In Sawczuk, A. and Bianchi, G., editors, *Plasticity today: modelling, methods and applications*, pages 279–310, London. Elsevier Applied Science Publishers.
- Suresh, S., Mortensen, A., and Needleman, A., editors (1993). *Fundamentals of metal-matrix composites*. Butterworth-Heinemann, Boston.
- Svedberg, T. and Runesson, K. (1997). A thermodynamically consistent theory of gradient-regularized plasticity coupled to damage. *Int. J. Plasticity*, 13(6-7):669–696.
- Terada, K., Hori, M., Kyoya, T., and Kikuchi, N. (2000). Simulation of the multi-scale convergence in computational homogenization approach. *Int. J. Solids Structures*, 37:2285–2311.
- Terada, K. and Kikuchi, N. (1995). Nonlinear homogenization method for practical applications. In Ghosh, S. and Ostoja-Starzewski, M., editors, *Computational Methods in Micromechanics*, AMD-Vol. 212/MD-Vol. 62, pages 1–16. ASME.
- Terada, K. and Kikuchi, N. (2001). A class of general algorithms for multi-scale analysis of heterogeneous media. *Comput. Methods Appl. Mech. Engrg.*, 190:5427–5464.
- Tervoort, T. (1996). *Constitutive modelling of polymer glasses: finite, nonlinear viscoelastic behaviour of polycarbonate*. PhD thesis, Eindhoven University of Technology, Eindhoven, The Netherlands.
- Tolenado, A. and Murakami, H. (1987). A high-order mixture model for periodic particulate composites. *Int. J. Solids Structures*, 23:989–1002.
- Toupin, R. A. (1962). Elastic materials with couple-stress. *Arch. Ration. Mech. Anal.*, 11:385–414.
- Toupin, R. A. (1964). Theories of elasticity with couple-stress. *Arch. Ration. Mech. Anal.*, 17:85–112.
- Triantafyllidis, N. and Bardenhagen, S. (1996). The influence of scale size on the stability of periodic solids and the role of associated higher order gradient continuum models. *J. Mech. Phys. Solids*, 44(11):1891–1928.
- Tvergaard, V. (1990). Analysis of tensile properties for whisker-reinforced metal-matrix composites. *Acta Metall. Mater.*, 38(2):185–194.
- van der Aa, H. C. E., van der Aa, M. A. H., Schreurs, P. J. G., Baaijens, F. P. T., and van Veenen, W. J. (2000). An experimental and numerical study of the wall ironing process of polymer coated sheet metal. *Mech. Mater.*, 32:423–443.
- van der Sluis, O. (2001). *Homogenisation of structured elastoviscoplastic solids*. PhD thesis, Eindhoven University of Technology, Eindhoven, The Netherlands.
- van der Sluis, O., Schreurs, P. J. G., Brekelmans, W. A. M., and Meijer, H. E. H. (2000). Overall behaviour of heterogeneous elastoviscoplastic materials: effect of microstructural modelling. *Mech. Mater.*, 32:449–462.
- van der Sluis, O., Schreurs, P. J. G., and Meijer, H. E. H. (1999a). Effective properties of a viscoplastic constitutive model obtained by homogenisation. *Mech. Mater.*, 31:743–759.
- van der Sluis, O., Vosbeek, P. H. J., Schreurs, P. J. G., and Meijer, H. E. H. (1999b). Homogenization of heterogeneous polymers. *Int. J. Solids Structures*, 36:3193–3214.

- Vardoulakis, I. and Aifantis, E. C. (1991). A gradient flow theory of plasticity for granular materials. *Acta Mech.*, 87:197–217.
- Willis, J. R. (1981). Variational and related methods for the overall properties of composites. *Adv. Appl. Mech.*, 21:1–78.
- Xia, Z. C. and Hutchinson, J. W. (1996). Crack tip fields in strain gradient plasticity. *J. Mech. Phys. Solids*, 44(10):1621–1648.
- Yuan, X. and Tomita, Y. (2001). Effective properties of Cosserat composites with periodic microstructure. *Mech. Res. Comm.*, 28(3):265–270.
- Zervos, A., Papanastasiou, P., and Vardoulakis, I. (2001). A finite element displacement formulation for gradient elastoplasticity. *Int. J. Numer. Meth. Engrg.*, 50:1369–1388.
- Zhang, W. and Chen, D. P. (1997). The patch test conditions and some multivariable finite element formulations. *Int. J. Numer. Meth. Engrg.*, 40:3015–3032.
- Zhu, H. T., Zbib, H. M., and Aifantis, E. C. (1997). Strain gradients and continuum modeling of size effect in metal matrix composites. *Acta Mech.*, 121:165–176.
- Zienkiewicz, O. C. and Taylor, R. L. (1997). The finite element patch test revisited. A computer test for convergence, validation and error estimates. *Comput. Methods Appl. Mech. Engrg.*, 149:223–254.
- Zienkiewicz, O. C. and Taylor, R. L. (2000). *The Finite Element Method*. Arnold, London, 5th edition.

Samenvatting

De meeste materialen die worden geproduceerd en toegepast in de industrie zijn heterogeen op een of andere ruimtelijke schaal. Typische voorbeelden zijn metaallegeringen, poreuze media, polykristallijne materialen en composieten. De verschillende fasen waaruit dergelijke materialen bestaan vormen een microstructuur. De (eventueel veranderende) grootte, vorm, fysische eigenschappen en ruimtelijke verdeling van de microstructurele bestanddelen bepalen in hoge mate het macroscopische, globale gedrag van deze meerfasige materialen.

Het macroscopische gedrag van heterogene materialen kan worden voorspeld door middel van een aantal homogenisatiemethoden. De meeste van deze technieken zijn echter niet geschikt voor grote vervormingen en gecompliceerde belastingspaden en houden geen rekening met veranderingen in de microstructuur tijdens de deformatie. Om deze beperkingen op te heffen is een numerieke homogenisatiemethode ontwikkeld, die in feite neerkomt op het oplossen van twee gekoppelde randwaardeproblemen: één op de macroscopische en één op de microscopische schaal. Dit soort technieken (i) vereist geen veronderstellingen ten aanzien van het globale gedrag; (ii) staat grote vervormingen en rotaties toe op zowel micro- als macroniveau; (iii) is geschikt voor willekeurig welk materiaalgedrag, met name ook fysisch niet-lineair en tijdsafhankelijk gedrag; (iv) maakt het mogelijk gedetailleerde informatie over de microstructuur en de ontwikkeling daarvan in rekening te brengen in de macroscopische analyse en (v) kan gebruik maken van elk soort model op het microniveau.

Bestaande (eerste-orde) numerieke homogenisatiemethoden passen geheel in het standaard, lokale continuümsmechanica-raamwerk. In ieder materieel punt van de microstructuur wordt de macroscopische deformatietensor berekend, welke vervolgens gebruikt wordt om kinematische randvoorwaarden te formuleren voor een microstructureel representatief volume-element dat toegekend is aan het betreffende punt. Nadat het microstructurele randwaardeprobleem is opgelost, wordt de macroscopische spanningstensor verkregen door middeling van het microstructurele spanningsveld over het volume van de representatieve cel. Op deze manier kan voor ieder macroscopisch punt de (numerieke) spanning-rekrelatie gegenereerd worden. Eerste-orde numerieke homogenisatie heeft zich bewezen als een waardevol gereedschap om de mechanische respons van niet-lineaire, meerfasige materialen te analyseren.

Echter, de eerste-orde numerieke homogenisatiemethode kent ook enkele belangrijke beperkingen ten aanzien van haar toepasbaarheid (die ook gelden voor conventio-

nele homogenisatiemethoden). Ten eerste houdt de methode weliswaar rekening met de volumefracties, verdeling en vorm van de bestanddelen, maar zijn de resultaten ongevoelig voor de absolute afmetingen van de microstructuur. Als gevolg hiervan kunnen effecten die gerelateerd zijn aan variaties van deze afmetingen niet worden voorspeld. Ten tweede kan de methode niet worden toegepast in gebieden met sterk gelocaliseerde vervormingen, waar de karakteristieke golflengte van het macroscopische deformatieveld van dezelfde orde van grootte is als de afmetingen van de microstructuur. Verder leidt, in de eerste-orde aanpak, verzwakking in een macroscopisch punt tot resultaten die afhangen van de ruimtelijke discretisatie als gevolg van het niet correct gesteld zijn van het randwaardeprobleem.

Om deze beperkingen weg te nemen wordt een nieuwe, tweede-orde homogenisatiemethode voorgesteld. Bij deze tweede-orde methode wordt de gradiënt van de macroscopische deformatietensor betrokken in de kinematica van het micro-macro raamwerk. De macroscopische spanningstensor en een hogere-orde spanningstensor worden vervolgens verkregen door middel van een uitbreiding op de Hill-Mandel energiebalans. Aldus wordt een volledige tweede-orde continuümtheorie geformuleerd, die het oplossen van een hogere-orde evenwichtsprobleem vereist door middel van een speciale eindige-elementenimplementatie.

De belangrijkste eigenschap van de tweede-orde numerieke homogenisatiemethode is in feite dat de relevante lengteschaal van de microstructuur op directe wijze in rekening wordt gebracht op het macroniveau door middel van de grootte van de representatieve cel. Deze grootte dient een afspiegeling te zijn van de schaal waarop de relevante microstructurele deformatiemechanismen zich voordoen. Dankzij het opnemen in de modellering van de afmetingen van de microstructuur kunnen fenomenen zoals schaal-effecten en macroscopische localisering beschreven worden, waarvoor de eerste-orde theorie faalt. Door middel van een aantal microstructurele analyses wordt aangetoond dat de tweede-orde aanpak een andere respons laat zien wanneer de absolute afmetingen van de microstructuur worden veranderd of wanneer macroscopische gradiënten van de deformatie worden aangebracht. Indien de afmetingen van de microstructuur verwaarloosbaar zijn ten opzichte van de lengteschaal van het macroscopische deformatieveld, vallen de resultaten verkregen met de tweede-orde modellering samen met die van de eerste-orde aanpak. Deze belangrijke constatering toont aan dat de tweede-orde homogenisatiemethode gezien kan worden als een natuurlijke uitbreiding op het eerste-orde raamwerk. In problemen waarin macroscopische localisering optreedt wordt de breedte van de localisatiezone bepaald door de microstructurele lengteschaal, waardoor resultaten onafhankelijk zijn van de numerieke discretisatie. Verder kunnen met de tweede-orde methode grenslaageffecten gemodelleerd worden door het aanbrengen van hogere-orde randvoorwaarden. Modelleren met behulp van hogere-orde continua wordt met de tweede-orde homogenisatie methode aanzienlijk eenvoudiger omdat de tweede-orde respons direct uit de micromechanica volgt in plaats van uit gesloten constitutieve relaties, welke moeilijk te formuleren zijn en die een groot aantal parameters bevatten.

Numerieke homogenisatie is een breed toepasbare strategie voor het bepalen van relaties tussen microstructuur en macroscopische eigenschappen van materialen met een evoluerende, meerfasige samenstelling waarvoor andere methoden falen.

Acknowledgements

I would like to express my sincere gratitude to Marc Geers and Marcel Brekelmans. Their guidance, help and support throughout the passed four years are greatly appreciated. Without the enthusiasm and inspiration, they have provided on an every day basis, this work would have been hardly possible. Additional thanks to Marcel for carefully reading and correcting the draft versions of this manuscript an almost infinite number of times. The discussions with Ron Peerlings and his support during the preparation of this dissertation were very important for me. I also would like to thank Frank Baaijens and Han Meijer for giving me the opportunity to carry out this PhD project in the Netherlands and the Netherlands Institute for Metals Research (NIMR) for providing the excellent working conditions. I certainly would like to thank Henk de Vree for his attention and support during the first most difficult months of my stay in Eindhoven. I owe many thanks to Leo Wouters and Patrick van Brakel for their help in “computer-related” issues. Furthermore, I would like to direct acknowledgements to all my colleagues of MaTe and the NIMR for a perfect working and social atmosphere, in particular to Hans van Dommelen, Roy Engelen, Rens Evers, Edwin Klompen, Jesus Mediavilla, Harold van Melick, René Ubachs and Katja Viatkina. I also want to thank Sebastiaan Boers and Peter Janssen for providing me with microstructural images for this publication.

I wish to express my gratitude to my mother for her initial influence on and current support of my personal and academic advances. Last but certainly not least, I wish to thank Maxim for his devoted participation in my research career, encouraging help, understanding and patience. I hope to be able to return to him all that he missed during the last months.

Varvara Kouznetsova,
Eindhoven, October 2002

Curriculum Vitae

- | | |
|-----------------------|--|
| 15 January, 1976 | Born in Perm, Russia. |
| 1983–1991 | Primary and secondary school in Perm, Russia. |
| 1991–1993 | Lyceum at the Perm State Technical University, Perm, Russia. |
| 1993–1998 | Bachelor and Engineer Degree in Applied Mathematics, specialization Computational Solid Mechanics; Department of Mathematical Modelling of Systems and Processes, Perm State Technical University, Perm, Russia. |
| 1994–1995 | Junior research assistant, Department of Mathematical Modelling of Systems and Processes, Perm State Technical University, Perm, Russia. Research topic “Development of an elasto-plastic model for non-proportional cyclic loading of metals”. |
| 1995–1998 | Junior research assistant, Institute of Continuous Media Mechanics, Russian Academy of Sciences, Perm, Russia. Research topic “Constitutive modelling of slightly compressible materials within a finite deformation framework”. |
| Sept. 1998–Sept. 2002 | PhD researcher in the Netherlands Institute for Metals Research (NIMR), cluster “Fundamentals of Forming”; placement at the Eindhoven University of Technology, in the Materials Technology group, under supervision of Prof.Dr.Ir. M.G.D. Geers. Research topic “Multi-scale computational homogenization”, resulting in this dissertation. |

